PROPELLER-INDUCED VIBRATION: EXPERIMENTAL TESTS IN ATMOSPHERIC TOWING TANK

by

© Kareem Al-Taiby, B.Eng.

A thesis submitted to the School of Graduate Studies

in partial fulfillment of the requirement for the degree of

Master of Engineering

(Ocean and Naval Architectural Engineering)

Faculty of Engineering and Applied Science

Memorial University of Newfoundland

May 2022

St. John's Newfoundland and Labrador Canada

Abstract

Ship's propellers are main sources of onboard vibration that can have adverse effects on humans and machinery alike. A reliable design tool that allows the prediction of propeller induced vibration, in the early design phases of new constructions would help prevent damage or discomfort and reduce costs related to later modifications of the propellers. In an effort to obtain data on vibration generated by ship's propellers, tests can be performed on a ship model in a tow tank. Self-Propulsion, Resistance and Bollard tests are established tests used to characterize the ship's hydrodynamics in a tow tank. Recently some researchers are investigating the possibilities to help understand the how the propeller design affects the vibration and vibration propagation to the ship body. One of the main problems with these tests is the separation of vibrational contribution of the propeller versus the fundamental frequencies of the ship model. In this work, experimental model tests were performed to evaluate the pressure fluctuations created by the propeller on a vessels structure. Methods used to perform these tests included Experimental Modal Analysis and Operating Deflection Shape, the latter performed during the hydrodynamic tests. The results show how pressure measurements can be influenced by structural vibration and thus the importance of identifying ranges of vibrational effects from the ship models' structure during hydrodynamic testing to understand if structural vibrations need to be removed from the pressure sensor measurements to give an accurate representation of vibration effects due to the propeller.

Acknowledgment

First and foremost, I would like to express my deep and sincere gratitude to my supervisor, Dr. Lorenzo Moro of the Ocean and Naval Department of Memorial University of Newfoundland. He has for giving me the opportunity to complete this research, providing invaluable guidance throughout. His vision, sincerity and support have deeply inspired me.

I would also like to express my appreciation for the patience, motivation and attentiveness of my co-supervisor, Dr. Mohammed (Shameem) Islam, Research Council Officer and Naval Architect of the National Research Council of Canada.

I also want to acknowledge my research funding through the “Propeller Induced Noise and Vibration (PINOV)” project, co-founded by Transport Canada (TC), the National Research Council (NRC), and the Department of Industry, Energy and Technology (IET) of the Government of Newfoundland and Labrador.

I am very grateful for my team mates who have been supportive and critical to the completion of my work; in particular, I would like to thank Jacopo Fragasso, without whom this research could not have been completed.

Last but not least, I would like to thank my family and friends for their continuous motivation and support during my degree.

Table of Contents

Table of Figures

List of Tables

Chapter 1: Introduction

Vibration is the one of the foundations of any structural analysis. Its effects can be seen on both the structure and humans inhabiting the space. Negative effects can, in turn, limit a ship's life span and therefore, it is essential to thoroughly investigate the structure and dynamic forces causing it.

Vibration and vibration control of structures are among the major research subjects in mechanical engineering, aerospace engineering, civil engineering, engineering mechanics, and related technical disciplines and are vital to many industrial and defense-related applications. Conventional structural designs are often unable to deal with modern problems of structural resonance caused by the complex nature of the dynamic environments. This can be seen in many industries; from the aviation industry to the power generation industry, as continual vibration effects are a key concern in design and maintenance to reduce effects such as rapid part wear, loosening hardware, or equipment fatigue and to ensure requirements like long life, low noise, and reliability.

In addition to equipment effects, vibrations have been shown to impact humans and animals in close proximity. For example, some aircraft can produce induced noise that can harm both humans and wildlife and effective means of their reductions are currently being studied (Pepper et al., 2003). Effects of high-frequency vibration from watercrafts have also been proven to affect the normal migratory patterns of nearby marine mammals (Erbe et al., 2019).

A major area where the vibrational effects are of vital concern is the maritime industry. The maritime industry is an age-old commercial market sector that employs millions of people around the world. This industry accounts for the majority of worldwide trade as an estimated 80% of all goods are carried by sea. In particular, global maritime container trade is estimated to account for around 60 percent of all maritime trade and this is estimated to be valued at 14 trillion US dollars.(United Nations Conference on Trade and Development (UNCTAD), 2019) The number and value of container ships are continually increasing, and as such, the need for further research is critical. Over the past decade, the number of container ships in the global fleet increased from 4,966 ships in 2011 to 5,371 ships in 2019, and between 1980 and 2019, the deadweight tonnage of container ships has grown from about 11 million metric tons to around 275 million metric tons.(United Nations Conference on Trade and Development (UNCTAD), 2019)

These maritime vessels are complex systems of conjoined structural and mechanical assemblies, excited by many dynamic forces. The dynamic forces produce several vibrational responses that can be transmitted throughout the ship's structure. Prolonged exposure to vibration can contribute to increased maintenance, onboard equipment failure and potentially ship structure failure. In addition to effects on the ship itself, vibrations have a direct impact on crew and passenger discomfort, increasing the opportunities for human error. Minimizing these risks is imperative to the maritime industry to improve reliability and dependability, as this industry is significant enough to have a direct effect on the global economy.

Working and living onboard vessels impose a vibratory strain on the human body. Albeit the vibration levels on board might seem within limits from an engineering point of view according to some standards, this might not be the case from human health. Numerous studies of the harmful effects of vibration resonance have been performed on the human body. Frequencies from 5-15 Hz may be acceptable for certain structures, while intense frequencies within this range are considered hazardous for humans (Subashi et al., 2008). Within this low-frequency range, constant whole-body vibration exposure, as well as impulse shock loads, can result in motion sickness, body instability, fatigue, and increased health risk (Jensen & Jepsen, 2014; Kingma et al., 2003).

On the other hand, high-frequency vibrations cause poor performance, wellness, and comfort levels.

When a ship is subjected to an impulsive load, such as a sudden descending anchor, it will produce elastic vibrations, in addition to rigid body motions, affecting the ship's structure. Of these vibrations, some can be observed only locally and others throughout the hull. Sources of these vibrations can be found in multiple locations in a marine vehicle, and can include:

- Diesel engines
- Propeller pressures and forces
- Maneuvering devices
- Machinery onboard
- Sea wave slamming

Vibrations are important to be considered in the structural design phase, and it has become standard practice to mitigate vibration levels for new builds. Recently, vibration analyses are being performed during the preliminary or structural design stage for many ship types, due to the increased efficiency-seeking industry. Some areas of optimization that designers take into account are:

- Lightweight construction (with low stiffness and mass)
- Arrangement of living and working places near the propeller area to optimize cargo space
- High propulsion power
- Tip clearance of the propeller (to increase propeller efficiency)
- Fuel-efficient, slow-running main engines.

According to ISO guidelines for mechanical vibrations, vibrations levels of interest cover the frequency range of 1 to 80 Hz (International Organization for Standardization (ISO), 2000). Figure 1 shows common natural frequencies of ship structures (Lloyd's Register, 2006; Smolko, 2009). Ship vibrations can become problematic if the exciting frequency is close to a natural frequency of the structure; this is defined as resonance.

	Min	Max
Global hull structures	0.5 Hz	10 Hz
Local structures	10.0 Hz	50 Hz
Deckhouse and aftbody structures	4.0 Hz	15 Hz
Structures above propeller	18.0 Hz	> 100 Hz
Large deck-panel structures	6.0 Hz	20 Hz
Engine foundations	20.0 Hz	> 100 Hz
Mast structures	7.0 Hz	21 Hz
Slow-running engines	4.5 Hz	12 Hz
Medium-speed engines, realistically supported	20.0 Hz	60 Hz
Medium-speed engines, mounted resiliently	1.5 Hz	7 Hz
Propeller shaft lines	4.0 Hz	19 Hz

Figure 1 – Natural Frequency Ranges in Ship-building Applications (Lloyd's Register, 2006)

There are several sources of ship vibration; one such example is vibration from rotating or reciprocating machinery, as previously mentioned. This has led to studies where engines installed on resilient mounts have been analyzed to better understand their contribution to ship vibration (American Bureau of Shipping (ABS), 2006a; Asmussen et al., 2001; Biot & Moro, 2012; Norwood & Dow, 2013; Pais et al., 2017). Another common cause is the propeller, which is frequently a source of trouble and can cause excessive ship stern vibration as pressure pulses are generated by the propellers' blades while spinning. There are typically three main methods used for predicting and measuring the effects of pressure pulses; these include experimental methods, empirical, and computational methods. The consequences of excessive vibration, particularly in the stern area, can be severe as deterioration of the structural members can be accelerated due to long-term cyclic vibration fatigue. Excessive vibration from the propeller can also damage or adversely impact the in-service performance of the ship's equipment and can impact crew safety and comfort. Therefore, it is critical to understand the vibration effects of the propellers on the hull of ships that are being used every day.

Experimental tests are performed on full-scale ships (Zambon et al., 2021) or on ship models during hydrodynamic tests in the towing tanks (Wijngaarden, 2011). The latter has been used to assess propeller-induced hull pressure fluctuations on the ship model hull in early design phases.

The objective of this study is to capture the dynamics of the ship model, analyze the ship characteristics, and effectively capture vibrational data using a scaled model of the container ship. This will allow for the study of the vibrations induced in the hull through both the ship's body movement in the water and the vibration caused by the rotation of the propeller. This will aid in developing a procedure to measure the propeller-induced hull vibration in tow tanks. It will also help understand the effect of dynamics of the ship body with respect to the induced hull vibrations and allow for the extraction of validated experimental data for an FEA model to be developed at a later stage. To perform the vibration analysis of the scaled container ship model studied, the experimental testing was divided into two parts. First, modal testing was conducted to determine the vibrational characteristics, such as the natural frequencies and mode shapes, of the mechanical structure (Steen, 2015). A hammer test was performed, both in water and in air, to perform the modal testing with nine accelerometers installed on the deck of the ship model to capture the vibration changes. Secondly, ship model runs were performed in water to capture ship dynamics. Three types of tests were completed: a resistance test, a bollard test and a self-propulsion test following the International Towing Tank Conference guidelines for each (The International Towing Tank Conference (ITTC), 2011a, 2014, 2017). Alongside the accelerometer data for the second part of the testing, twelve highly sensitive pressure sensors, installed in the ship hull directly above the propeller, recorded pressure fluctuations following the peer-reviewed literature (The International Towing Tank Conference (ITTC), 2011; Wijngaarden, 2011). The recorded measurements of pressure fluctuation are translated into vibration on the hull of the vessel.

This thesis is a part of a large research project, ‘Propeller Induced near- and far-field Noise and ship hull Vibration (PINOV)” funded by Transport Canada (TC), National Research Council (NRC) and Department of Industry, Energy and Technology of the government of Newfoundland and Labrador. The primary objectives of this project are the development of design tools to predict underwater radiated noise and propeller-induced hull vibration from non-cavitating propellers. The work presented in this thesis is fundamental to provide guidelines for experimental tests of hull-induced propeller measurements in a towing tank. One of the problems with propeller-induced hull vibrations is that there can be a matching of the dyamincs of the propeller and the body , this can produce unwanted noise. Using this sequence that was done (Modal analysis, Self-Propulsion and Resistance tests, and Operating Deflection Shape), it was possible able to identify the dynamics of the model, hence identify any critical resonance. If the resonance matched the fundamental frequency of the excitation frequency of the propeller, then there are unwanted pressure measurements/distoration. So using the Operating Deflection Shape, these unwanted pressure measurements can be removed following the procedure presnted by Wijngaarden. (Wijngaarden, 2011)

The outcomes of these experimental tests are used to validate numerical models and help the development of the design tool for pressure fluctations by the propeller in the hull area. Further research will be done to create a design tool for theses pressure flucations, which inlcudes the creation of a numerical model to simulate the dynamics of the ship model.

Chapter 2: Literature Review

Though ships and various types of watercraft have been around for centuries, it was not until the late eighteen hundreds that studies on ship vibration and its effects began. With the invention and widespread use of the steamship, scientific studies were undertaken to better understand the effects and prevention methods of ship vibration and noise. The steamship's large and reciprocating engines caused excessive vibration, along with engine balance issues. In 1893, Otto Schlick presented the Pallograph, the first device designed to measure the vibrations of a steamship. Soon after, methods of dealing with vibrations due to engine balancing were created, such as the Yarrow-Schlick-Tweedy system of engine balancing, introduced in 1894.

Steamship use has almost died out over the past century; however, the newer diesel-powered ships face similar issues of vibrations. Marine vessels are complex systems and are excited by many dynamic forces, including the diesel engine itself, the propeller, maneuvering equipment, and are further affected by sea conditions. Vibrations caused by these forces can cause damage to ships through excessive wear, loosening of the propulsion system, and overall fatigue of the ship structure, which in turn affect sensitive equipment and potentially compromises the safety of the vessel (Asmussen et al., 2001). Since World War II, scientists have acknowledged the importance of studying and predicting the response of vibrations onboard vessels; however, they were focused on solutions for singular vibration problems rather than on the ship as a whole (Ship Structure Committee, 1990).

Vibration in ships is a source of discomfort to people on board, leading to degraded performance and health, and affects the overall duties of crew members (American Bureau of Shipping (ABS), 2014b; American Bureau of Shipping, 2016; Constantinescu et al., 2009). All these factors impede overall operations and safety on the ship. Many studies have been performed to minimize vibration levels aboard vessels in terms of structural safety and ergonomic-personal wellbeing, particularly in the context of luxury transportation (American Bureau of Shipping (ABS), 2006b; Asmussen et al., 2001; Norwood & Dow, 2013; Ojak, 1988; Pais et al., 2017). Some of these studies have led to the development of floating floors (Moro et al., 2016), and resilient mounts (Biot & Moro, 2012; Moro, 2015; Moro et al., 2015; Fragasso et al., 2017) to decouple ship structures from the onboard sources. The use of viscoelastic materials has also been proven to provide a viable means to dampen the effects of noise and vibration on board (Fragasso et al., 2017; Vergassola et al., 2018). However, from a control hierarchy perspective, a more dependable process would be the elimination of vibration during the design vessels, rather than the use of corrective methods post-manufacturing. As shown in (America Bureau of Shipping (ABS), 2014), the cavitating propeller is usually the main vibration source. It contributes to vibrations directly by exciting the ship through the drive train and indirectly by creating pressure fluctuations in the water that transmit hydro-acoustic waves to the hull above the propeller.

The International Towing Tank Conference (ITTC) was first formed in 1933 and started with 23 representatives seeking to promote improvements of ship model work and approve guidelines for publication. It has grown in the last 80 years into a voluntary association of worldwide organizations responsible for predicting the hydrodynamic performance of ships and marine installations based on the results of physical and numerical experiments. They aim to stimulate research into specific topics, organize meetings to review progress and establish procedures to ensure member organizations retain institutional credibility (The International Towing Tank Conference (ITTC), 1966).

Propeller research and the effect of cavitation have been a key topic promoted by the ITTC. By the third ITTC, the cavitation effect on propellers was known, but the full influence of vibration was not yet discovered. It was not until the 11th ITTC where the ITTC proceedings gave an account of propeller-induced vibratory surface forces. In these proceedings, Schwanecke wrote: ‘The exciting pressure fluctuations at the hull plating close to the propeller, the bossings, rudders, etc. will be found out either by model tests and full-scale experiments respectively by means of inductive or strain gauge mounted pressure pickups, or they will be found out by calculating the propeller pressure near field by means of the potential theory.’ It was also found that measurements performed with highly loaded propellers have minimal effect on the exciting amplitudes at the hull plating for propellers, differing only according to the number of blades (The International Towing Tank Conference (ITTC), 1966). ITTC, until recent years provided a comprehensive guide to measurement, analysis, and prediction of undesirable vibrations onboard both full scale and scaled models.

Following the aforementioned ITTC measurement guidelines, several studies have been dedicated to the measurement of scaled ship propeller vibrations. Most notably, Eric Van Wijngaarden, performed an extensive study to measure the scaled model cavitating propeller pressures and validated using predictive algorithms within a 15% margin. He also developed techniques to extrapolate local and global vibratory data from scaled experimental hull pressure measurements (Wijngaarden, 2005, 2011; Wijngaarden et al., 2006).

At the same time, (Dessi et al., 2021), estimated the modal damping concerning the ship bending modes experimentally via physical model tests of a cruise ship, carried out both in the towing-tank and in a vibration lab. Such a study is a crucial step in analyzing the damping of the ship body to have a better understanding of the model dynamics and to get response limits for resonance conditions.

Their analysis was also carried out in both “wet” and “dry” conditions. This allows for both (i) the segregation of hydrodynamic damping effects for the ship model and (ii) the comparison of the damping effects with the input-output techniques based on the calculation of the frequency response functions (FRFs). (Dessi et al., 2021; Mariani & Dessi, 2012)

In comparison, a modal analysis was the first step conducted in this research in both “wet” and “dry” conditions to better understand the modal ship’s dynamic properties. This is done in an effort to try to extend the work done by Wijngaarden by using a non-cavitating propeller in air-open tanks. With further tests and analysis, the research will help develop a starting point for numerical models, simulate the model’s interactions with the propeller and validate it using the experimental methods. Consequently, the digital model can be used to change the criteria and parameters of the ship model and see the variations in the induced pressure on the hull.

Chapter 3: Methodology

When performing experiments on a scale ship model in a towing tank, to predict hull-pressure fluctuations and the resulting vibratory hull-excitation forces, one must ensure the same geometric, kinematic and dynamic conditions are met in both the in model and prototype (Steen, 2015). This means similarity in the relevant aspects such as lengths, displacements, velocities, accelerations and forces. Thus, ship scale quantities may be predicted from their model scale counterparts by a proportionality factor. Consequently, a 1/60 scaled container ship model shown in Figure 2 has been developed at the National Research Council Canada (NRC-OCRE) facility to study propeller-induced non-cavitating hull vibrations.

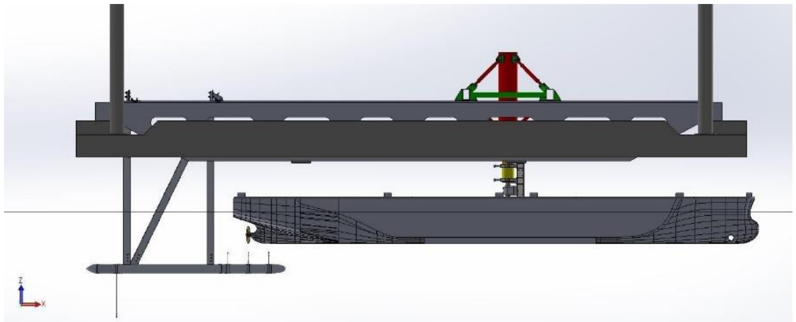

Figure 2 – Scale Container Ship Attached to the Carriage for Testing

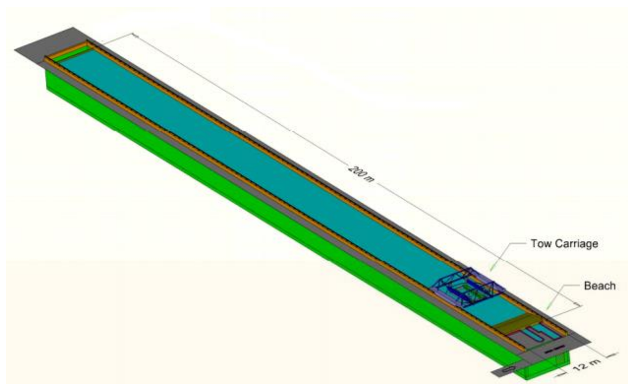

Figure 3 – Tow Tank at the National Research Council Canada Facility

This study was achieved with three main tests:

- Modal Testing: completed using a load cell rugged impact hammer test on the ship body
- Hydrodynamic tests, which include:
    - Operation Deflection Shape (ODS) Tests: consisting of nine accelerometers installed on the ship deck to measure the acceleration changes as the ship model is towed through the tank.

- Pressure Tests: twelve pressure sensors were installed in the stern of the ship, within the hull and above the propeller to measure the direct effect of the pressure fluctuations of the ship's propeller.

The hydrodynamics measurements were performed in three testing conditions: bollard tests, resistance tests and self-propulsion tests.

A ship model was used to perform the detailed layout of this facility. The ship structure is made of 440 Renshape, brass, hi-60 foam, plywood, pine & fiberglass. The tank is 200 m long, 12 m wide, and 7 m in depth, a model of this is shown in Figure 3. The sidewalls of the tank are made of concrete and painted with a thickness of 6 mm, these sidewalls, along with the bottom of the tank are flat and the water surface is open to the atmosphere. A carriage powered by an eight-wheel 746 kW synchronized motor drive supports the model, and the measurement system can slide over the railways. The weight of the carriage is 85,000 kg and can achieve a speed range between 0.001 m/s to 10 m/s. The facility can accommodate a maximum model size of 12 m in length, and the test frame could be adjusted for model size. Normal tap water was used in the tank, and the temperature of the water was maintained between 16-18 ^{0}C for the duration of the experiment. The above mentioned tow-tank experiements were carried out in the towing tank at NRC-OCRE.

3.1 Ship Model Case Study

Below is a brief description of the ship model constructed for the testing, and a picture of the model can be seen in Figure 4 and Figure 5:

Figure 4 – Ship Model Used in Testing

Figure 5 – Close Up of Ship Model's Propeller

- Geometry: the dimensions of the overall model are shown in Table 1**Error! Reference source not found.** below. The geometry was generated in SOLIDWORKS and can be seen in Figure 6 – Global Geometry of the Model and the material used for the fabrication includes:
  - Fibre-Reinforced Plastic (3 Layers, 6 Oz)
  - SPF Plywood (Spruce, Pine, Fir)
  - Brass
  - RenShape 440
  - Hi-60 Foam

Table 1 – Ship Model Dimensions

Model Dimensions	
Length Overall (mm)	7142
Depth (mm)	623
Breadth (mm)	1024

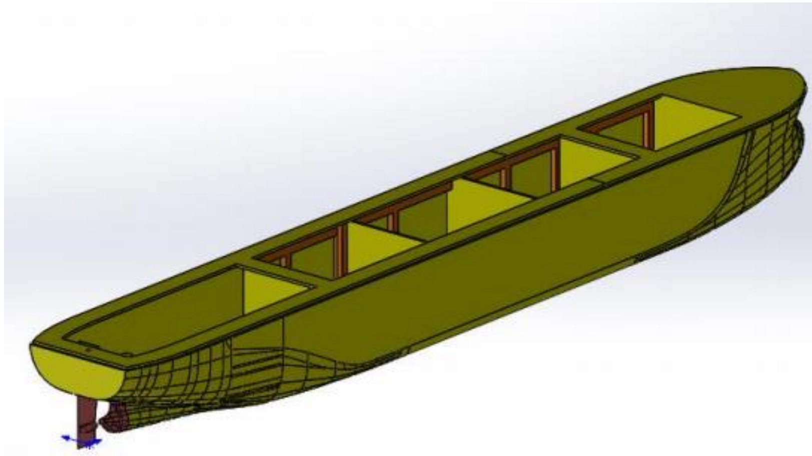

Figure 6 – Global Geometry of the Model

- Weight: to have sufficient hydrostatic equilibrium in the model attached to the carriage, weights have been used to compensate for the light weight of the low-density materials in the model structure. The final model displacement, lightweight, and total ballast weights are shown in Table 2 below.

Table 2 – Ship Model Weight

Weights of Model	
Total ballast (kg)	2260
Model weight (kg)	425
Total displacement (kg)	2685

For comparison, the actual dimensions of the full-scale ship are shown in Table 3.

Table 3 – Full-Scale Ship Dimensions

Full-Scale Dimensions (OCRE916 CLS TANKER)	
Length Overall (m)	226.198
LWL (m)	226.198
Beam (m)	32.261
BWL (m)	32.238
Volume (m^3)	83547.92
Displacement (MT)	85637.09

Nine accelerometers were installed on the top surface of the ship body, as shown in Figure 7 below. All the accelerometers were connected to a National Instruments Data Acquisition System (NI 9234) and processed on a laptop with National Instruments LabVIEW® script that records all measured data as raw data for later analysis. In parallel, twelve highly sensitive PCB PIEZOELECTRONICS acoustic pressure sensors (106B50) were installed in the hull of the ship during the ship construction, as shown in Figure 13.

Throughout the first part of the test, the Hammer test was conducted on the ship body for Modal testing. An integrated force sensor rugged impact hammer was used to simulate an impulse excitation on the body of the ship. A moving bridge above the tow tank was used to have all the storage data and connections of the measuring sensors, while the ship model was connected to the bottom of the bridge to help perform the resistance test, bollard test and self-propulsion tests. The moving bridge can also control the speed of the connected model and take a live video of the entire testing area.

3.2 Modal Testing

Modal testing is a method of testing that allows the calculation of the natural frequencies (modes), modal masses, modal damping ratios and mode shapes of a test structure. Typical methods of modal testing are either impact hammer testing or shaker testing (Rao, 2007). Since I am concerned with general vessel dynamics characteristics in the low-medium frequency range, and attaching the modal shaker is impractical, impact hammer testing will suffice. In theory, an impact would be created on the structure with a perfect impulse. This would be of infinitely short duration and would result in a constant amplitude in the frequency domain. This type of impulse is only possible theoretically. But, there is a known contact time and this duration is directly linked to the frequency of the force applied.

In hammer impact testing (modal testing), the ship structure is tested using the load-cell equipped hammer to generate the impulse and then measure the response using accelerometers. This should be done at several points on the ship structure to capture the profile of the entire hull. The red arrows shown in Figure 7, Figure 8 and Figure 9, show the pre-determined locations where the impacts are delivered on the ship body.

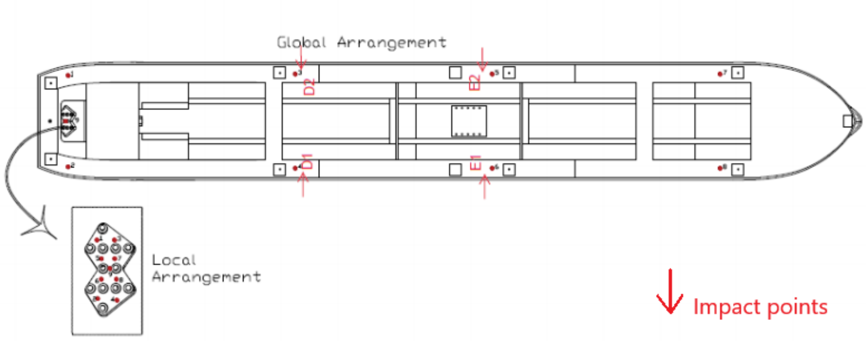

Figure 7 – Ship Model with Impact Points' Locations

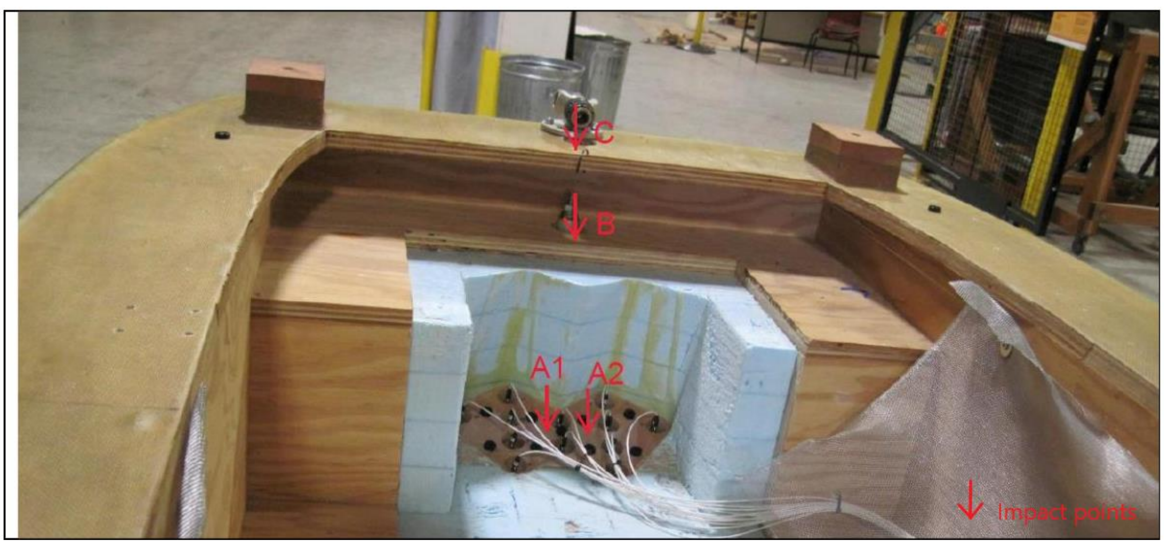

Figure 8 – Impacts Points on the Aft of the Ship Model

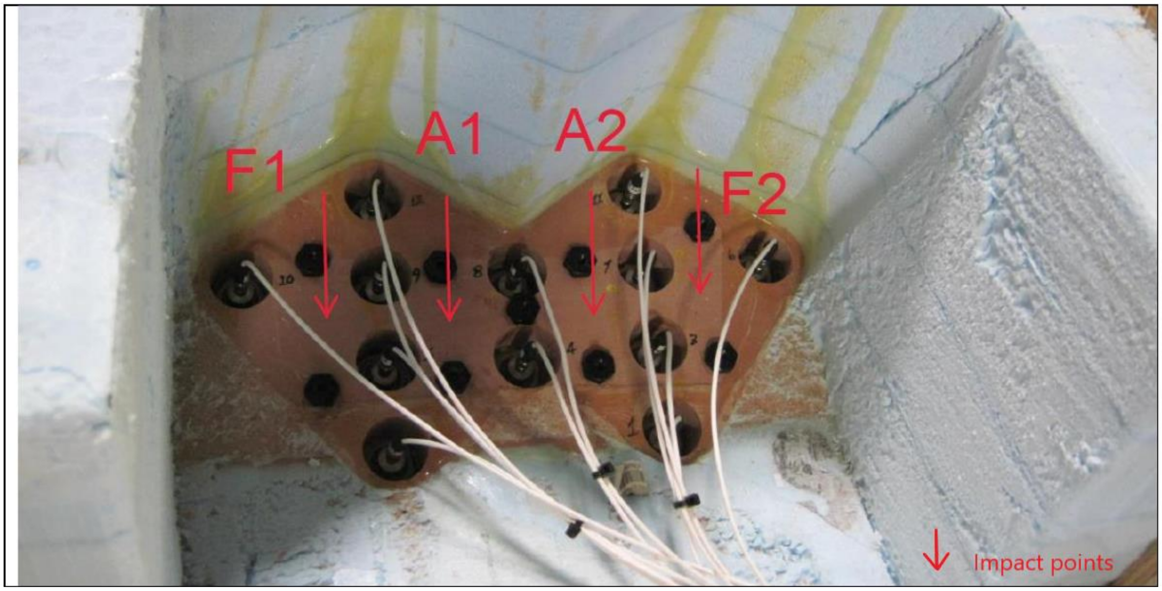

Figure 9 – Impact Points near Pressure Sensor Arrangements

The hammer test for this experiment was performed under two conditions: in water and in air. The accelerometers were placed in two arrangements, global and local. The global arrangement is along the ship deck, while the local arrangement is on the aft part of the ship, as shown in Figure 10 below. The positions of the impacts were pre-determined as per the above pictures. Each measurement was taken approximately thirty-five seconds after the hammer impact, and to ensure a reliable averaged measurement, each impact at the pre-determined locations was repeated three times with sixty seconds between each impact. The sampling frequency used during these tests for the accelerometers measurement was 2048 Hz.

The frequency range of the hammer test can be varied by changing the type of tip used. To elicit a higher frequency response, a stiffer tip without the extender mass should be used. For a lower frequency response, a softer tip, with the extender mass is preferred for an ideal response. Given the dynamic properties and size of the model, and to ensure a high-quality impact, a medium-soft tip was used for the hammer with the extender mass.

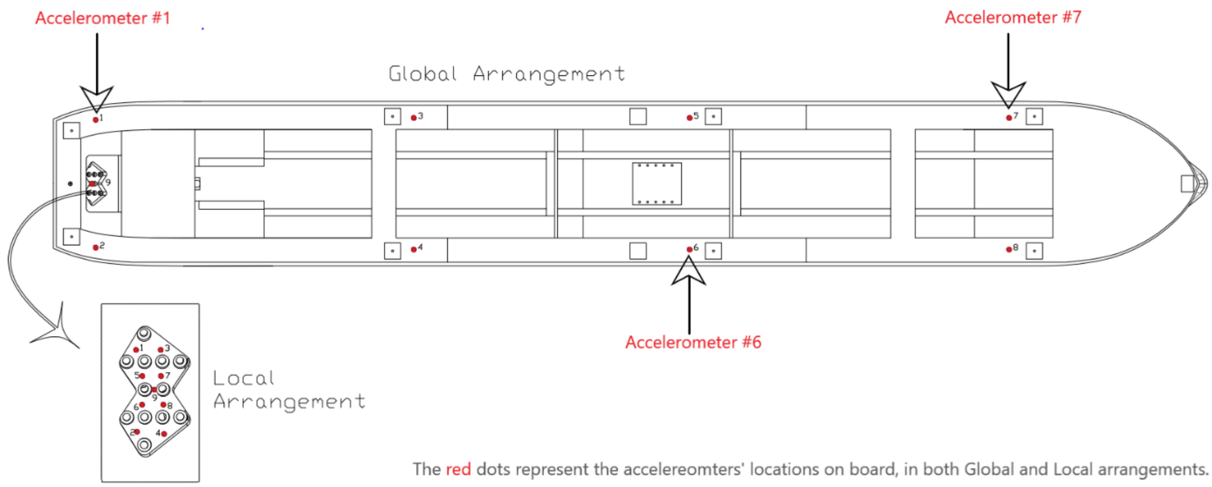

Figure 10 – Global and Local Arrangements of Accelerometers

After an impact was applied, the response was recorded and processed using MATLAB® and the ABRAVIBE toolbox to generate the Frequency Response Function (FRF) plots, the Fast Fourier Transform (FFT) plots and the and coherence plots. FRF and FFT plots were calculated and then averaged to produce more reliable data. Finally, the output was analyzed after validating data integrity against the coherence plots. The MATLAB® script flow chart for generating these plots can be seen below in Figure 11.

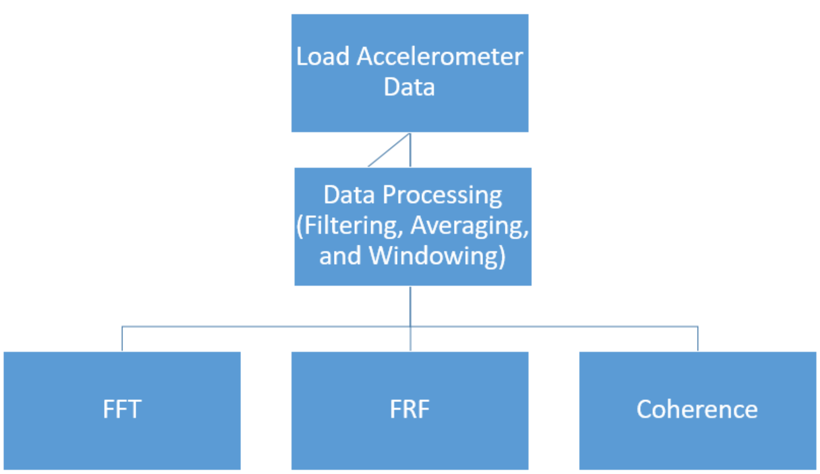

Figure 11 – MATLAB® Script Flow Chart

The Load Accelerometer Data block in Figure 11 is where the three accelerometer measurement files are loaded (ex: Air_Global_A2_001, Air_Global_A2_002 and Air_Global_A2_003). Each file contains the nine accelerometer readings as well as the impact force from the hammer. The Data Processing Block in Figure 11 is where all accelerometer signals are then filtered and averaged to produce a reliable, consistent output. Finally, the averaged signals along with the impact force signal are used to produce FRF Plot, FFT Plots, Averaged FFT Plots, and Coherence Plots.

3.2.1 Modal Analysis

To better visualize the movement of the accelerometers after the hammer impact and simulate the system's modes, the ABRAVIBE toolbox was used. ABRAVIBE is a free, open-source MATLAB® /Octave toolbox to learn, teach, and practice vibration analysis. The ABRAVIBE code was adjusted to adapt to the research at hand. The developed code was able to simulate the ship's body response to the hammer impact. MATLAB® was used to load three accelerometers' measurements, measurements were then averaged, filtered and coherence plots were generated. FRF and FFT plots were calculated and averaged to produce more reliable data. The output was analyzed after validating data integrity against the coherence plots. Finally, an animation of the perspective, X, Y and Z views of the ship deck structure were plotted based on the chosen frequencies.

3.2.2 Instrumentation

To summarize the instrumentation and equipment used during the above modal testing procedure, below is a list of those items:

- Hardware:

  - National Instruments Data Acquisition System (model number: NI9234) – Quantity: 4
  - National Instruments Compact DAQ Chasis (model number: cDAQ-9174) – Quantity: 1
  - PCB Piezoelectric ICP Impact Hammer (model number: 086C03) – Quantity: 1
  - PCB Piezoelectric ICP Accelerometers (model number: 352C33) – Quantity: 9
  - Laptop with the required software
- Software:
  - National Instruments LabVIEW®
  - MATLAB® by MathWorks® software.

3.3 Hydrodynamic Tests

The hydrodynamics tests took place in three testing forms. Those forms are listed below:

- Resistance Test: this is performed without a propeller, and the model is pulled across the tank using the carriage. Resistance tests are conducted to provide data from which the resistance of the model hull at any desired speed may be determined. For this purpose, the model resistance and its speed through the water are simultaneously measured. ITTC 7.5-02-02-01 Rev03 Resistance Test's guidelines were followed. (The International Towing Tank Conference (ITTC), 2011a)
- Bollard Test: the bollard test is performed while the propellers are rotating, but the bridge is not moving, keeping the ship stationary in the water. Bollard pull is the static force exerted by a ship on a fixed tow line at zero speed. Typically, the bollard pull test is conducted as part of the self-propulsion test. This implies that the same measuring

equipment and instrumentation are used for both tests. ITTC 7.5-02-03-01.1 Rev05 Propulsion/Bollard Pull test guidelines were followed to perform all of the bollard tests. (The International Towing Tank Conference (ITTC), 2017)

- Self-propulsion Test: in this test, the model is allowed to move across the tank with the propeller rotating at a fixed rotation per minute (RPM). ITTC 7.5-02-03-01.01 Rev02 Performance Propulsion Test' guidelines were followed during the self-propulsion tests. (The International Towing Tank Conference (ITTC), 2017)

During the hydrodynamic tests, two kinds of measurements were taken: ODS (Operating Deflecting Shape) and Hull pressure sensors measurements. ODS was used to verify the dynamics characteristics of the ship model while the ship was moving, and hull pressure sensors were installed to monitor the pressure fluctuations on the hull.

3.3.1 ODS Measurements and Analysis

As mentioned earlier, nine accelerometers were placed on the deck as a global arrangement setup and a local arrangement at the stern of the ship. Three types of tests were performed for the ship model in the water:

- Bollard test
- Resistance test
- Self-Propulsion test

When performing the above tests, they were first conducted with the global arrangement, then performed again with the local arrangement. Different pre-selected RPMs and bridge velocities were used in each test. The data captured throughout the accelerometers were saved, and the Fast Fourier Transform (FFT), averaging and windowing were applied to the signals. Each signal was split into 5 second windows, the Hanning window was applied, and then an average of those windows was taken. In addition, the Blade Pass Frequencies (BPF) were plotted using a different modified version of the ABRAVIBE tool used previously in the hammer test.

The table below shows the summarized test log that was pre-determined and followed during the test durations. Some tests were repeated several times for consistency but are not shown below. These tests were conducted over a period of several days, and several rough-up runs were completed that are not mentioned in Table 4 below.

Table 4 – Test Log

DATE	FILENAME (.DAQ)	CARRIAGE SPEED (m/s)	RUN DESCRIPTION	COMMENTS
20-Feb-20	Roughup_004	1.238	OCRE-916 Resistance	
20-Feb-20	Roughup_005	1.422	OCRE-916 Resistance	
20-Feb-20	Res_001	0.734	OCRE-916 Resistance	
20-Feb-20	Res_002	0.826	OCRE-916 Resistance	
21-Feb-20	Roughup_007	0.871	OCRE-916 Resistance	
21-Feb-20	Res_009	1.192	OCRE-916 Resistance	
21-Feb-20	Res_015	1.376	OCRE-916 Resistance	
21-Feb-20	Res_019	1.559	OCRE-916 Resistance	
21-Feb-20	Res_020	0.917	OCRE-916 Resistance	
21-Feb-20	Res_022	1.101	OCRE-916 Resistance	
21-Feb-20	Res_023	1.284	OCRE-916 Resistance	
21-Feb-20	Res_024	1.468	OCRE-916 Resistance	
24-Feb-20	Bollard_001	0.000		Bollard, steps of 2rps up to 15rps.
24-Feb-20	Bollard_002	0.000		Bollard, steps of 2rps up to 11rps.
25-Feb-20	SP_001	0.917	X	Self propulsion, 10.5rps, Hydrophone array in place
25-Feb-20	SP_003	0.917	X	Self propulsion, 12rps, Hydrophone array in place
25-Feb-20	SP_004	0.917	X	Self propulsion, 6rps, Hydrophone array in place
25-Feb-20	SP_006	0.917	X	Self propulsion, 5rps, Hydrophone array in place
25-Feb-20	SP_011	1.101	X	Self propulsion, 5rps, Hydrophone array in place
25-Feb-20	SP_012	1.101	X	Self propulsion, 5.5rps, Hydrophone array in place
25-Feb-20	SP_013	1.101	X	Self propulsion, 6rps, Hydrophone array in place
25-Feb-20	SP_014	1.101	X	Self propulsion, 6.5rps, Hydrophone array in place
25-Feb-20	SP_015	1.101	X	Self propulsion, 7rps, Hydrophone array in place
25-Feb-20	SP_016	1.101	X	Self propulsion, 6rps, Hydrophone array in place

25-Feb-20	SP_018	1.101	X	Self propulsion, 4.5rps, Hydrophone array in place
26-Feb-20	Bollard_005	0.000		Bollard, steps of 2rps up to 11rps.
9-Mar-20	Frictions_002	0.000		Frictions, steps of 2rps up to 15rps.
9-Mar-20	Frictions_003	0.000		Frictions, steps of 2rps up to 15rps.
9-Mar-20	Bollard_006	0.000		Bollard, steps of 2rps up to 11rps.
9-Mar-20	SP_019	0.917	X	Self propulsion, 3.0rps, Hydrophone array in place
9-Mar-20	SP_020	0.917	X	Self propulsion, 3.5rps, Hydrophone array in place
9-Mar-20	SP_022	0.917	X	Self propulsion, 5.0rps, Hydrophone array in place
10-Mar-20	SP_023	0.917	X	Self propulsion, 4.05rps, Hydrophone array in place
10-Mar-20	SP_025	0.917	X	Self propulsion, 4.5rps, Hydrophone array in place
10-Mar-20	SP_026	0.917	X	Self propulsion, 4.45rps, Hydrophone array in place
10-Mar-20	SP_031	1.101	X	Self propulsion, 5.2rps, Hydrophone array in place
10-Mar-20	SP_032	1.101	X	Self propulsion, 5.1rps, Hydrophone array in place
10-Mar-20	SP_033	1.101	X	Self propulsion, 5.35rps, Hydrophone array in place
10-Mar-20	SP_034	1.101	X	Self propulsion, 5.41rps, Hydrophone array in place
10-Mar-20	SP_039	1.284	X	Self propulsion, 6.5rps, Hydrophone array in place
11-Mar-20	Bollard_007	0.000		Bollard, steps of 2rps up to 11rps.
11-Mar-20	Bollard_008	0.000		Bollard, steps of 2rps up to 11rps.
11-Mar-20	SP_045	1.284	X	Self propulsion, 6.26rps, Hydrophone array in place
11-Mar-20	SP_046	1.376	X	Self propulsion, 6.7rps, Hydrophone array in place
11-Mar-20	SP_047	1.376	X	Self propulsion, 7.0rps, Hydrophone array in place
11-Mar-20	SP_049	1.376	X	Self propulsion, 6.79rps, Hydrophone array in place
11-Mar-20	SP_050	1.376	X	Self propulsion, 6.8rps, Hydrophone array in place
11-Mar-20	SP_054	0.917	X	Self propulsion, 4.45rps, Hydrophone array in place, alternate accel. location.
11-Mar-20	SP_057	1.101	X	Self propulsion, 5.41rps, Hydrophone array in place, alternate accel. location.
11-Mar-20	SP_058	1.101	X	Self propulsion, 5.41rps, Hydrophone array in place, alternate accel. location.
11-Mar-20	SP_059	1.101	X	Self propulsion, 5.41rps, Hydrophone array in place, alternate accel. location.
12-Mar-20	Bollard_009	0.000		Bollard, steps of 2rps up to 11rps.
12-Mar-20	roughup_013	0.917		Self propulsion, 8rps, Hydrophone array in place

12-Mar-20	SP_060	1.284	X	Self propulsion, 6.26rps,Hydrophone array in place, alternate accel. location.
12-Mar-20	SP_063	1.376	X	Self propulsion, 6.8rps,Hydrophone array in place, alternate accel. location.
12-Mar-20	Bollard_010	0.000		Bollard, 4.45rps.
12-Mar-20	Bollard_011	0.000		Bollard, 5.41rps.
12-Mar-20	Bollard_012	0.000		Bollard, 6.26rps.
12-Mar-20	Bollard_013	0.000		Bollard, 6.80rps.

3.3.2 Hull Pressure Sensors Analysis

While performing the tests noted previously, twelve highly sensitive pressure sensors, as shown in Figure 12, Figure 13, and Figure 14, were used to capture the pressure fluctuations caused by the propeller at the hull area to see the hull excitation from the propeller.

Figure 12 – PCB Piezoelectric Acoustic Pressure sensors (model number: 106B50)

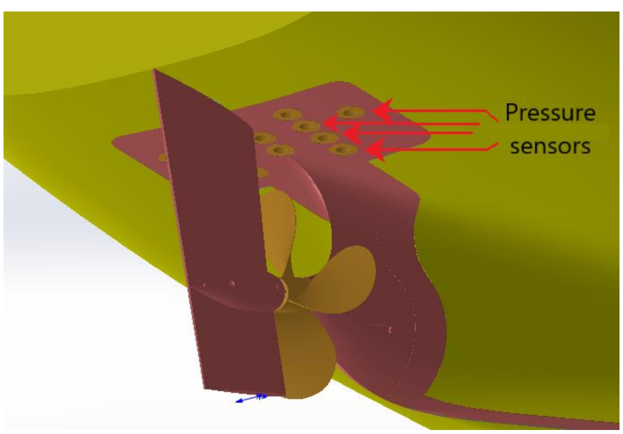

Figure 13 – Pressure Sensors Installation Locations in 3D Model

Figure 14 - Pressure Sensors Installation Locations on Ship Model

Data from those pressure sensors were acquired at a 25 kHz sampling frequency. The time-domain signal captured was then cropped to eliminate any transient components in correspondence of the signals' tails. Accordingly, the signals were then windowed with a Hanning window using a MATLAB® code. This code was also developed to perform an FFT analysis on those measurements (ex: SP_003_0.917_12rps), including averaging the signals. This MATLAB® code (example of the code file name: pressure_1_windows) executes in the below manner:

- The test results are uploaded to the code
- The signals measured from the pressure sensors are cropped
- Windowing is applied to the signals
- An FFT is obtained for each window; then an average FFT is generated

3.3.3 Instrumentation

To summarize the instrumentation and equipment used during the above Hydrodynamic testing procedure, see the below list:

- Hardware:
    - Laptop with the required software
    - PCB Piezoelectric Acoustic Pressure sensors (model number: 106B50) – Quantity: 12.
    - PCB Piezoelectric ICP Accelerometers (model number: 352C33) – Quantity: 9
    - National Instruments Data Acquisition System (model number: NI9234) – Quantity: 4
    - National Instruments Compact DAQ Chasis (model number: cDAQ-9174) – Quantity: 1
- Software:
    - MATLAB® by MathWorks® software.

- ABRAVIBE by MATLAB® toolbox. (with some customizations in the toolbox code)

Chapter 4: Results

This section presents the results acquired from the modal testing and the ODS and pressure sensors measurements. First, the hammer test is completed on the model in both air and water. This is performed according to a preset procedure and at specified locations. Once complete, the data acquired was recorded and analyzed to obtain the dynamic characteristics of the model and the shape modes. For a more descriptive visualization of the shape modes for the model, ABRAVIBE MATLAB® code was used to do the plotting.

Secondly, the accelerometer data and pressure sensor data were recorded during the three types of tests: Resistance, Bollard and Self-Propulsion. The measured signals were then uploaded to a different modified version of the ABRAVIBE code. The measured signals of the twelve pressure sensors are cropped, and windowing is applied to the signals. Then FFT plots were obtained for each window, then an average FFT of all the windowed FFTs was generated. Also, the first 6 peaks of the FFT were also noted down.

4.1.1 Ship Modal Testing Results

Figure 15 and Figure 16 present the FFT acquired by the accelerometers during the modal test in the air with the global accelerometer arrangement. Table 5 presents the main peaks from the FFT and the related mode number.

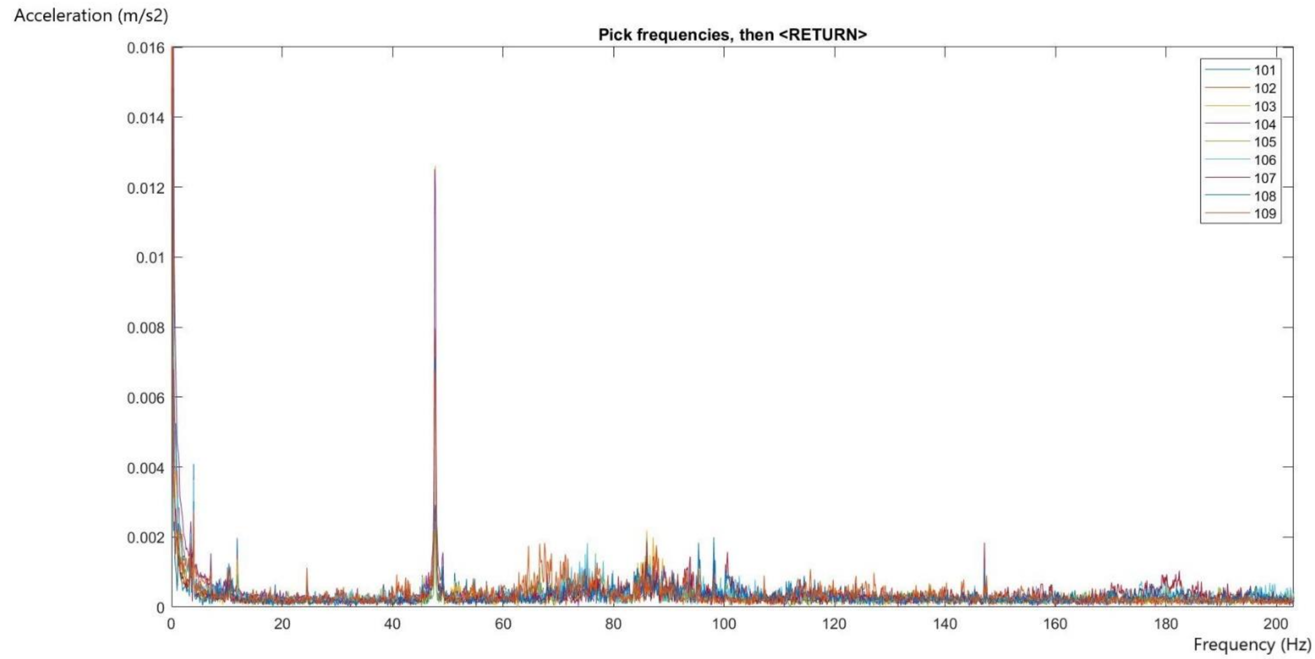

Figure 15 – Linear Frequency Plot for Global Arrangement in Air at Impact Point A2

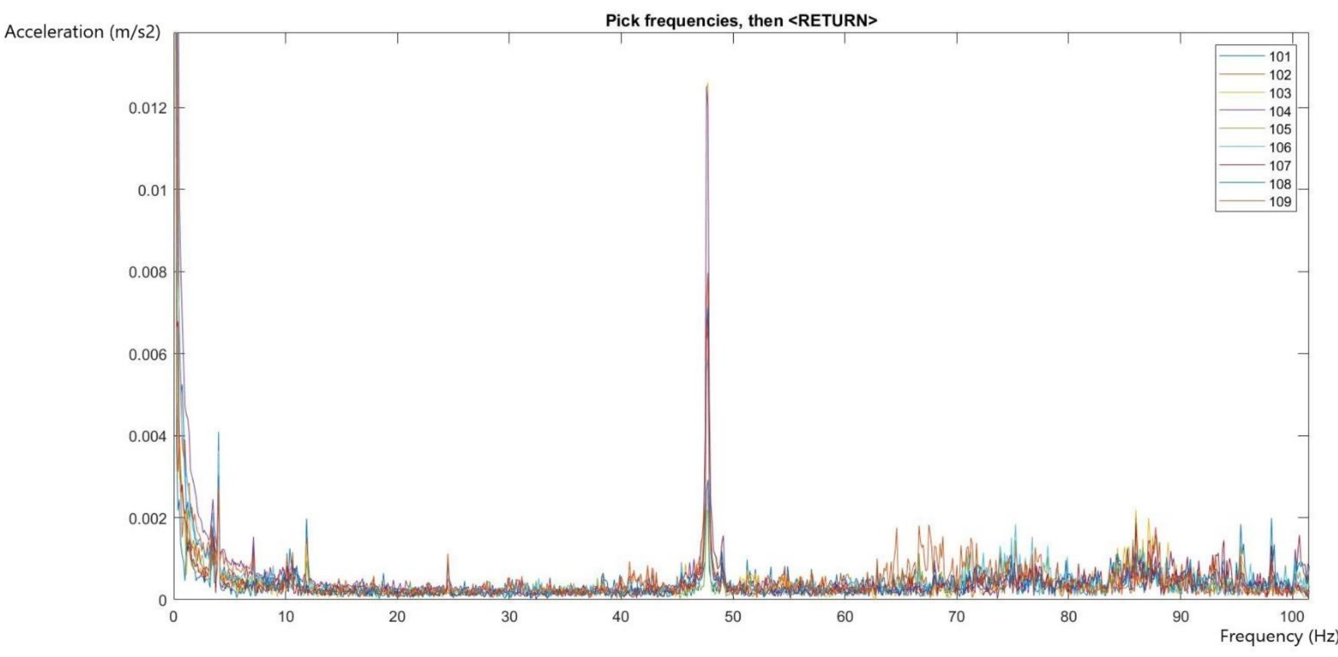

Figure 16 – Linear Frequency Plot for Global Arrangement in Air up to 100Hz at Impact Point A2

First 6 peaks:

Table 5 – Hammer Test in Air Global Arrangement

Peak 1 (Hz)	4
Peak 2 (Hz)	12
Peak 3 (Hz)	24
Peak 4 (Hz)	47
Peak 5 (Hz)	86
Peak 6 (Hz)	147

Figure 17 to Figure 25 present the coherence calculated between the force signal from the modal hammer and the acceleration signals. Additional FFTs for the hammer test in air are presented in Appendix A.1. (Figure 132 and Figure 133), followed by the coherence graphs (Figure 134 to Figure 142).

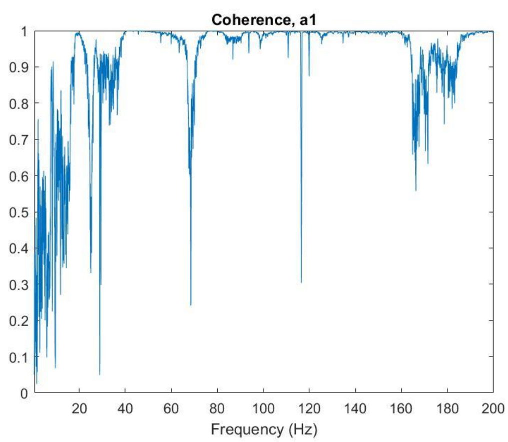

Figure 17 - Coherence Level for Accelerometer No. 1 for Global Arrangement in Air

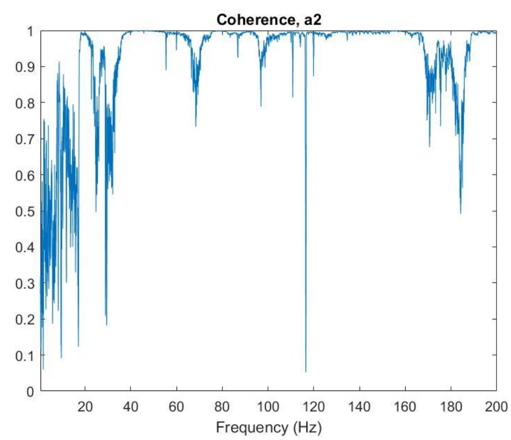

Figure 18 - Coherence Level for Accelerometer No. 2 for Global Arrangement in Air

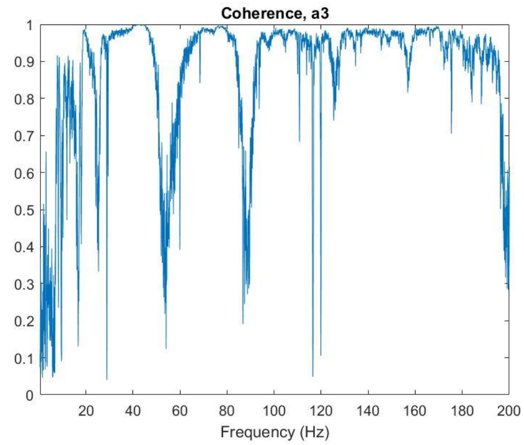

Figure 19 - Coherence Level for Accelerometer No. 3 for Global Arrangement in Air

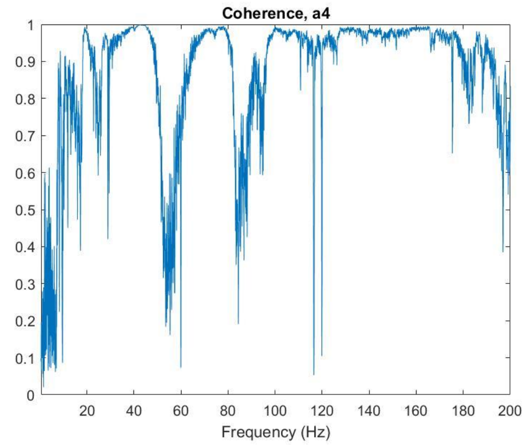

Figure 20 - Coherence Level for Accelerometer No. 4 for Global Arrangement in Air

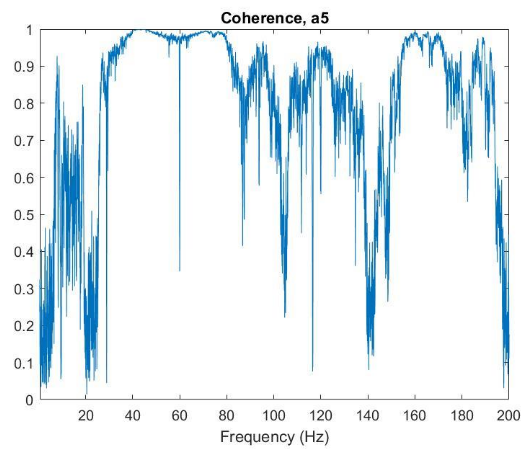

Figure 21 - Coherence Level for Accelerometer No. 5 for Global Arrangement in Air

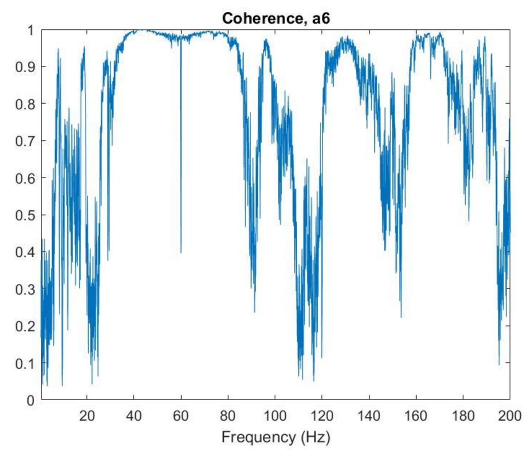

Figure 22 - Coherence Level for Accelerometer No. 6 for Global Arrangement in Air

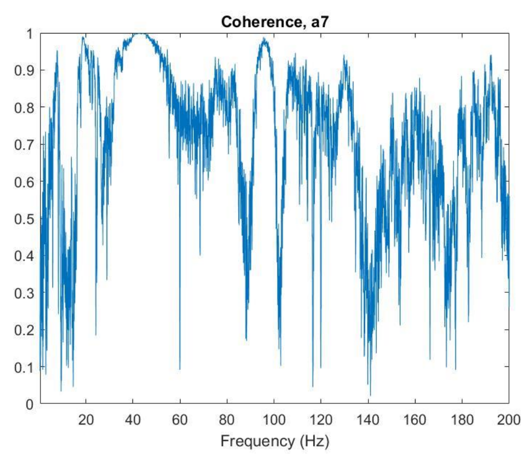

Figure 23 - Coherence Level for Accelerometer No. 7 for Global Arrangement in Air

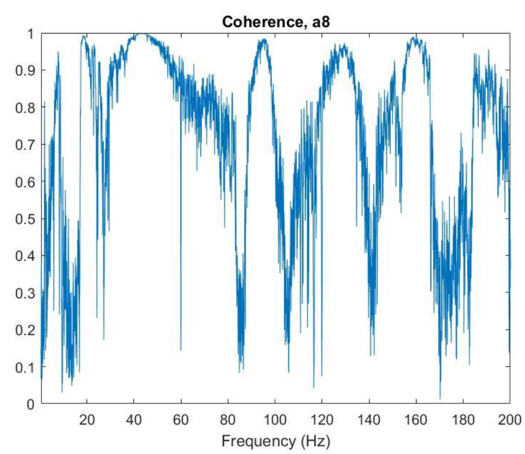

Figure 24 - Coherence Level for Accelerometer No. 8 for Global Arrangement in Air

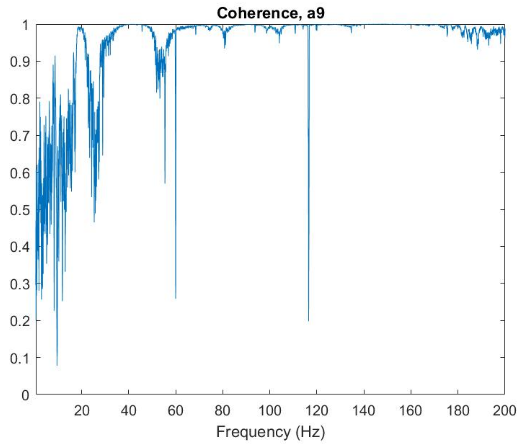

Figure 25 - Coherence Level for Accelerometer No. 9 for Global Arrangement in Air

Figure 26 to Figure 31 show the ABRAVIBE Mode Simulations for the above mentioned test.

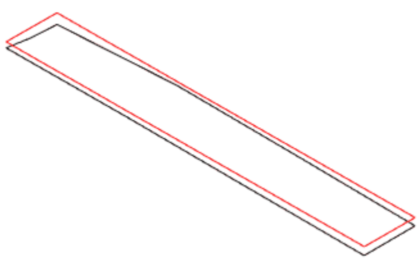

Figure 26 - ABRAVIBE Mode Simulation at 4 Hz for Global Arrangement in Air. Rigid Body Motion.

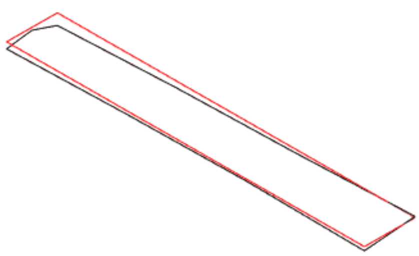

Figure 27 - ABRAVIBE Mode Simulation at 12 Hz for Global Arrangement in Air. Torsional Mode.

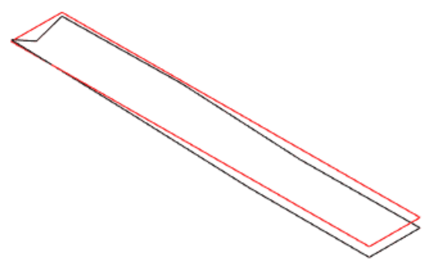

Figure 28 - ABRAVIBE Mode Simulation at 24 Hz for Global Arrangement in Air. Bending mode.

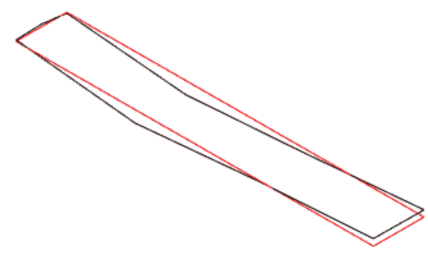

Figure 29 - ABRAVIBE Mode Simulation at 47 Hz for Global Arrangement in Air. First Bending Mode.

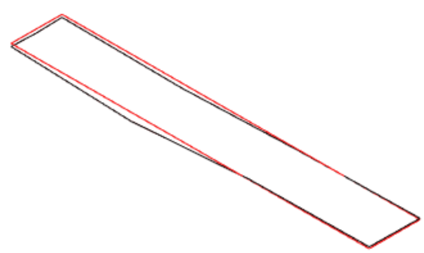

Figure 30 - ABRAVIBE Mode Simulation at 86 Hz for Global Arrangement in Air. Torsional and Bending Mode.

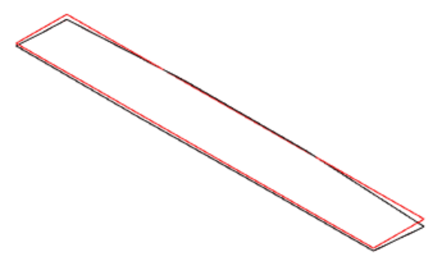

Figure 31 - ABRAVIBE Mode Simulation at 147 Hz for Global Arrangement in Air. Torsional Mode.

Figure 32 and Figure 33 present the FFT acquired by the accelerometers during the modal test in water with the global accelerometer arrangement. Table 6 presents the main peaks from the FFT and the related mode number.

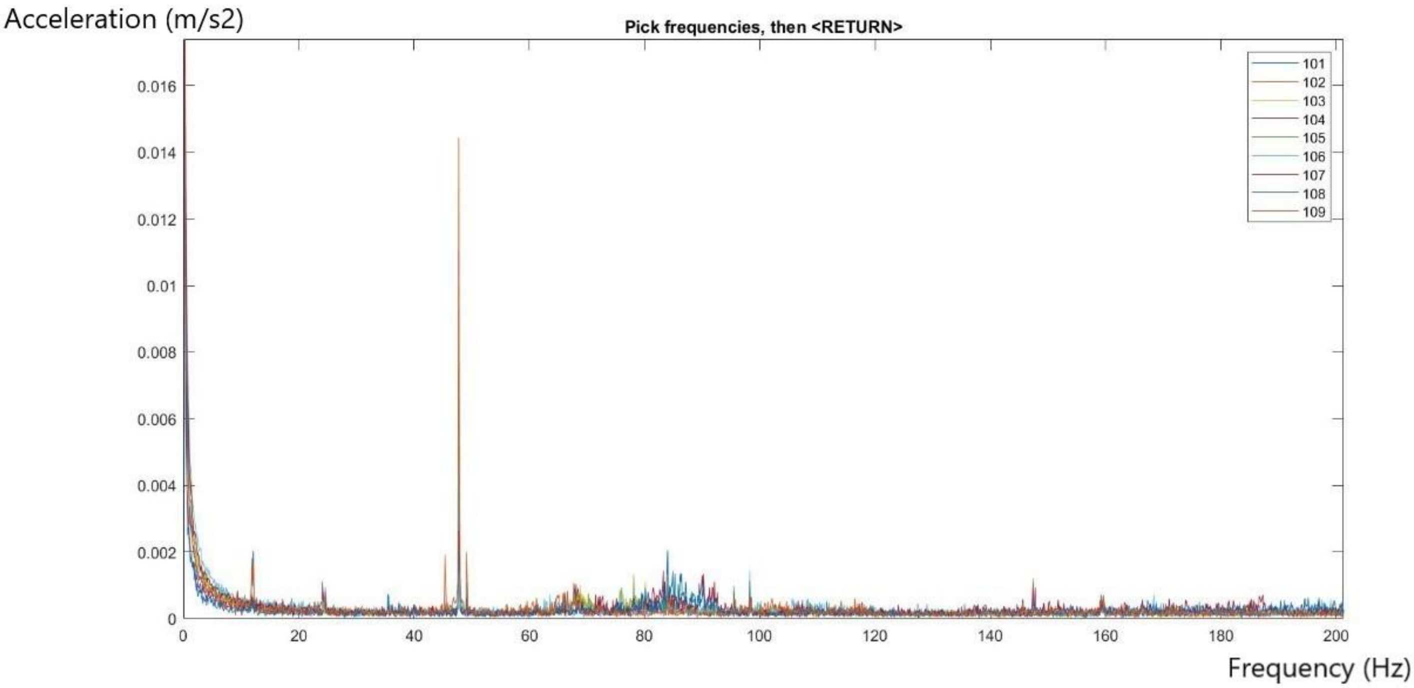

Figure 32 - Linear Frequency Plot for Global Arrangement in Water at Impact Point A2

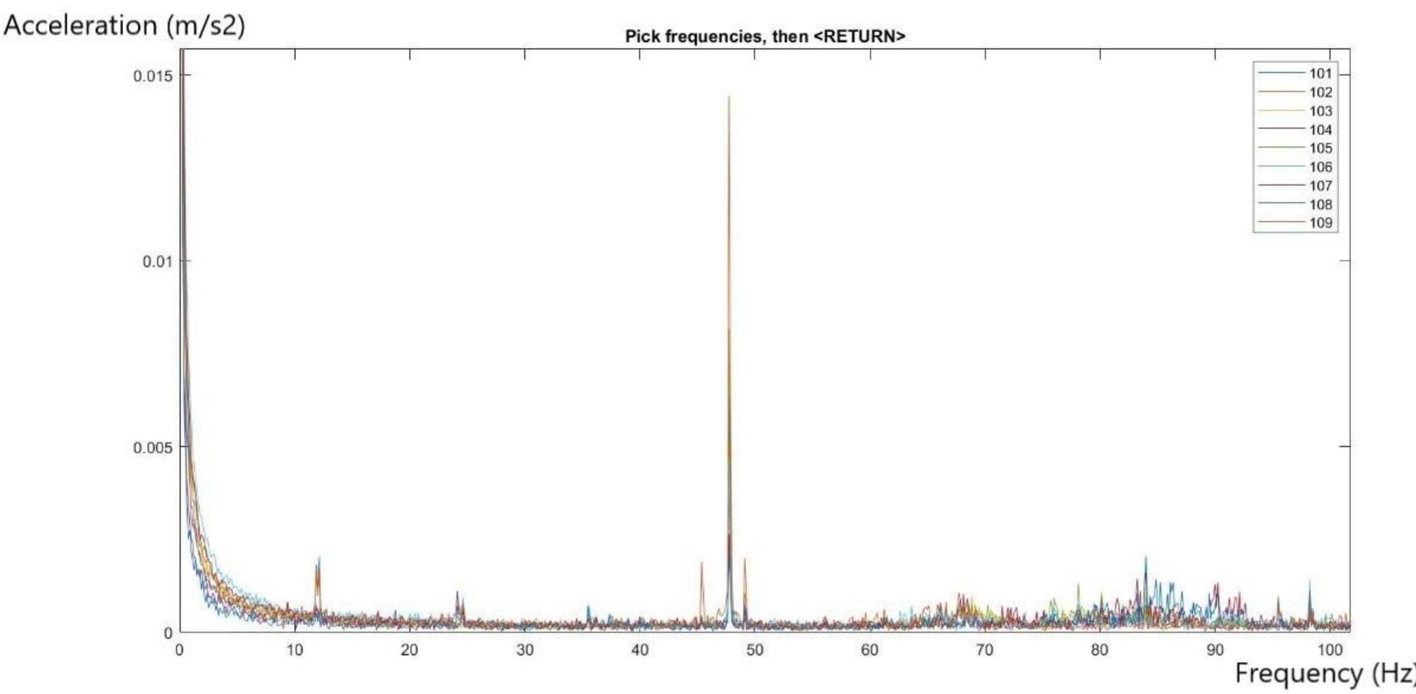

Figure 33 - Linear Frequency Plot for Global Arrangement in Water up to 100 Hz at Impact Point A2

First 6 peaks:

Table 6 – Hammer Test in Water Global Arrangement

Peak 1 (Hz)	12
Peak 2 (Hz)	24
Peak 3 (Hz)	35
Peak 4 (Hz)	47
Peak 5 (Hz)	86
Peak 6 (Hz)	147

Figure 34 to Figure 42 present the coherence calculated between the force signal from the modal hammer and the acceleration signals. Additional FFTs for the hammer test in water are presented in Appendix A.2. (Figure 143 and Figure 144), followed by the coherence graphs (Figure 145 to Figure 153).

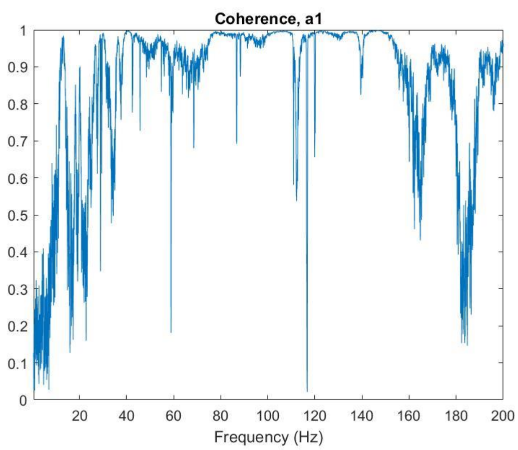

Figure 34 - Coherence Level for Accelerometer No. 1 for Global Arrangement in Water

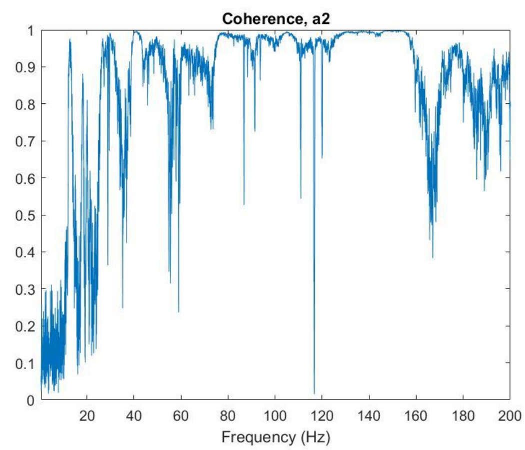

Figure 35 - Coherence Level for Accelerometer No. 2 for Global Arrangement in Water

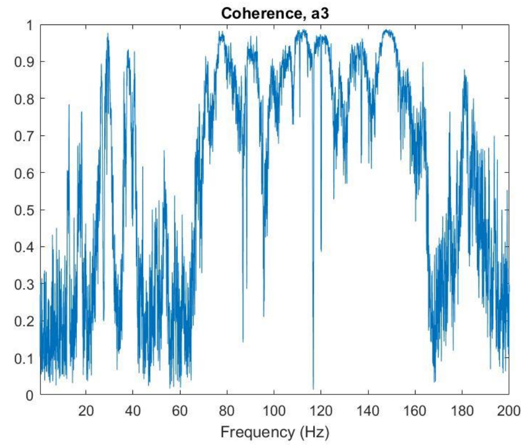

Figure 36 - Coherence Level for Accelerometer No. 3 for Global Arrangement in Water

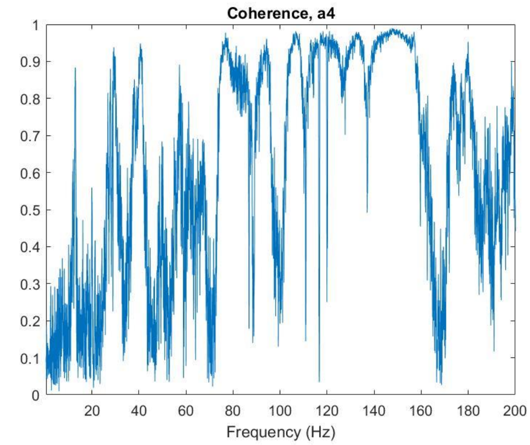

Figure 37 - Coherence Level for Accelerometer No. 4 for Global Arrangement in Water

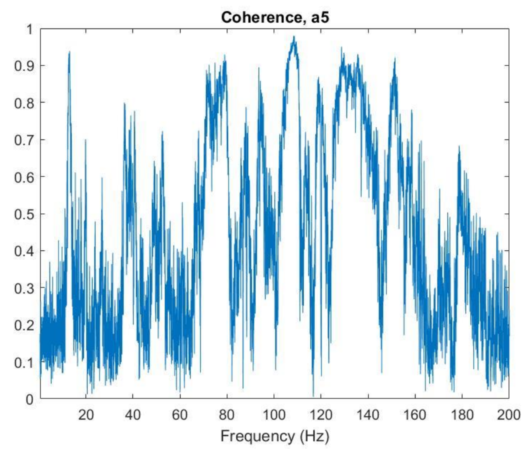

Figure 38 - Coherence Level for Accelerometer No. 5 for Global Arrangement in Water

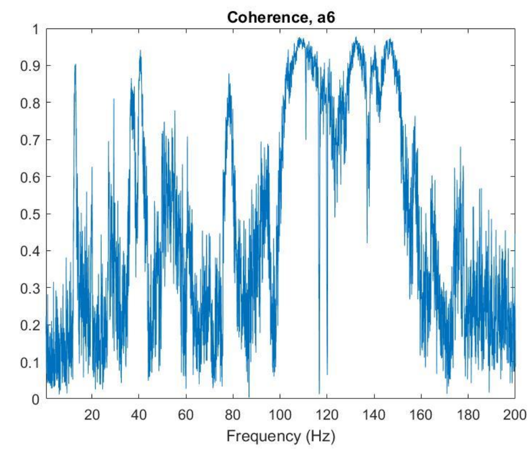

Figure 39 - Coherence Level for Accelerometer No. 6 for Global Arrangement in Water

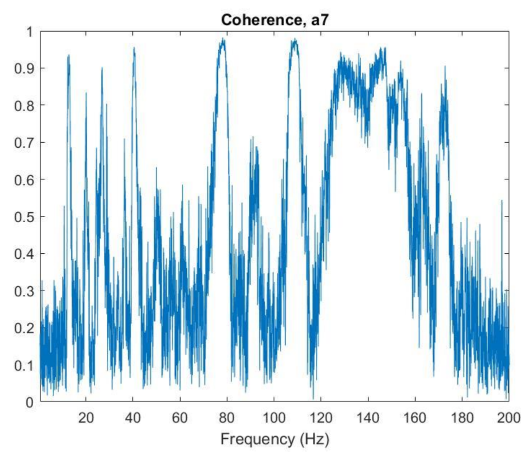

Figure 40 - Coherence Level for Accelerometer No. 7 for Global Arrangement in Water

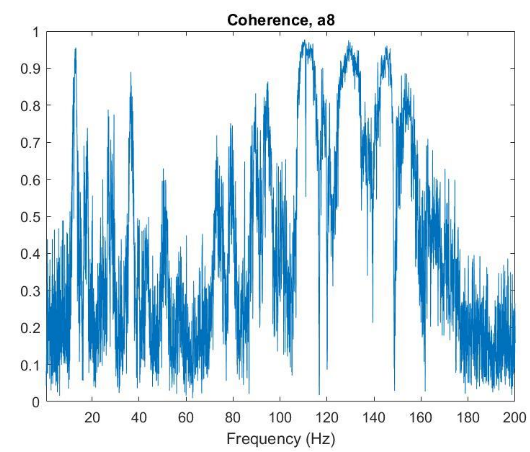

Figure 41 - Coherence Level for Accelerometer No. 8 for Global Arrangement in Water

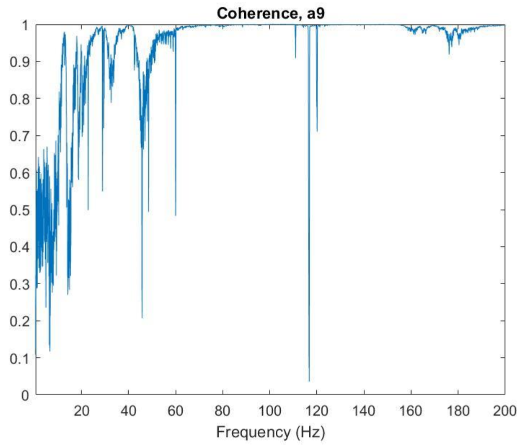

Figure 42 - Coherence Level for Accelerometer No. 9 for Global Arrangement in Water

Figure 43 to Figure 48 show ABRAVIBE Mode Simulation for the above mentioned test.

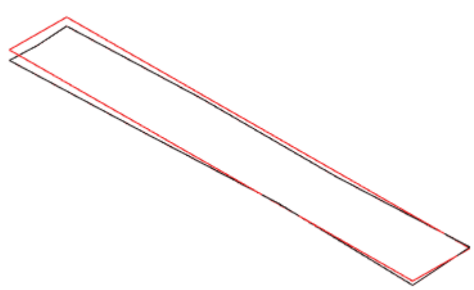

Figure 43 - ABRAVIBE Mode Simulation at 12 Hz for Global Arrangement in Water

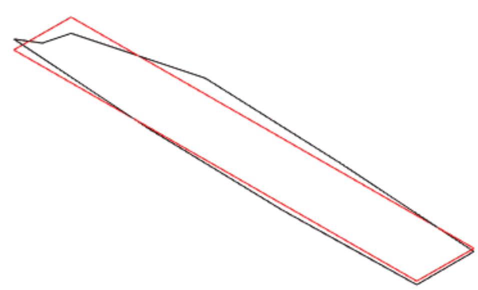

Figure 44 - ABRAVIBE Mode Simulation at 24 Hz for Global Arrangement in Water

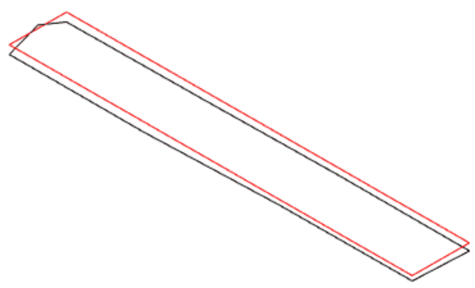

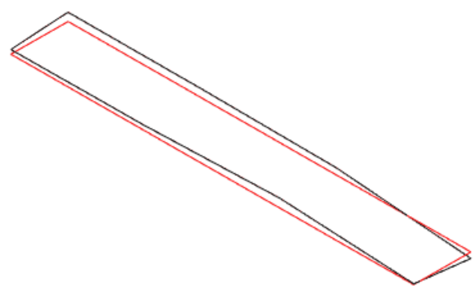

Figure 45 - ABRAVIBE Mode Simulation at 35 Hz for Global Arrangement in Water

Figure 46 - ABRAVIBE Mode Simulation at 86 Hz for Global Arrangement in Water

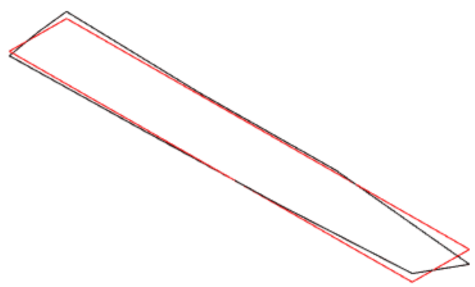

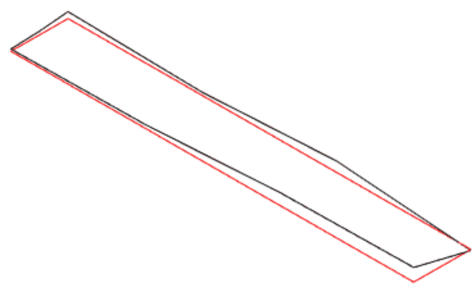

Figure 47 - ABRAVIBE Mode Simulation at 86 Hz for Global Arrangement in Water

Figure 48 - ABRAVIBE Mode Simulation at 147 Hz for Global Arrangement in Water

Figure 49 and Figure 50 present the FFT acquired by the accelerometers during the modal test in water with the local accelerometer arrangement. Table 7 presents the main peaks from the FFT and the corresponding mode number.

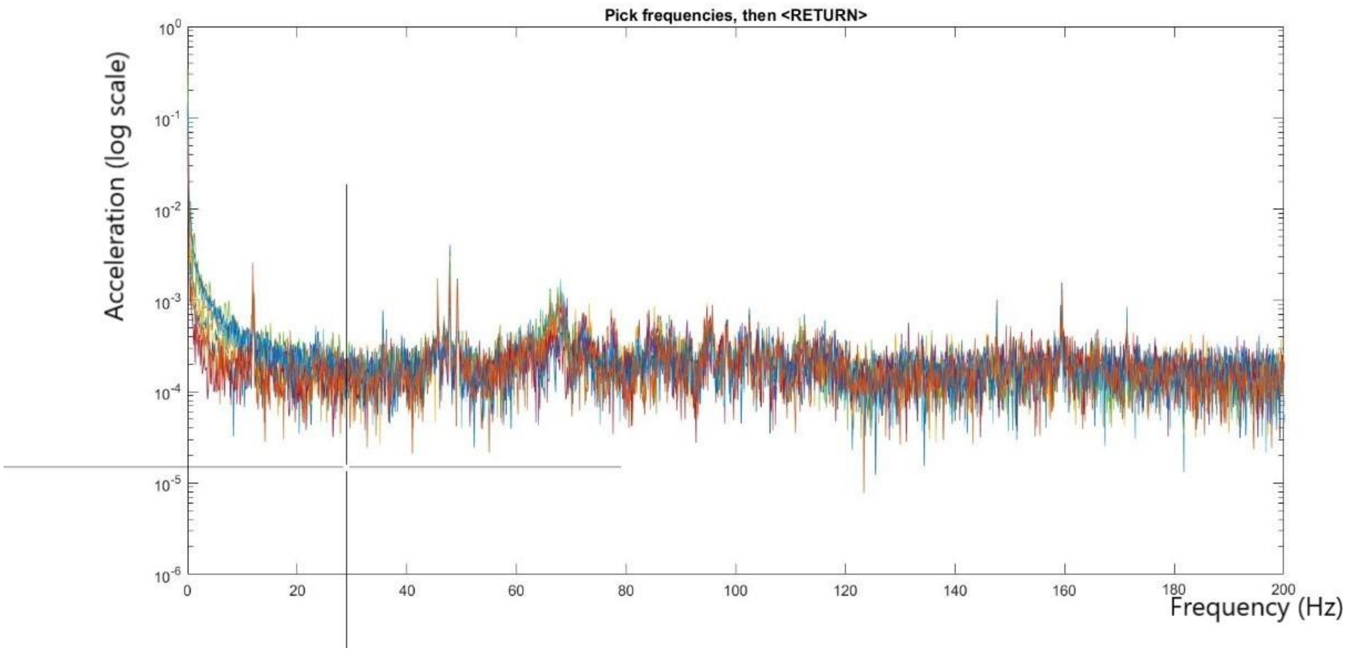

Figure 49 – Average FFT for Local Arrangement in Water at Impact Point A1

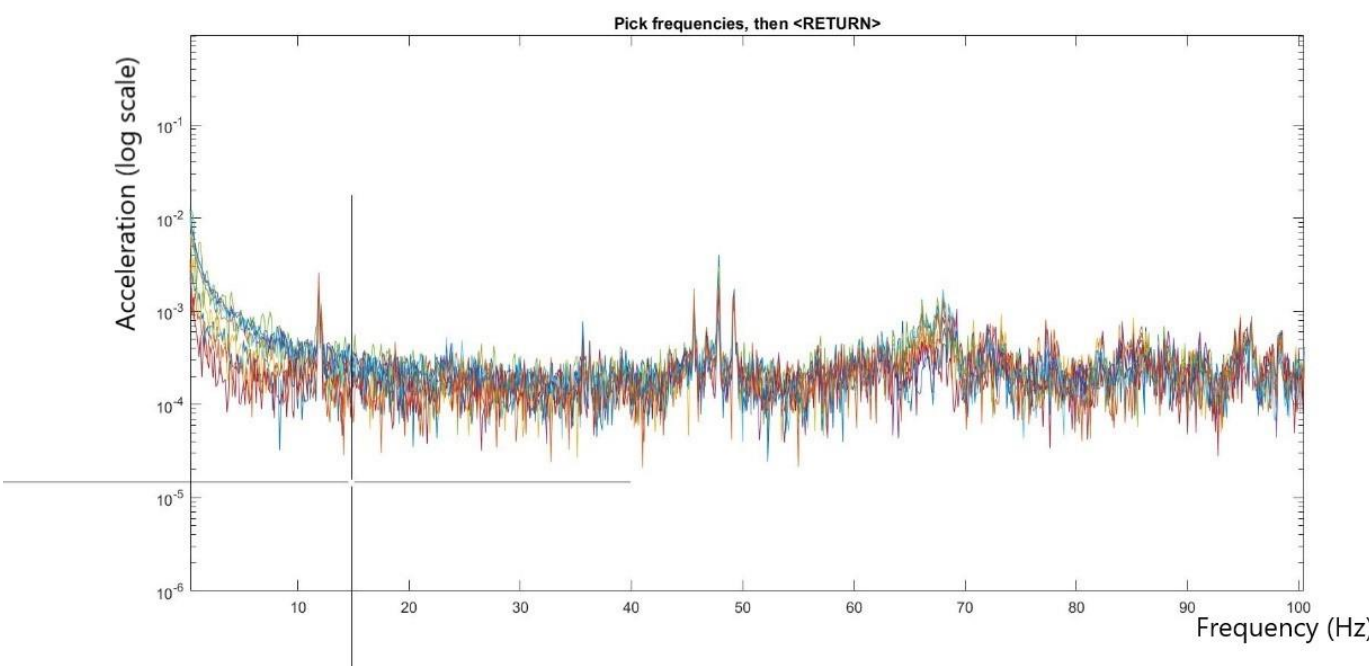

Figure 50 – Average FFT for Local Arrangement in Water at Impact Point A1 up to 100 Hz

First 6 peaks:

Table 7 – Hammer Test in Water Local Arrangement

Peak 1 (Hz)	12
Peak 2 (Hz)	23
Peak 3 (Hz)	36
Peak 4 (Hz)	48
Peak 5 (Hz)	69
Peak 6 (Hz)	96

Figure 51 to Figure 59Figure 142 present the coherence calculated between the force signal from the modal hammer and the acceleration signals.

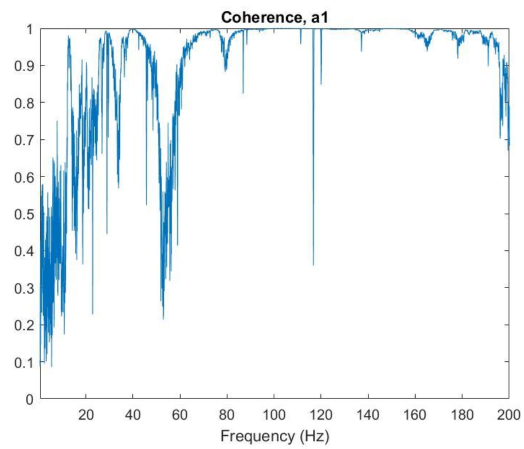

Figure 51 - Coherence Level for Accelerometer No. 1 for Local Arrangement in Water

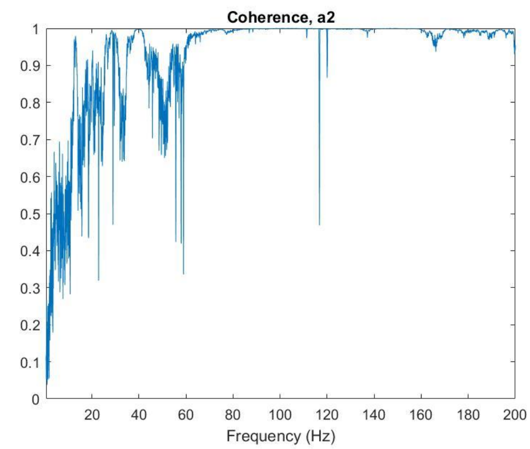

Figure 52 - Coherence Level for Accelerometer No. 2 for Local Arrangement in Water

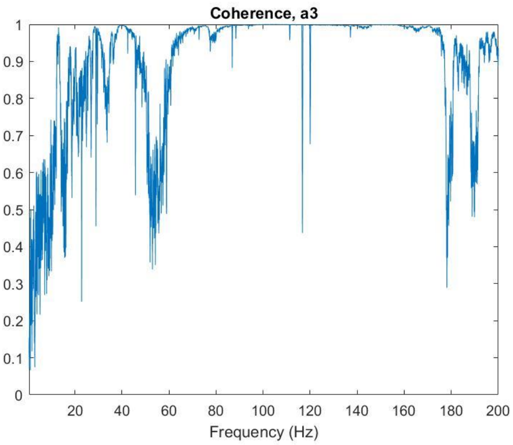

Figure 53 - Coherence Level for Accelerometer No. 3 for Local Arrangement in Water

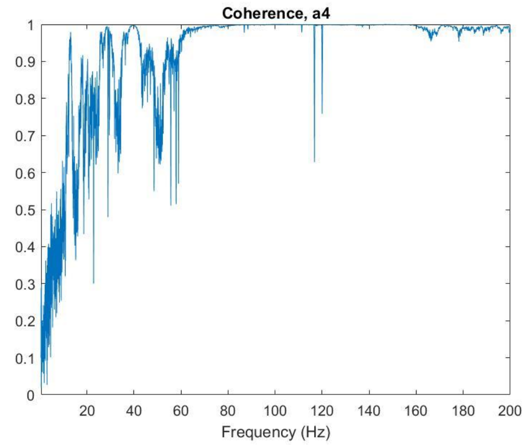

Figure 54 - Coherence Level for Accelerometer No. 4 for Local Arrangement in Water

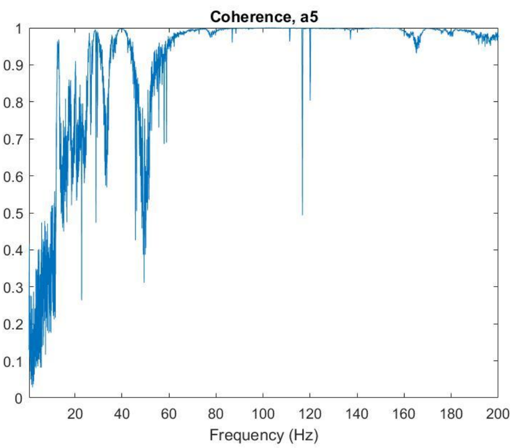

Figure 55 - Coherence Level for Accelerometer No. 5 for Local Arrangement in Water

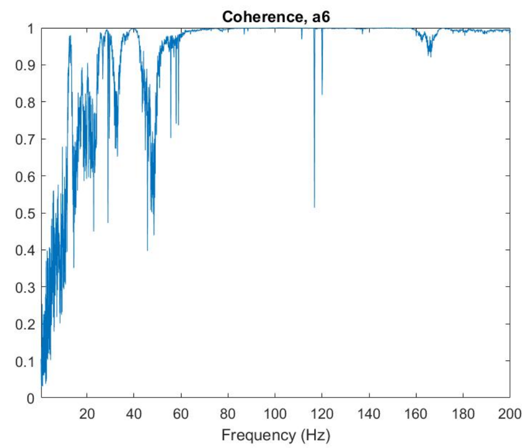

Figure 56 - Coherence Level for Accelerometer No. 6 for Local Arrangement in Water

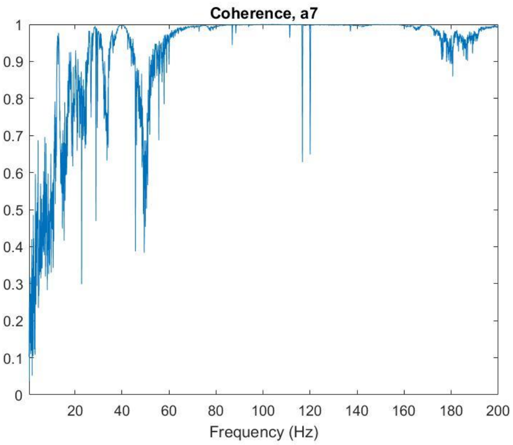

Figure 57 - Coherence Level for Accelerometer No. 7 for Local Arrangement in Water

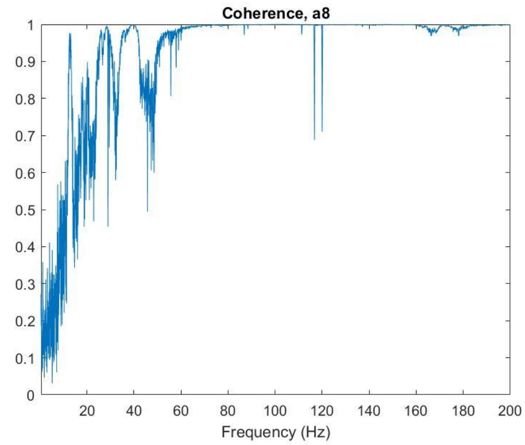

Figure 58 - Coherence Level for Accelerometer No. 7 for Local Arrangement in Water

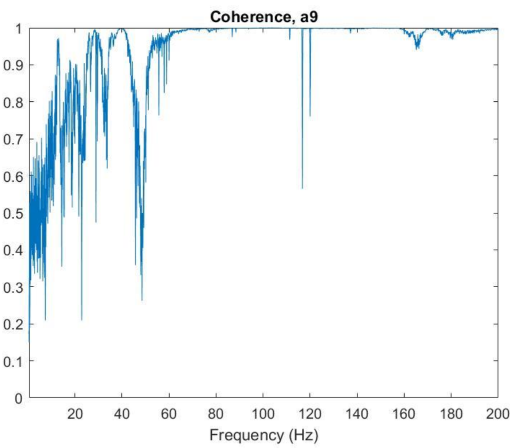

Figure 59 - Coherence Level for Accelerometer No. 9 for Local Arrangement in Water

Figure 60 to Figure 65 show ABRAVIBE Mode Simulation for the above mentioned test.

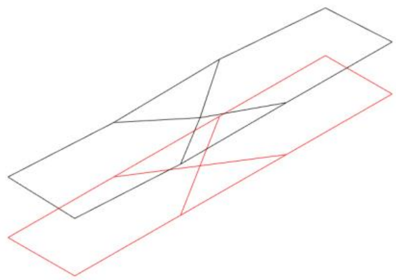

Figure 60 - ABRAVIBE Mode Simulation at 12 Hz for Local Arrangement in Water

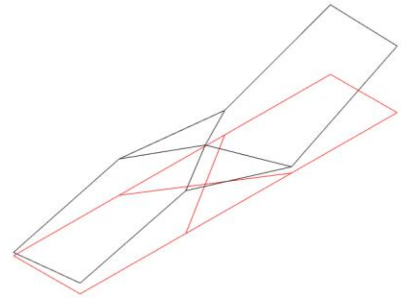

Figure 61 - ABRAVIBE Mode Simulation at 23 Hz for Local Arrangement in Water

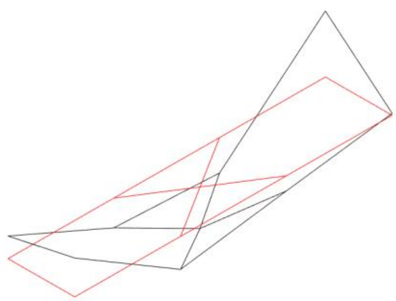

Figure 62 - ABRAVIBE Mode Simulation at 36 Hz for Local Arrangement in Water

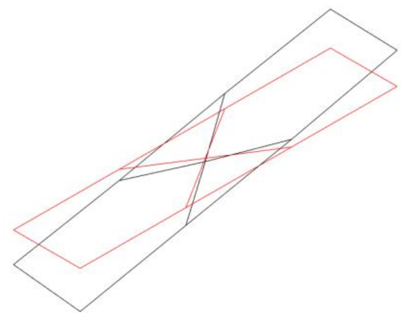

Figure 63 - ABRAVIBE Mode Simulation at 48 Hz for Local Arrangement in Water

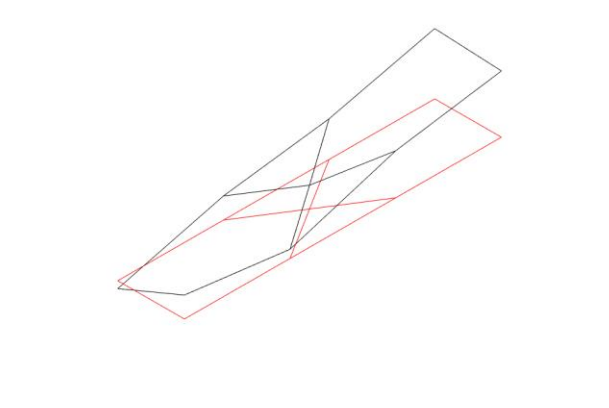

Figure 64 - ABRAVIBE Mode Simulation at 69 Hz for Local Arrangement in Water

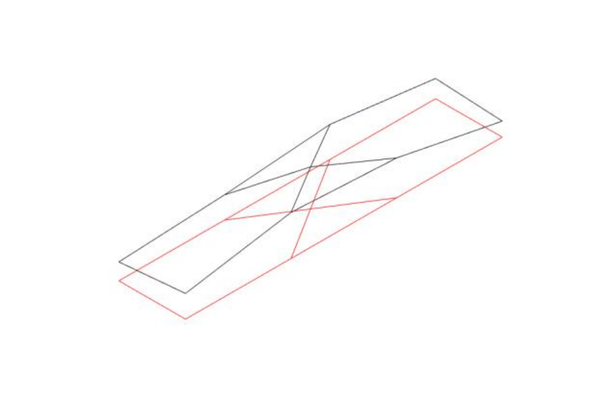

Figure 65 - ABRAVIBE Mode Simulation at 96 Hz for Local Arrangement in Water

4.1.2 Hydrodynamics Testing Results

In this section, the results of both the ODS and the Hull pressure sensors' measurements are presented.

4.1.2.1 ODS Analysis

Each of the three run types (Resistance, Bollard and Self-Propulsion) were analyzed over a minimum of several different speeds. The time-domain signal accelerometers FFT are presented for each run. At the end of the ODS analysis, a table that summarizes the ODS at Blade Passing Frequencies for several run types and speeds is also shown.

First, Figure 66 and Figure 76 present the time domain signal acquired by the accelerometers during the Resistance test in water with the global accelerometer arrangement for both 0.917 m/s and 1.101 m/s, respectively

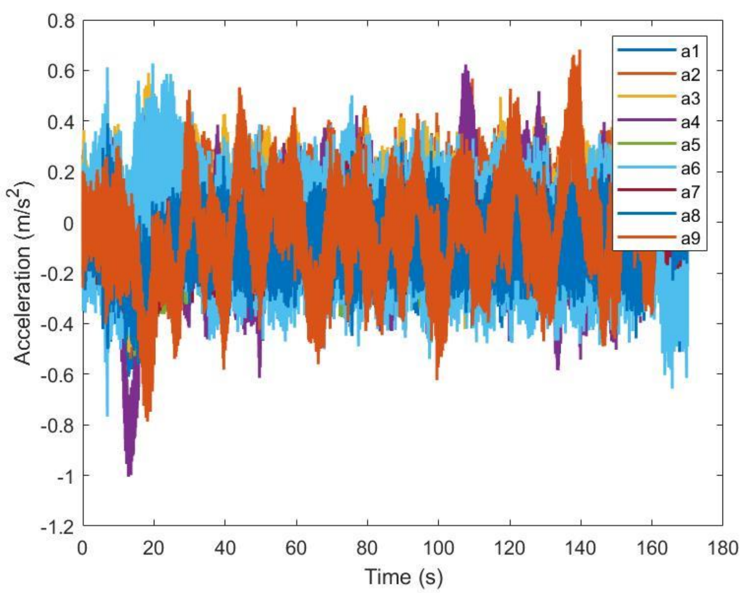

Figure 66 – Accelerometer Time Domain Signal for Global Arrangement at V_M= 0.917 m/s

Figure 67 to Figure 75 present the average FFT for the signal acquired by the accelerometers at the speed of 0.917 m/s, while Figure 77 to Figure 85 present the average FFT at the speeds of 1.101 m/s.

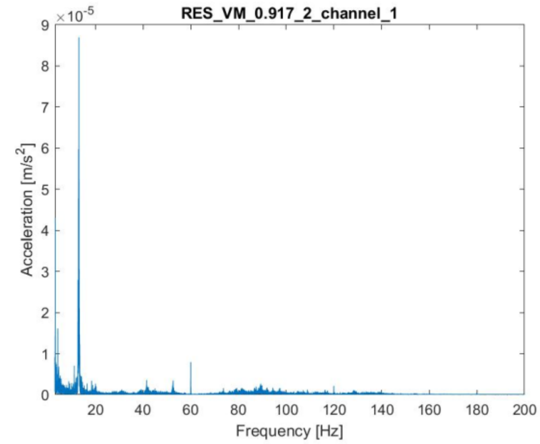

Figure 67 – Average FFT at V_M=0.917 m/s for Accelerometer No. 1 for Resistance Test in Global Arrangement in Water

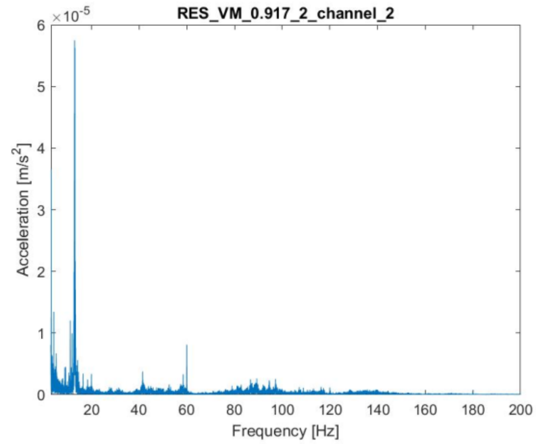

Figure 68 - Average FFT at V_M=0.917 m/s for Accelerometer No. for Resistance Test in Global Arrangement in Water

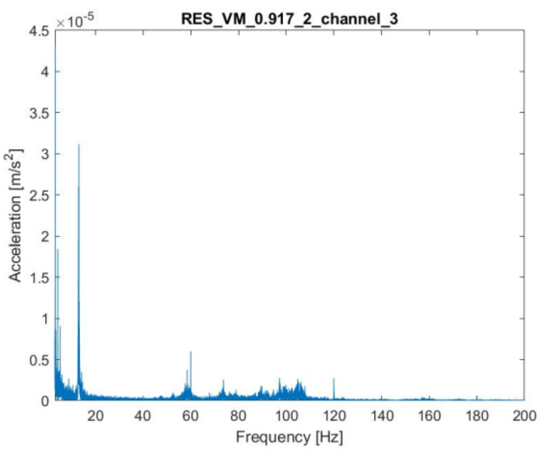

Figure 69 - Average FFT at V_M=0.917 m/s for Accelerometer No.3 for Resistance Test in Global Arrangement in Water

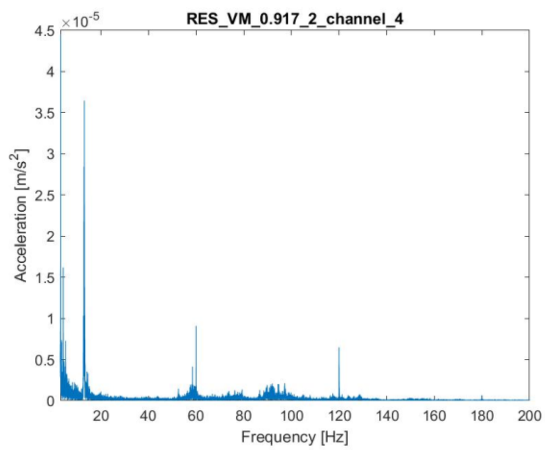

Figure 70 - Average FFT at V_M=0.917 m/s for Accelerometer No. 4 for Resistance Test in Global Arrangement in Water

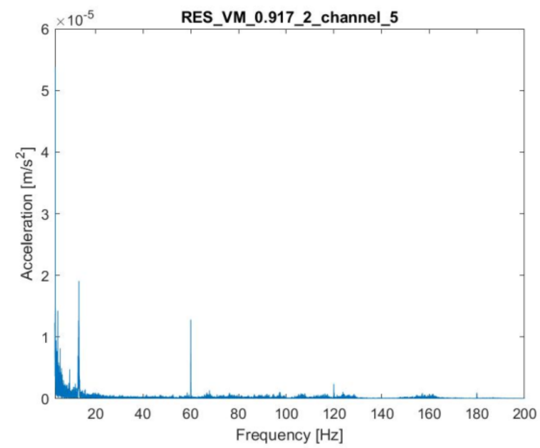

Figure 71 - Average FFT at V_M=0.917 m/s for Accelerometer No. 5 for Resistance Test in Global Arrangement in Water

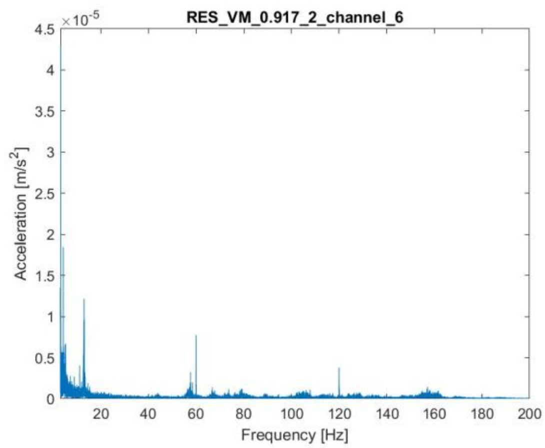

Figure 72 - Average FFT at V_M=0.917 m/s for Accelerometer No. 6 for Resistance Test in Global Arrangement in Water

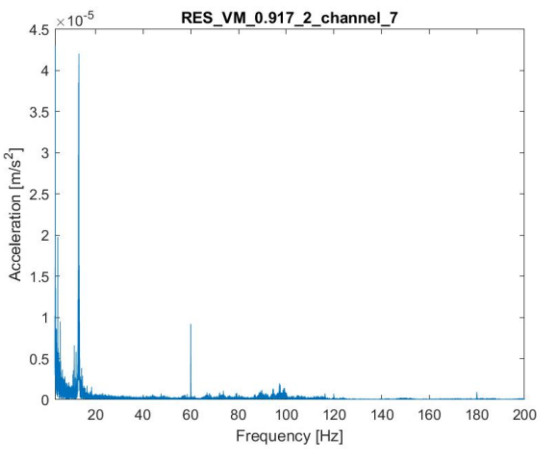

Figure 73 - Average FFT at V_M=0.917 m/s for Accelerometer No. 7 for Resistance Test in Global Arrangement in Water

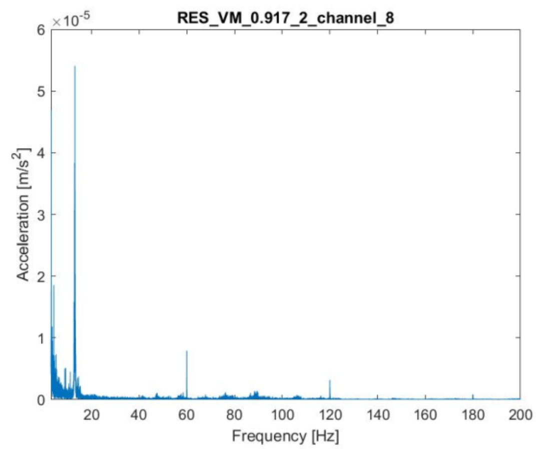

Figure 74 - Average FFT at V_M=0.917 m/s for Accelerometer No. 8 for Resistance Test in Global Arrangement in Water

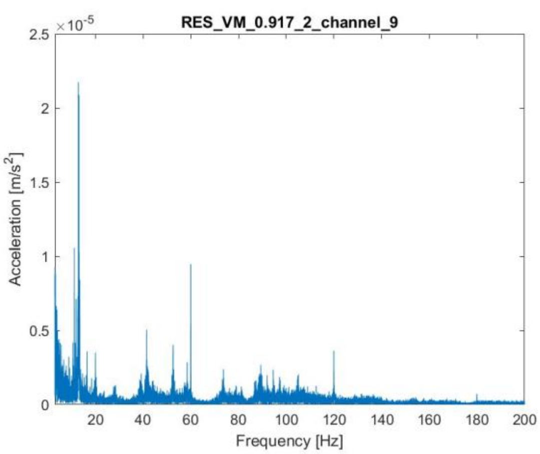

Figure 75 - Average FFT at V_M=0.917 m/s for Accelerometer No. 9 for Resistance Test in Global Arrangement in Water

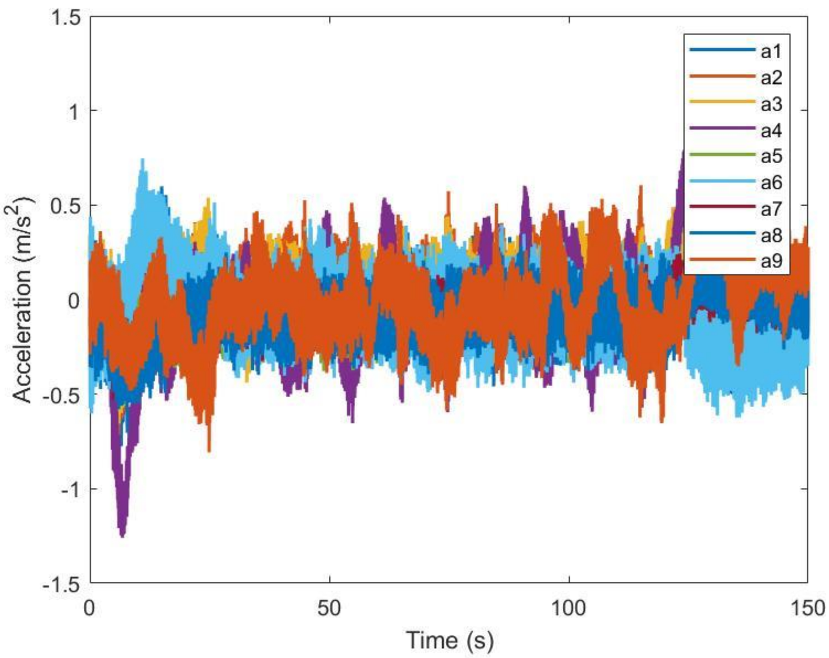

Figure 76 - Accelerometer Time Domain Signal for Global Arrangement

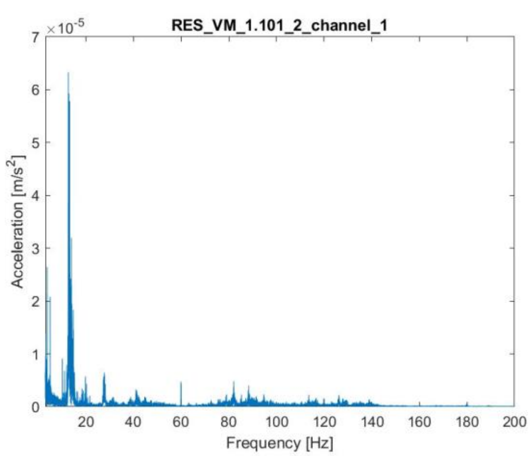

Figure 77 - Average FFT at V_M=1.101 m/s for Accelerometer No. 1 for Resistance Test in Global Arrangement in Water

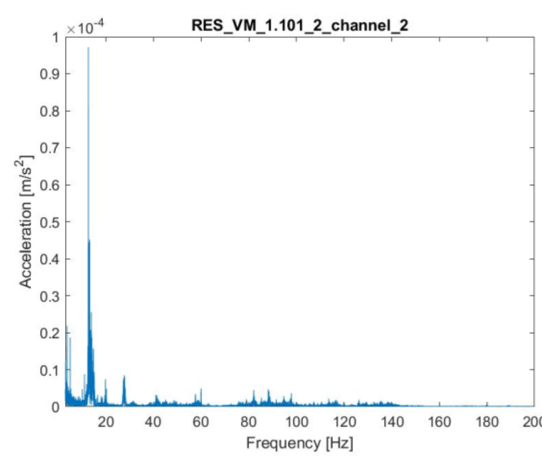

Figure 78 - Average FFT at V_M=1.101 m/s for Accelerometer No. 2 for Resistance Test in Global Arrangement in Water

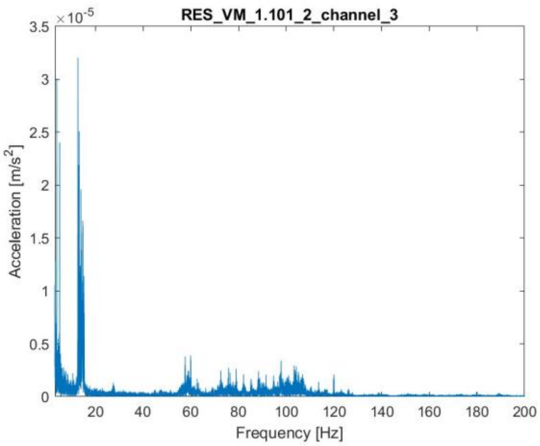

Figure 79 - Average FFT at V_M=1.101 m/s for Accelerometer No. 3 for Resistance Test in Global Arrangement in Water

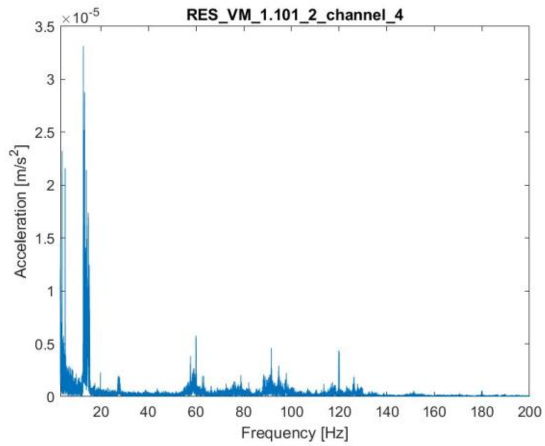

Figure 80 - Average FFT at V_M=1.101 m/s for Accelerometer No.4 for Resistance Test in Global Arrangement in Water

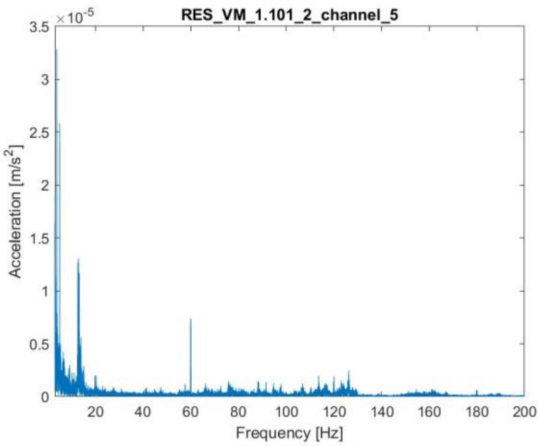

Figure 81 - Average FFT at V_M=1.101 m/s for Accelerometer No. 5 for Resistance Test in Global Arrangement in Water

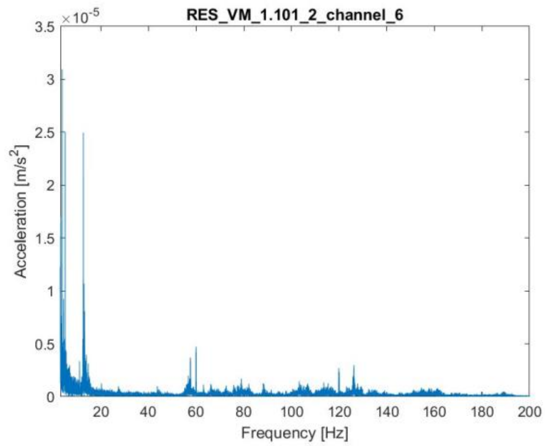

Figure 82 - Average FFT at V_M=1.101 m/s for Accelerometer No. 6 for Resistance Test in Global Arrangement in Water

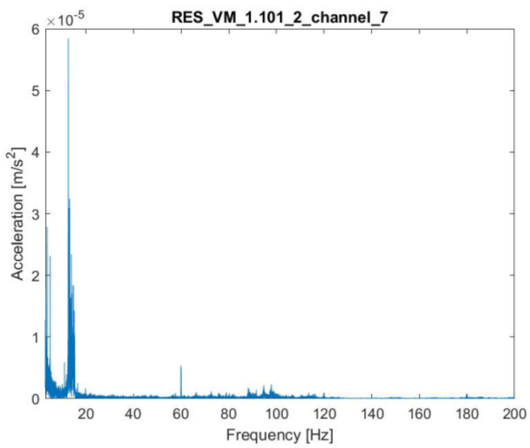

Figure 83 - Average FFT at V_M=1.101 m/s for Accelerometer No. 7 for Resistance Test in Global Arrangement in Water

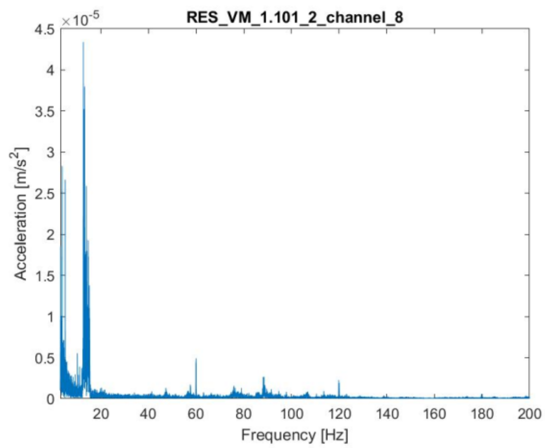

Figure 84 - Average FFT at V_M=1.101 m/s for Accelerometer No. 8 for Resistance Test in Global Arrangement in Water

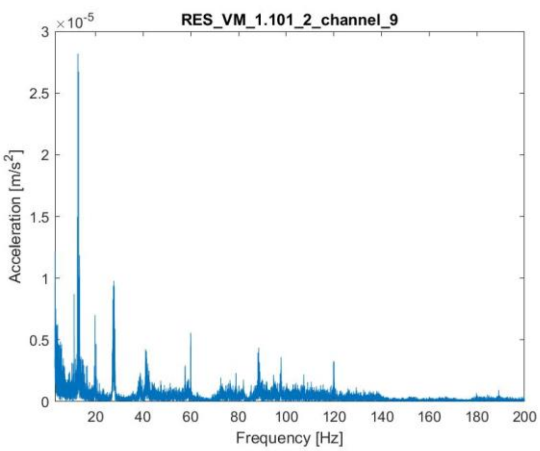

Figure 85 - Average FFT at V_M=1.101 m/s for Accelerometer No. 9 for Resistance Test in Global Arrangement in Water

Secondly, Figure 86 presents the time domain signal acquired by the accelerometers during the Bollard test in water, with the global accelerometer arrangement, for a propeller speed of 0-14 RPS.

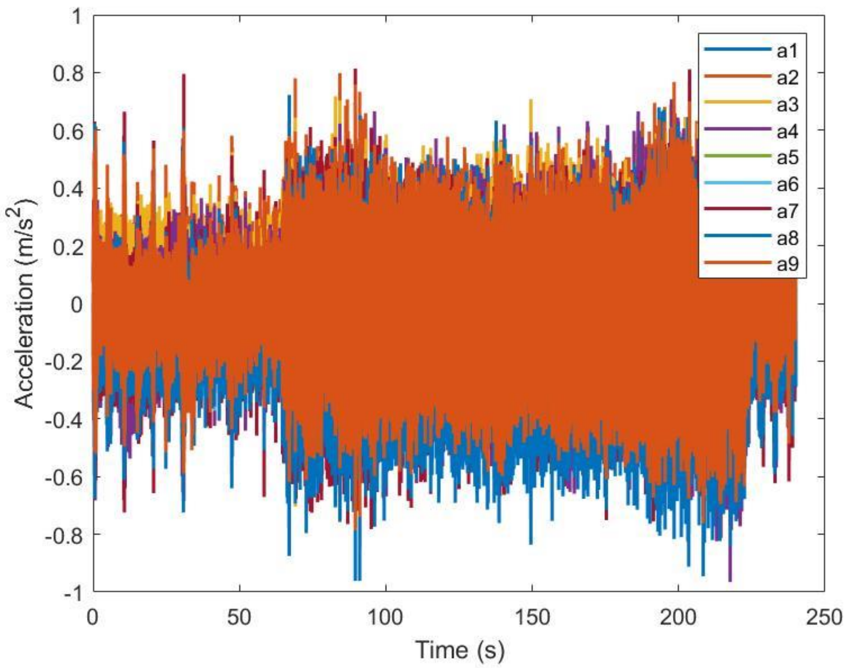

Figure 86 - Accelerometer Time Domain Signal for Global Arrangement at 0-14 RPS

Figure 87 to Figure 95Figure 142 present the average FFT for the signal acquired by the accelerometers during this test.

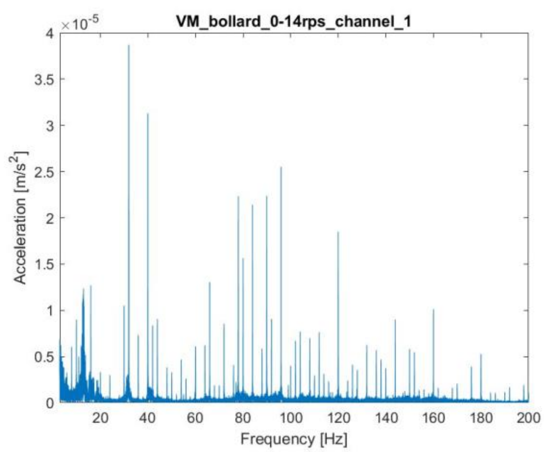

Figure 87 - Average FFT at 0 to 14 RPS for Accelerometer No.1 for Bollard test in Global Arrangement in Water

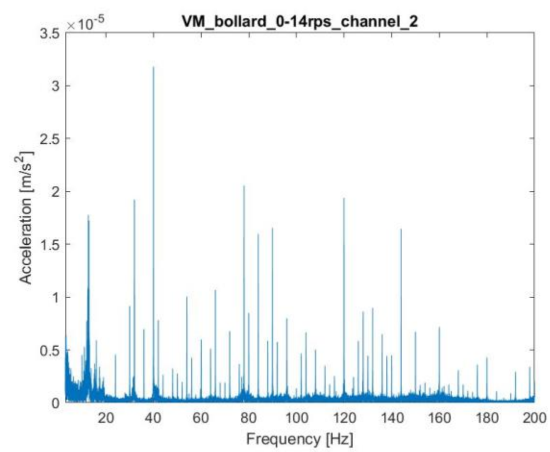

Figure 88 - Average FFT at 0 to 14 RPS for Accelerometer No.2 for Bollard test in Global Arrangement in Water

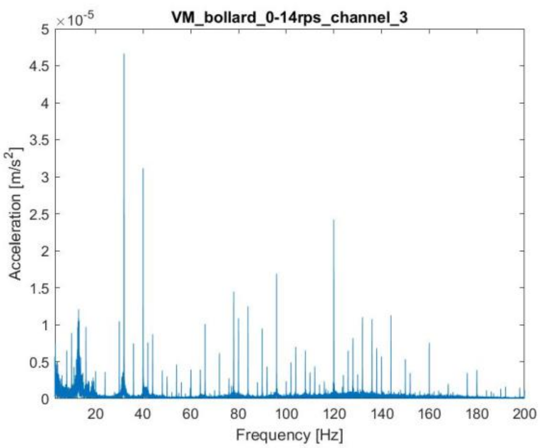

Figure 89 -Average FFT at 0 to 14 RPS for Accelerometer No.3 for Bollard test in Global Arrangement in Water

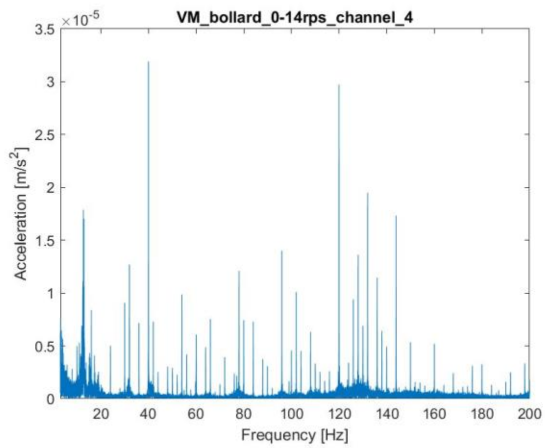

Figure 90 - Average FFT at 0 to 14 RPS for Accelerometer No.4 for Bollard test in Global Arrangement in Water

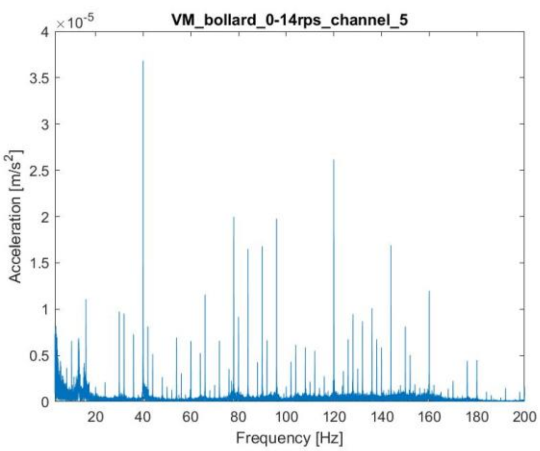

Figure 91 - Average FFT at 0 to 14 RPS for Accelerometer No.5 for Bollard test in Global Arrangement in Water

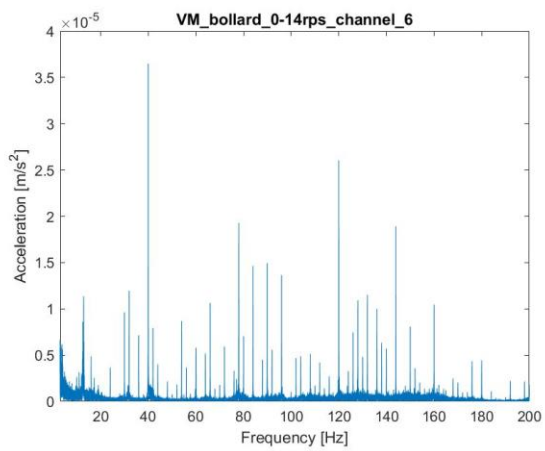

Figure 92 - Average FFT at 0 to 14 RPS for Accelerometer No.6 for Bollard test in Global Arrangement in Water

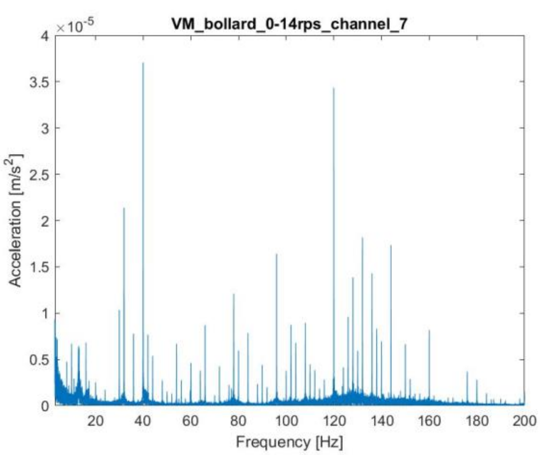

Figure 93 - Average FFT at 0 to 14 RPS for Accelerometer No.7 for Bollard test in Global Arrangement in Water

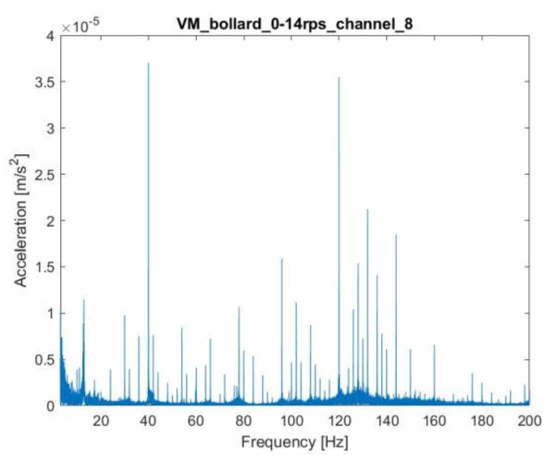

Figure 94 - Average FFT at 0 to 14 RPS for Accelerometer No.8 for Bollard test in Global Arrangement in Water

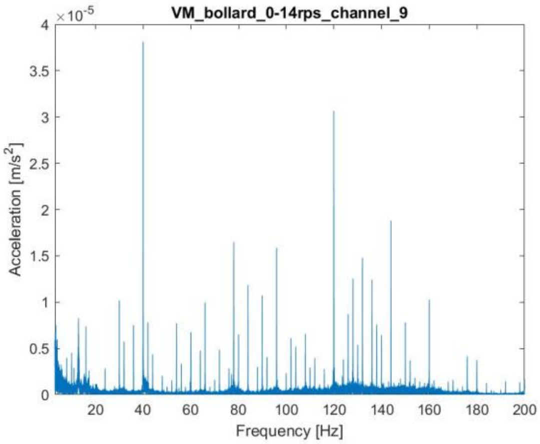

Figure 95 - Average FFT at 0 to 14 RPS for Accelerometer No. 9 for Bollard test in Global Arrangement in Water

Thirdly, Figure 96, Figure 106 and Figure 116 present the time domain signal acquired by the accelerometers during the Self-Propulsion test. This test is in water with the global accelerometer arrangement for both 0.917 m/s with propeller speed of 4.45 RPS, 0.917 m/s with propeller speeds of 12 RPS and 1.101 m/s with propeller speed of 6 RPS, respectively.

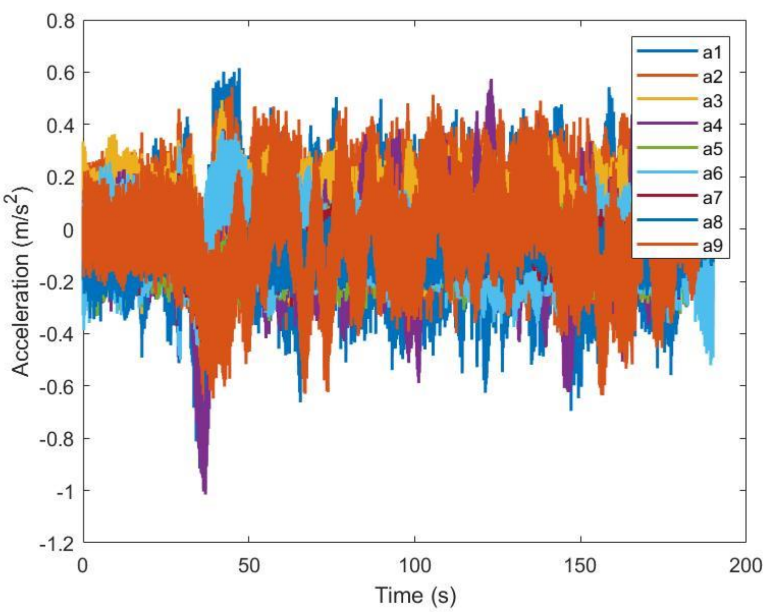

Figure 96 - Accelerometer Time Domain Signal for Global Arrangement at V_M=0.917 m/s and 4.45 RPS

Figure 97 to Figure 105Figure 142 present the average FFT for the signal acquired by the accelerometers at the speed of 0.917 m/s with 4.45 RPS, while Figure 107 to Figure 115 present the average FFT at the speeds of 0.9171 m/s with 12 RPS. Figure 117 to Figure 125 present the same speed of 1.101 m/s with the propeller speed of 6 RPS.

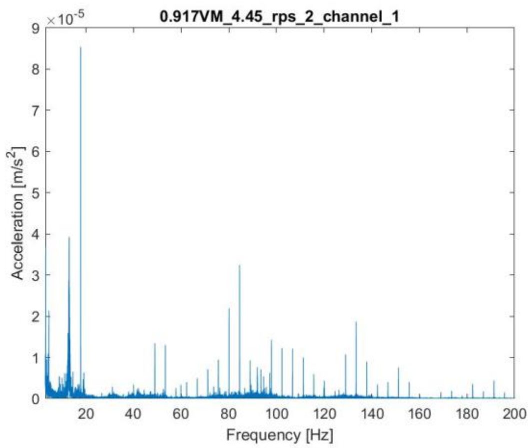

Figure 97 - FFT Signal at V_M= 0.917 m/s and 4.45 RPS for Accelerometer No. 1 in the Global Arrangement

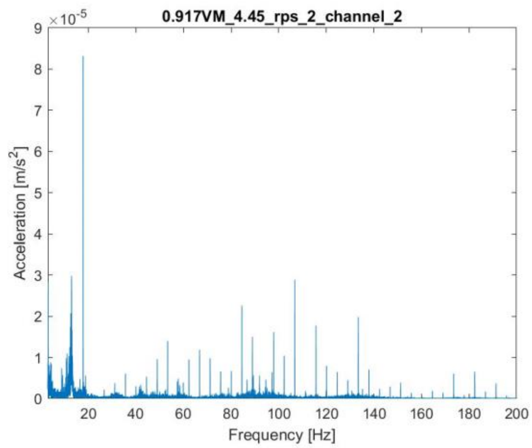

Figure 98 - FFT Signal at V_M=0.917 m/s and 4.45 RPS for Accelerometer No. 2 in the Global Arrangement

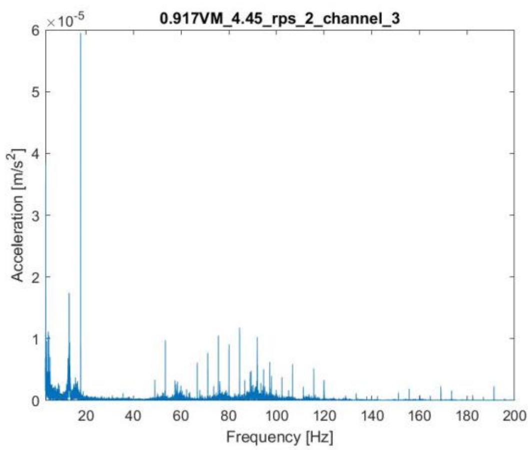

Figure 99 - FFT Signal at V_M=0.917 m/s and 4.45 RPS for Accelerometer No. 3 in the Global Arrangement

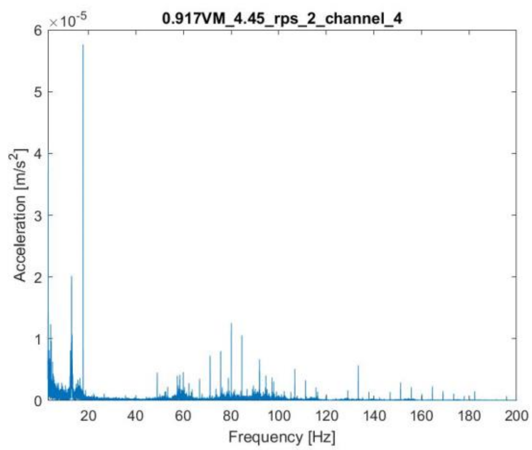

Figure 100 - FFT Signal at V_M=0.917 m/s and 4.45 RPS for Accelerometer No. 4 in the Global Arrangement

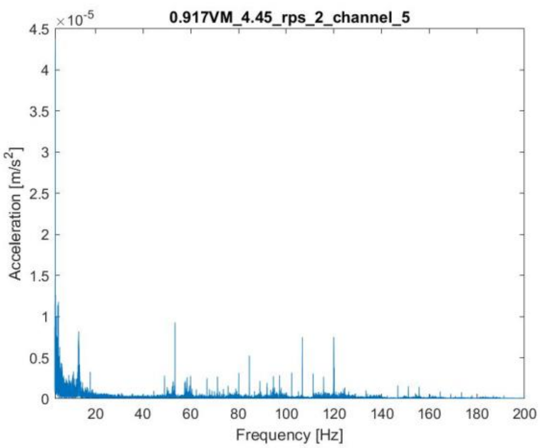

Figure 101 - FFT Signal at V_M=0.917 m/s and 4.45 RPS for Accelerometer No. 5 in the Global Arrangement

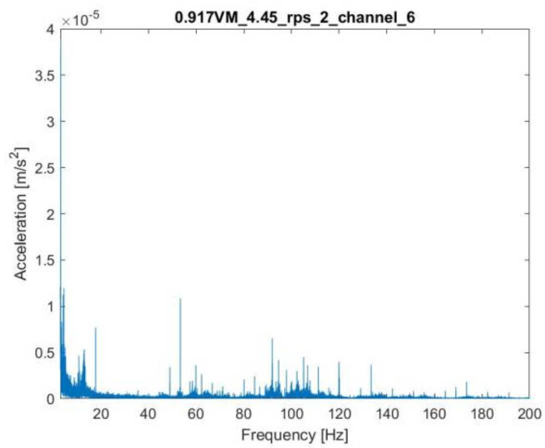

Figure 102 - FFT Signal at V_M=0.917 m/s and 4.45 RPS for Accelerometer No. 6 in the Global Arrangement

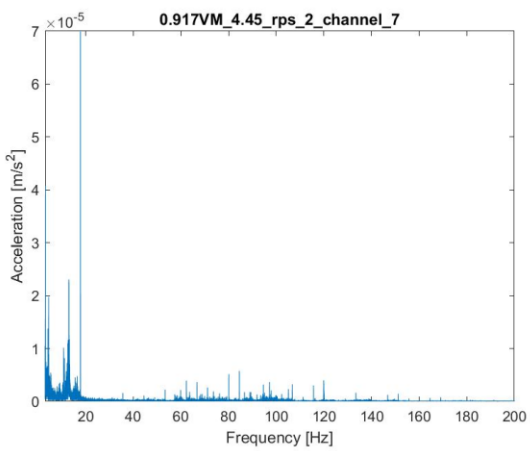

Figure 103 - FFT Signal at V_M=0.917 m/s and 4.45 RPS for Accelerometer No. 7 in the Global Arrangement

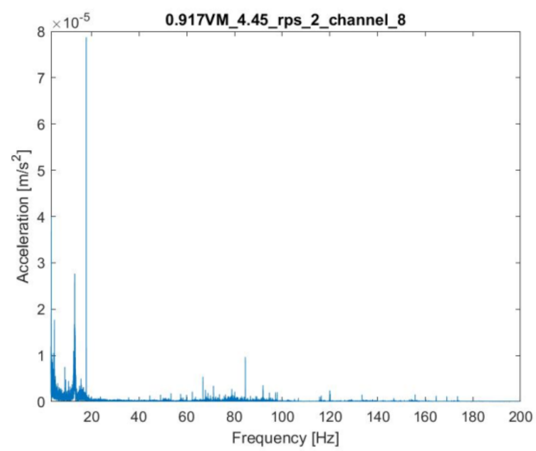

Figure 104 - FFT Signal at V_M=0.917 m/s and 4.45 RPS for Accelerometer No. 8 in the Global Arrangement

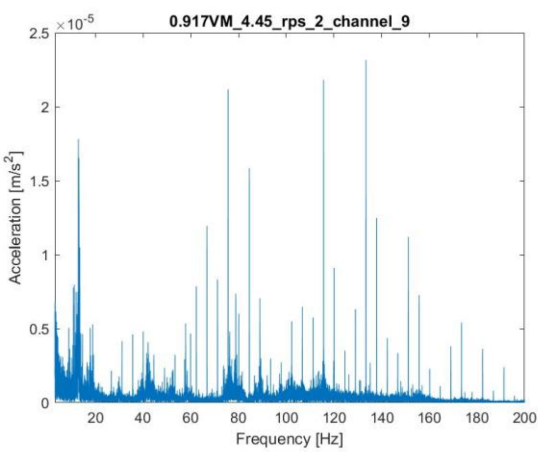

Figure 105 - FFT Signal at V_M=0.917 m/s and 4.45 RPS for Accelerometer No. 9 in the Global Arrangement

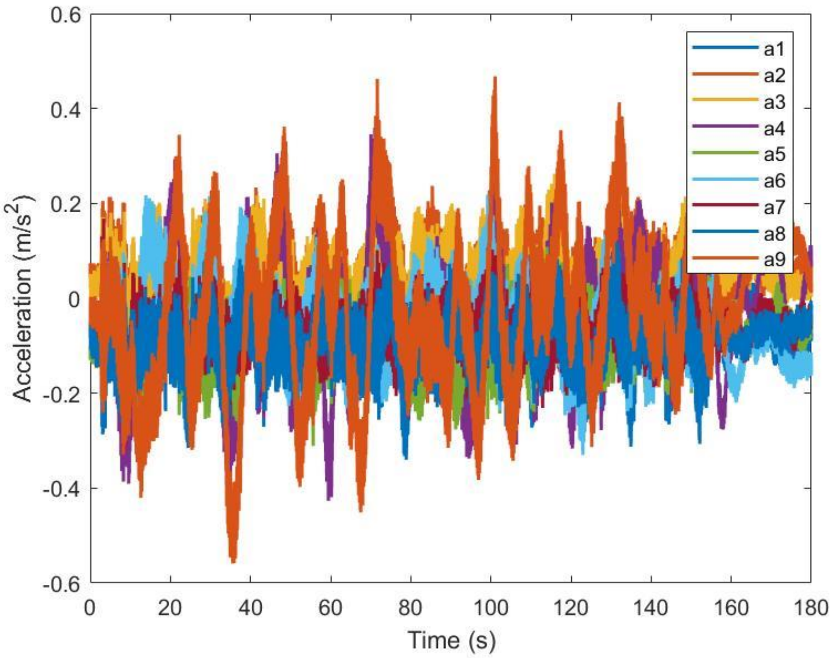

Figure 106 - Accelerometer Time Domain Signal for Global Arrangement at V_M=0.917 m/s and 12 RPS

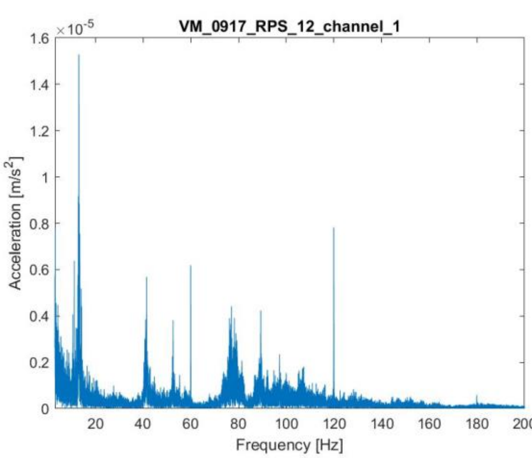

Figure 107 - FFT Signal at V_M=0.917 m/s and 12 RPS for Accelerometer No. 1 in the Global Arrangement

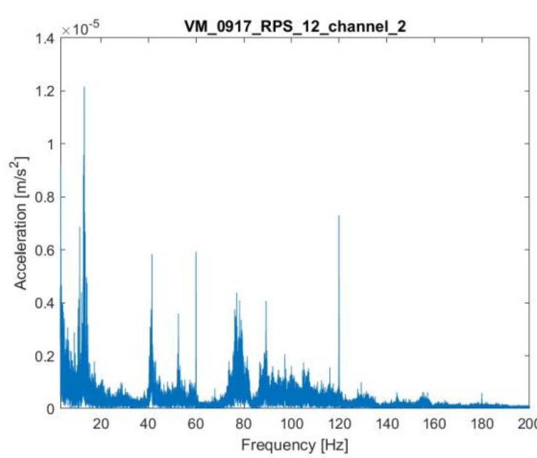

Figure 108 - FFT Signal at V_M=0.917 m/s and 12 RPS for Accelerometer No. 2 in the Global Arrangement

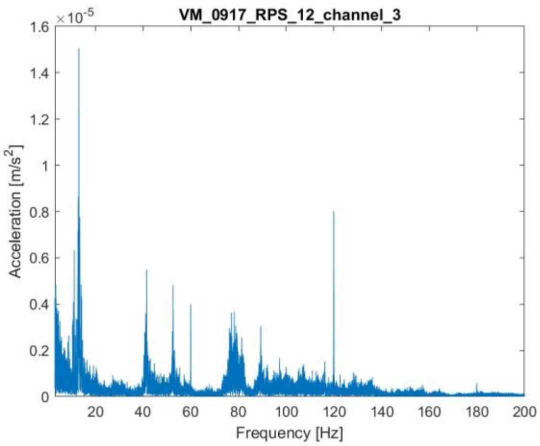

Figure 109 - FFT Signal at V_M=0.917 m/s and 12 RPS for Accelerometer No. 3 in the Global Arrangement

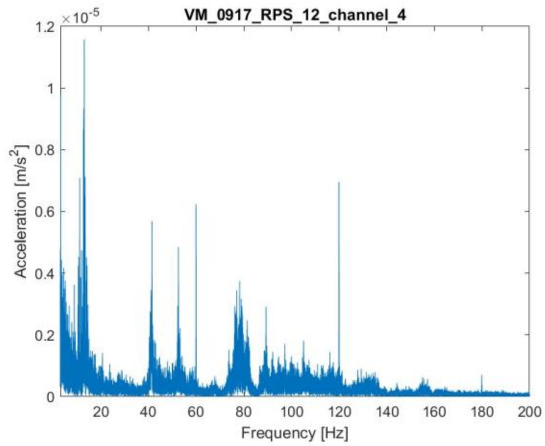

Figure 110 - FFT Signal at V_M=0.917 m/s and 12 RPS for Accelerometer No. 4 in the Global Arrangement

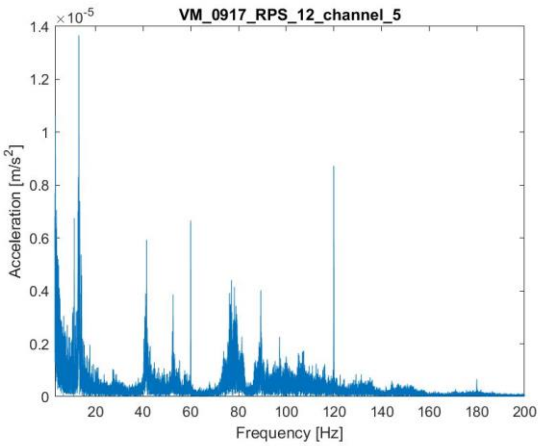

Figure 111 - FFT Signal at V_M=0.917 m/s and 12 RPS for Accelerometer No. 5 in the Global Arrangement

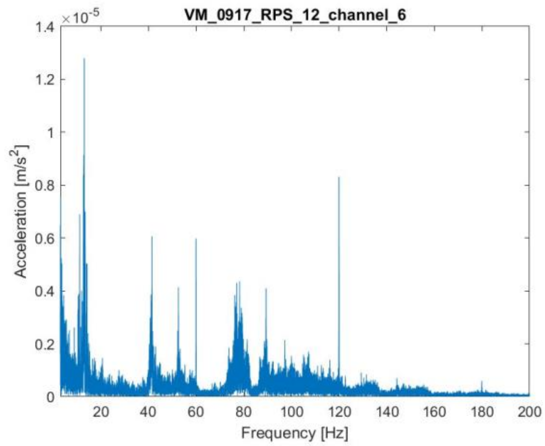

Figure 112 - FFT Signal at V_M=0.917 m/s and 12 RPS for Accelerometer No. 6 in the Global Arrangement

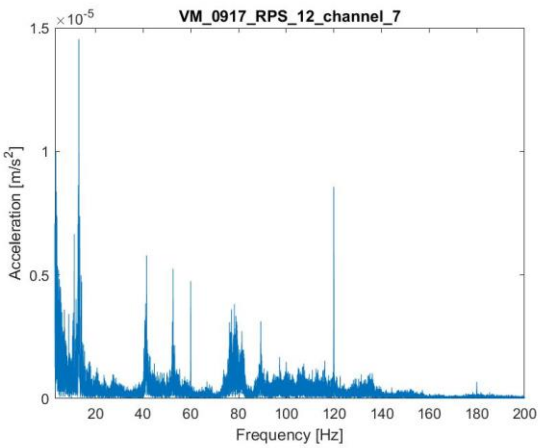

Figure 113 - FFT Signal at V_M=0.917 m/s and 12 RPS for Accelerometer No. 7 in the Global Arrangement

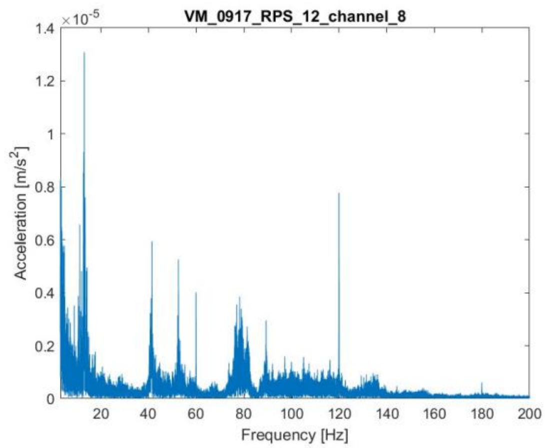

Figure 114 - FFT Signal at V_M=0.917 m/s and 12 RPS for Accelerometer No. 8 in the Global Arrangement

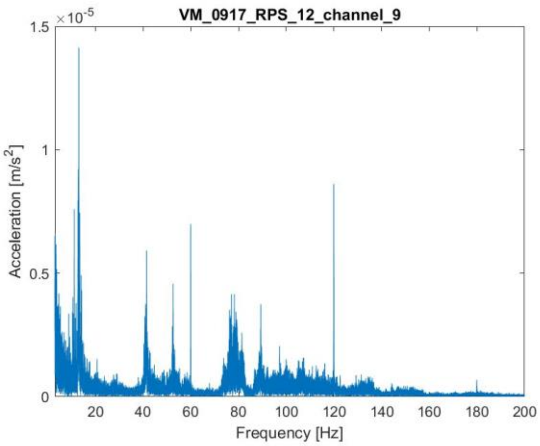

Figure 115 - FFT Signal at V_M=0.917 m/s and 12 RPS for Accelerometer No. 9 in the Global Arrangement

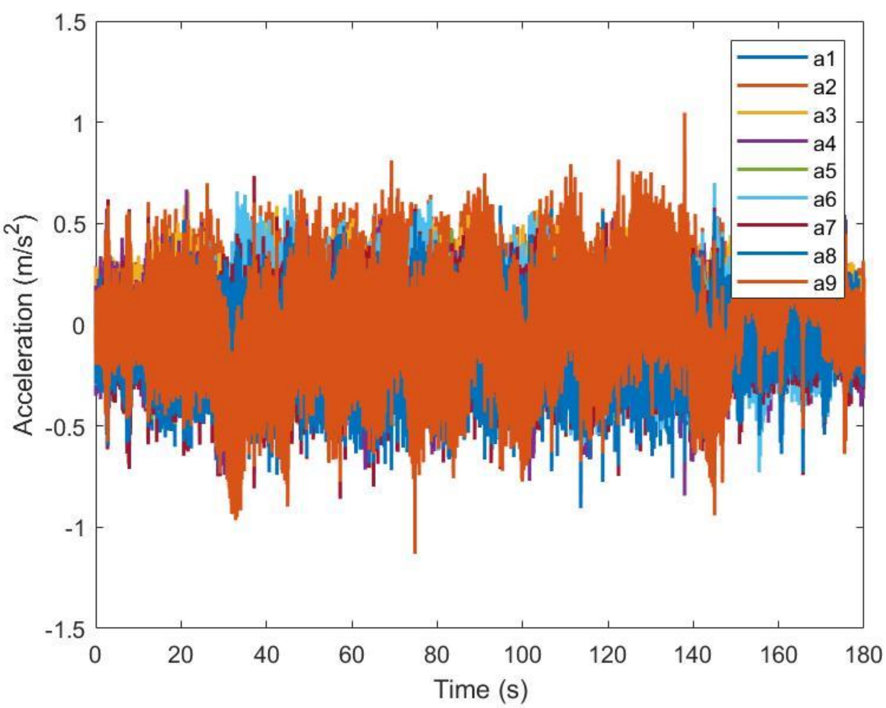

Figure 116 - Accelerometer Time Domain Signal for Global Arrangement at V_M=1.101 m/s and 6 RPS

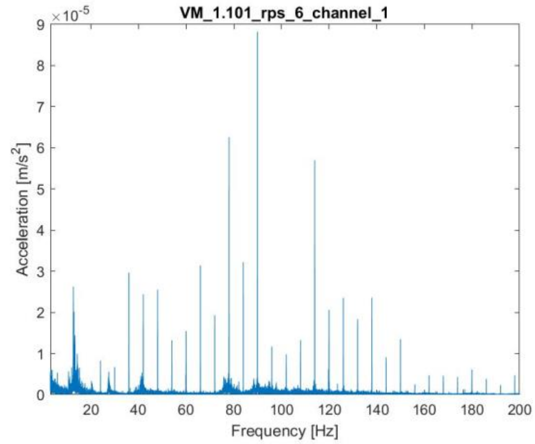

Figure 117 - FFT signal at V_M=1.101 m/s and 6 RPS for Accelerometer No. 1 in the Global Arrangement

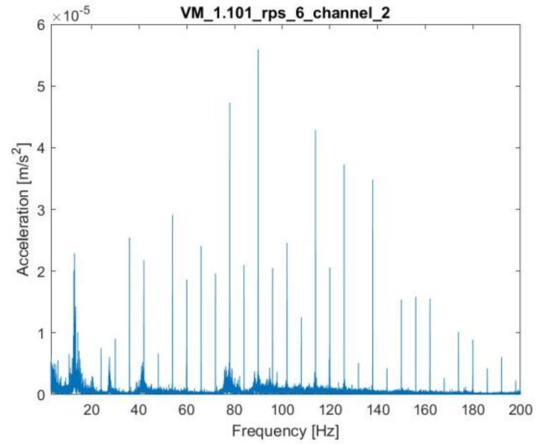

Figure 118 - FFT signal at V_M=1.101 m/s and 6 RPS for Accelerometer No. 2 in the Global Arrangement

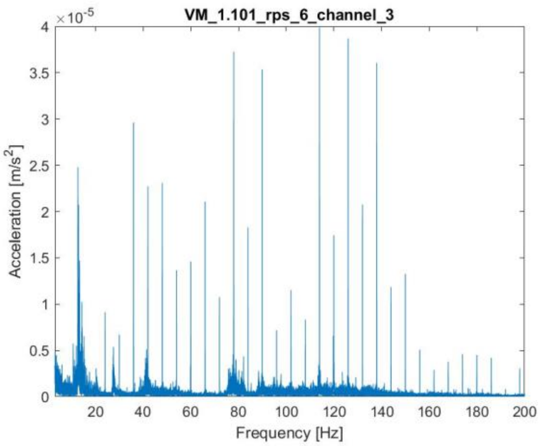

Figure 119 - FFT signal at V_M=1.101 m/s and 6 RPS for Accelerometer No. 3 in the Global Arrangement

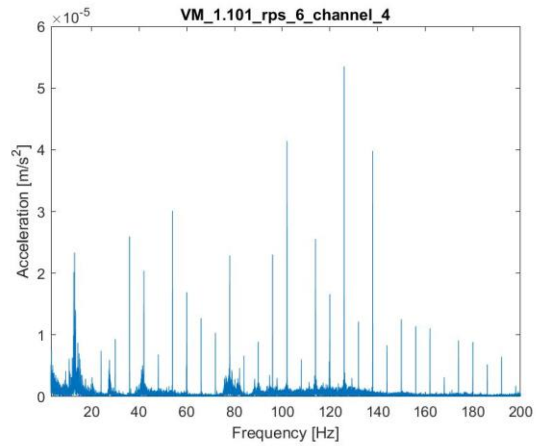

Figure 120 - FFT signal at V_M=1.101 m/s and 6 RPS for Accelerometer No. 4 in the Global Arrangement

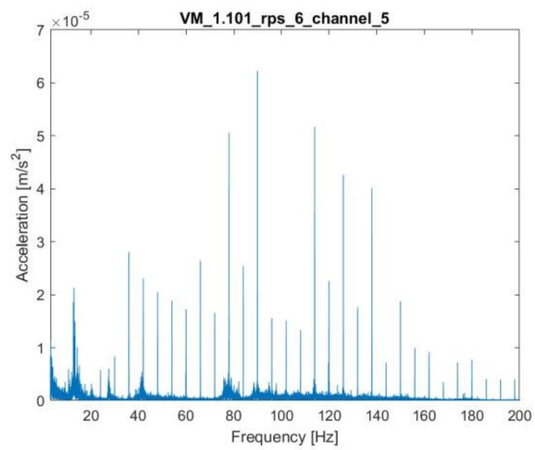

Figure 121 - FFT signal at V_M=1.101 m/s and 6 RPS for Accelerometer No. 5 in the Global Arrangement

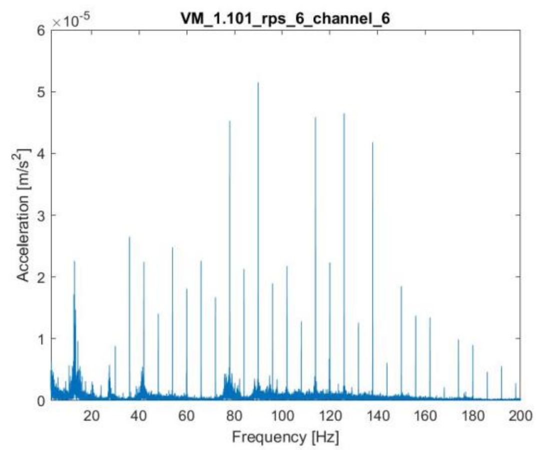

Figure 122 - FFT signal at V_M=1.101 m/s and 6 RPS for Accelerometer No. 6 in the Global Arrangement

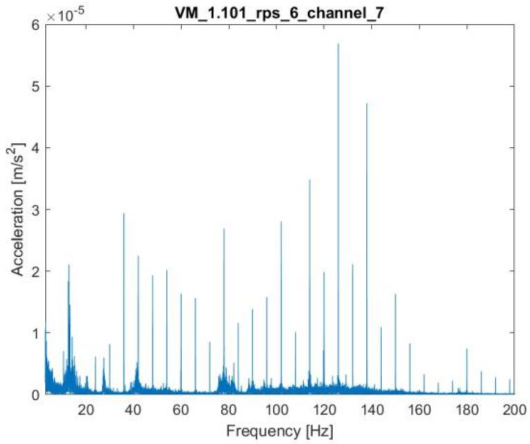

Figure 123 - FFT signal at V_M=1.101 m/s and 6 RPS for Accelerometer No. 7 in the Global Arrangement

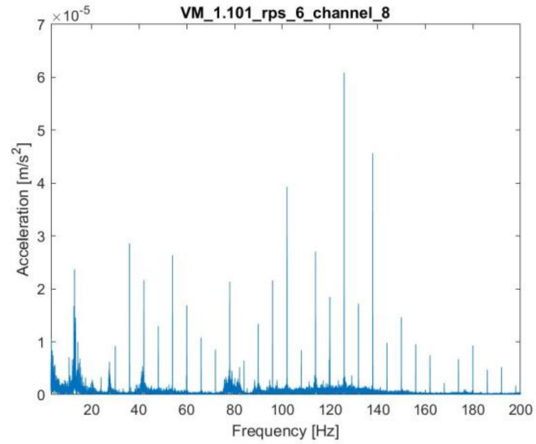

Figure 124 - FFT signal at V_M=1.101 m/s and 6 RPS for Accelerometer No. 8 in the Global Arrangement

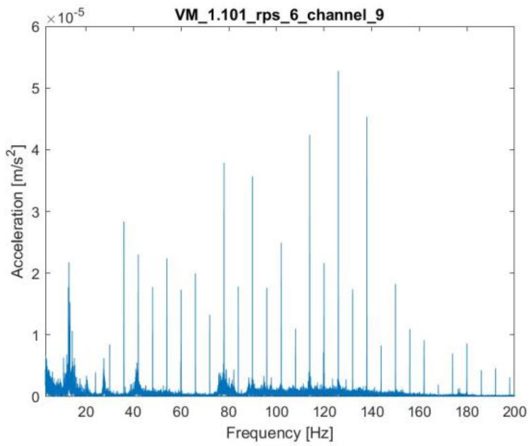

Figure 125 - FFT signal at V_M=1.101 m/s and 6 RPS for Accelerometer No. 9 in the Global Arrangement

Additional time domain signal for the Self-Propulsion tests in water with local accelerometer arrangement at 0.917 m/s and 4.45 rps is presented in Appendix B.1. (Figure 154). Figure 155 to Figure 163, in the same appendix, present the average FFT for the signal acquired by the accelerometers for the same signal.

Also, additional ABRAVIBE ODS analysis at blade passing frequencies for resistance, bollard and self-propulsion tests are presented in Appendix B.1. for the same (Figure 166 to Figure 182)

Lastly, Table 8**Error! Reference source not found.** summarizes the ODS at Blade Passing Frequencies for several run types and speeds. For each frequency listed, an ODS simulation in X, Y, Z and perspective views, were generated.

Table 8 – ODS at Blade Passing Frequencies

	Speed (RPS)	BPF	2nd BPF	3rd BPF	4th BPF	4th BPF	5th BPF	6th BPF	7th BPF	8th BPF	9th BPF	10th BPF	11th BPF
	4.45	17.8	35.6	53.4	71.2	89	106.8	124.6	142.4	160.2	178	195.8	213.6
	5.41	21.64	43.28	64.92	86.56	108.2	129.84	151.48	173.12	194.76	216.4	238.04	259.68
	6.26	25.04	50.08	75.12	100.16	125.2	150.24	175.28	200.32	225.36	250.4	275.44	300.48
	6.8	27.2	54.4	81.6	108.8	136	163.2	190.4	217.6	244.8	272	299.2	326.4
SP	0.917_12RPS	11.6	48	60.5	71.2	83.5	95	108.3	119.5	144.3			
SP	1.101_6RPS	13.8	27.2	48	66	78	90.3	113.5	126.8				
RES	VM 1.159	5	10	15	20	25	30	35	40	45	50	55	60
RES	VM 0.917	13.5	39.7	59.5	92.2	119.8							
RES	VM 1.101	13	42	59.5	88	119.8							

4.1.2.2 Hull Pressure Sensors Analysis

Below is the analysis of the pressure sensors installed in the hull area. For each type of run (Resistance, Bollard and Self-Propulsion), two speeds are analyzed, for which; an Average FFT plot and 6 peaks table is presented.

Figure 126 and Figure 127 presents the average FFT plot in a Resistance test for the signals acquired by the hull pressure sensors at speeds of 0.917 m/s and 1.101 m/s, respectively.

Table 9 and Table 10 show the first 6 peaks in each of the above FFT plots. Additional resistance tests' average FFT plots for other speeds are presented in Appendix B.2.1. (Figure 183 to Figure 185).

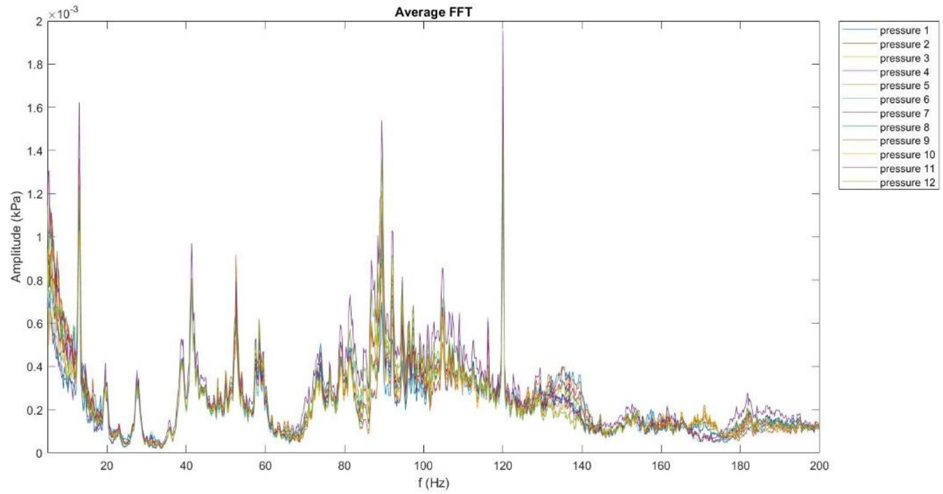

Figure 126 - Average FFT for Pressure Sensors for Resistance Test at V_M=0.917 m/s

Table 9 – Resistance Test Peaks at V_M=0.917 m/s

Peak 1 (Hz)	13
Peak 2 (Hz)	41
Peak 3 (Hz)	52
Peak 4 (Hz)	86
Peak 5 (Hz)	89
Peak 6 (Hz)	120

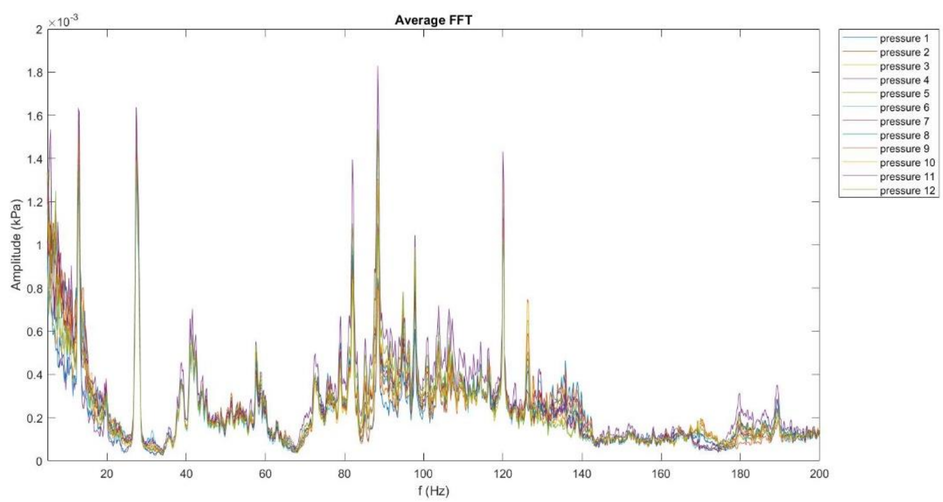

Figure 127 - Average FFT for Pressure Sensors for Resistance Test at V_M=1.101 m/s

Table 10 – Resistance Test Peaks at V_M=1.101 m/s

Peak 1 (Hz)	13
Peak 2 (Hz)	27
Peak 3 (Hz)	82
Peak 4 (Hz)	88
Peak 5 (Hz)	97
Peak 6 (Hz)	120

Figure 128 and Figure 129 presents the average FFT plot in a Bollard test for the signals acquired by the hull pressure sensors at propeller speeds of 4.45 RPS and 6.26 RPS, respectively. Table 11 and Table 12 show the first 6 peaks in each of the above FFT plots. Additional bollard tests' average FFT plots for other speeds are presented in Appendix B.2.2. (Figure 186 and Figure 187).

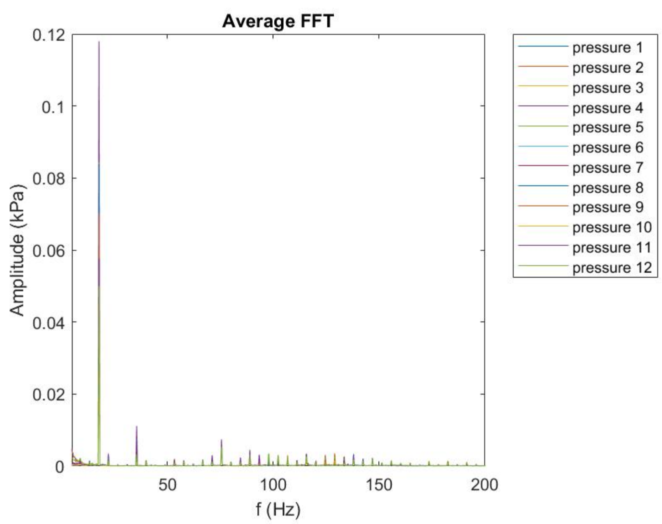

Figure 128 - Average FFT for Bollard Test at 4.45 RPS

Table 11 – Bollard Test Peaks for 4.45 RPS

Peak 1 (Hz)	17
Peak 2 (Hz)	22
Peak 3 (Hz)	35
Peak 4 (Hz)	75
Peak 5 (Hz)	89
Peak 6 (Hz)	115

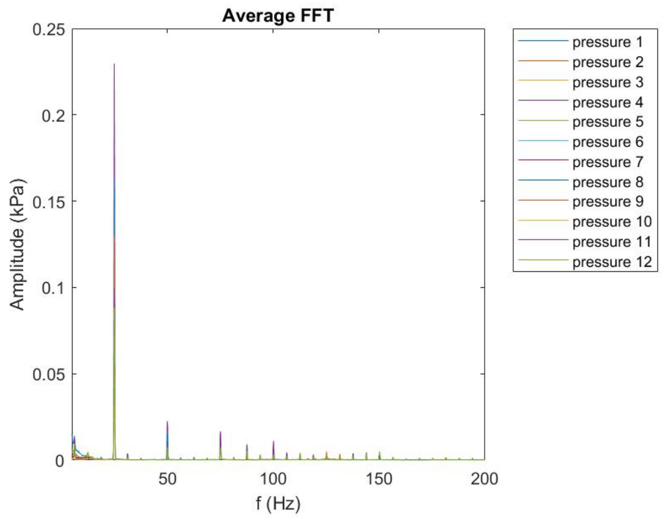

Figure 129 - Average FFT for Bollard Test at 6.26 RPS

Table 12 – Bollard Test Peaks for 6.26 RPS

Peak 1 (Hz)	6
Peak 2 (Hz)	25
Peak 3 (Hz)	50
Peak 4 (Hz)	75
Peak 5 (Hz)	87
Peak 6 (Hz)	100

Figure 130 and Figure 131 presents the average FFT plot in a Self-Propulsion test for the signals acquired by the hull pressure sensors at 0.917 m/s with propeller speed of 4.45 RPS and 1.101 m/s with propeller speed of 6.26 RPS, respectively. Table 13 and Table 14 note the first 6 peaks in each of the above FFT plots. Additional self-propulsion tests' average FFT plots for other speeds are presented in Appendix B.2.3. (Figure 188 to Figure 191).

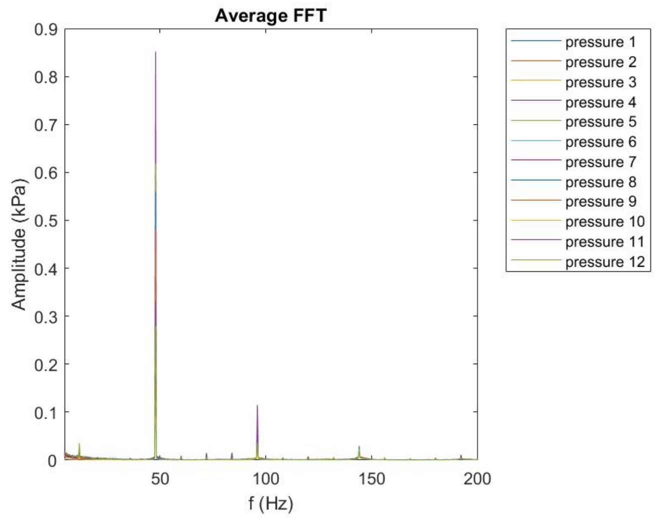

Figure 130 – Average FFT for the Self Propulsion Test at V_M=0.917 m/s and 12 RPS

Table 13 – Self-Propulsion Test Peaks for V_M=0.917 m/s and 12 RPS

Peak 1 (Hz)	12
Peak 2 (Hz)	48
Peak 3 (Hz)	72
Peak 4 (Hz)	84
Peak 5 (Hz)	96
Peak 6 (Hz)	144

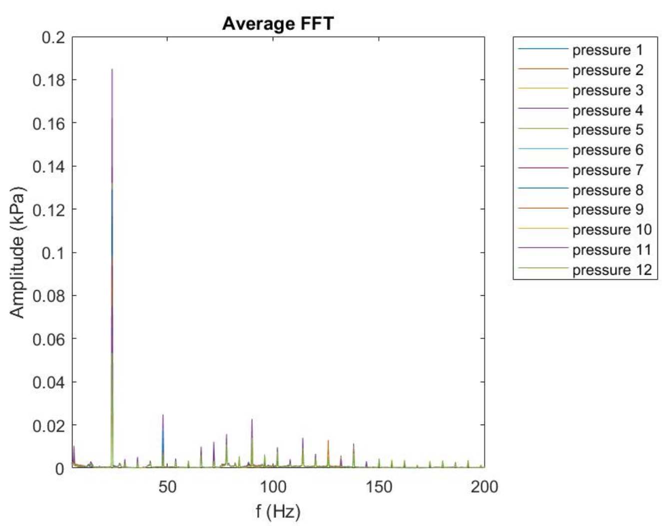

Figure 131 - Average FFT for the Self Propulsion Test at V_M=1.101 m/s and 6 RPS

Table 14 – Self-Propulsion Test Peaks at V_M=1.101 m/s and 6 RPS

Peak 1 (Hz)	6
Peak 2 (Hz)	24
Peak 3 (Hz)	48
Peak 4 (Hz)	66
Peak 5 (Hz)	72
Peak 6 (Hz)	78

Chapter 5: Discussion

As detailed in the previous sections, Experimental Modal Analysis (EMA) analysis/hammer impact testing was performed to understand the dynamics of the ship model and their influence on pressure sensors measurements.

As shown in Figure 15 and Figure 16, there are several peaks in the average FFT plot of the accelerometers; the first six peaks are noted in Table 5, with a noticeable peak amplitude at a frequency of 47 Hz. This test was performed at impact point A2 in the air, with a global arrangement of accelerometers. The following figures (Figure 17– Figure 25) captured the coherence for this impact. As impact point A2 (Figure 9) is closest to accelerometers no.1 and no.2, shown in Figure 10, a reliable coherence can be observed (≈1) in Figure 17 and Figure 18.

Alternatively, Table 6 shows us the peak of the same impact test, but in water conditions. The average FFT plot of the same test was presented in Figure 32 and Figure 33. Both Table 5 and Table 6 present the natural frequencies for the model in wet and dry conditions, respectively.

The analyses of the coherence of the FFTs obtained from the EMA show good results for the dry and wet conditions. As well, the modes are corresponding in both wet and dry conditions.

In addition, Operational Deflection Shape (ODS) analysis was performed on the same hammer-test impact measurements using a custom ABRAVIBE tool. Figure 26 to Figure 31 show us the natural modes of the ship model in the air, which coincides with the observed natural frequencies concluded earlier. The same applies to the results in water from Figure 43 to Figure 48.

To provide more conclusive results, the local accelerometer arrangement (refer to Figure 10) was also analyzed. Table 7 presents the natural frequencies that match the same frequencies from the water global arrangement tests. Figure 60 to Figure 65 offer more details into mode shapes of that area.

Moreover, measurements were taken during the resistance, bollard and self-propulsion tests. ODS analysis was also applied to these measurements using a different customized version of the ABRAVIBE tool. Given the results in the previous section and by calculating the passing band frequency for the model, the relative operational deflection shapes for those tests were concluded. Table 8 also shows a summary of the results noted.

In addition to the above, the pressure sensor measurements were recorded during the bollard, resistance, and self-propulsion tests. Despite the lack of a propeller in the resistance tests, they have helped to demonstrate and comprehend the background noise generated by the propeller when later installed and compared, as well as the hull hydrodynamics on the pressure measurements.

Figure 128 and Figure 129 show an example FFT from the data measured for two of the bollard tests, at a rotational speed of 4.45 rps and 6.26 rps. The peaks correspond to the fundamental frequencies of the propeller at rotational speeds mentioned in Table 8 of frequencies 17.8 Hz and 25.04 Hz, respectively, as well as their first harmonics (up to the first harmonics in the case of 6.26 rps).

Comparatively, Figure 130 and Figure 131 show the average FFTs calculated from the data obtained by the same pressure sensors during self-propulsion tests. The FFTs shown are for the tests conducted at 12 rps with 0.917 m/s advanced speed and 6rps with 1.101 m/s advanced speed. Again, the peaks correspond to the fundamental frequencies of the propeller at rotations speeds mentioned in Table 8 mentioned in Table 13 and Table 14 and their first harmonics.

Finally, Figure 126 and Figure 127 show two examples of the FFTs from the measured data for the resistance tests. The two examples shown are for resistance tests at 0.917 m/s and 1.101 m/s advanced speed of the model, respectively. Both plots give an idea of the background noise.

With the above mentioned, it can be concluded that the pressure sensors were properly installed and captured the propeller-induced pressure fluctuations at the hull area. Also, given the sharp peaks for the pressure measurements and that the first peak is the predominant peak, it demostrates that the propeller is not cavitating during tests. The resistance tests are showing peaks even though the propeller is not installed. Correlating to the results from the EMA and ODS, we can deduce that these peaks correspond to the natural frequencies of the hull model.

Nevertheless, the peaks recorded are generally 3 orders smaller than the peaks from the propeller pressures, and their influence on the measured data seems then negligible.

The ODS has confirmed the nature of the peaks found in the resistance tests. Though the modal shapes of the model are not always clear, especially at low frequencies, where a torsional mode seems to be predominant. The EMA properly identifies the natural frequencies and the natural modes of the model in dry conditions. In wet conditions, the coherence functions show that the model has not been excited enough at low frequencies, excluding the accelerometers adjacent to the impact hit.

Chapter 6: Future Work and Conclusion

6.1 Conclusion

This work presents an experimental procedure to evaluate the effect of the dynamic of ship model structures, while measuring propeller-induced hull pressure fluctuations during towing tank tests. The procedure is based on the combination of Experimental Modal Analysis (EMA), Operational Deflection Shape Analysis (ODS), and FFT analysis of pressures measured by using pressure sensors installed on the model stern. The results show the importance of performing these tests to avoid the effect of structural vibrations on the pressure measurements. In particular, including the ODS analysis while performing the hydrodynamic tests allow to monitor the ship model's dynamics and, therefore, understand if the latter is affecting the pressure pulses amplitudes measured. When this occurs, the results of the ODS and EMA can be used to calculate the contribution of the structural vibration on the pressure measurements, and decouple this from the propeller-induced hull pressure fluctuation.

6.2 Future Work

The results from this work have confirmed the effectiveness of ODS and EMA to understand the dynamics of the ship model structure while performing propeller-induced hull pressure pulses measurements; however, it also important to highlight the need for further studies. Related to this specific model and tests, further tests should be performed to understand the contribution of the electric motor to the dynamics of the model structures. The tests performed so far do not identify the contribution of the model motor to the overall vibration and hull pressure fluctuations.

Additional measurements by running the model with the motor in motion but without a propeller would help understand the motor excitation of the ship model. In addition, the modal analysis was performed using single-axis accelerometers which reduces the capability of the analysis to reproduce tridimensional modes. To better represent the torsional modes, these tests should be performed by using tri-axial accelerometers.

This work paves the way to the development of FE and CFD models that will help understand the effect of propeller design parameters on the induced vibration on the ship hull. Indeed, these experimental outcomes will be used in the PINOV project to validate FE and CFD models that will investigate different propellers designs.

Bibliography

American Bureau of Shipping. (2016). *Guide For Crew Habitability On Ships* (Issue February).

American Bureau of Shipping (ABS). (2006a). Guidance Notes on Ship Vibration. *Abs*, *2006*(April), 1–96.

American Bureau of Shipping (ABS). (2006b). Guidance Notes on Ship Vibration. *Abs*, *2006*(April), 1–96. https://ww2.eagle.org/content/dam/eagle/rules-and-guides/current/conventional_ocean_service/147_shipvibration/Ship_Vibration_GN_e-Jan15.pdf

American Bureau of Shipping (ABS). (2014a). ABS Guidance Notes on Noise and Vibration Control for Inhabited Spaces. *American Bureau of Shipping*, *July*.

American Bureau of Shipping (ABS). (2014b). Guide for Passenger Comfort on Ships. *American Bureau of Shipping*, *2001*(February).

Asmussen, I., Menzel, W., & Mumm, H. (2001). *Ship Vibration*. Germanischer Lloyd.

Biot, M., Boote, D., Brocco, E., Moro, L., Pais, T., & Delle Piane, S. (2015). Numerical and Experimental Analysis of the Dynamic Behavior of Main Engine Foundations. In *The Twenty-fifth International Ocean and Polar Engineering Conference* (p. 6). International Society of Offshore and Polar Engineers.

Biot, M., & Moro, L. (2012). Experimental Study of a Resilient Mounting for Marine Diesel Engines. *In Proceedings of the IMDC 2012 Conference, April*.

Constantinescu, A., Nême, A., & Rigo, P. (2009). Vibration assessment of ship structures. *Proceedings of the International Offshore and Polar Engineering Conference*, 720–726.

Dessi, D., Faiella, E., & Riccioli, F. (2021). A Procedure for the Identification of Hydrodynamic Damping Associated to Elastic Modes. *Lecture Notes in Civil Engineering*, *64 LNCE*, 305–

320. https://doi.org/10.1007/978-981-15-4672-3_19

Erbe, C., Marley, S. A., Schoeman, R. P., Smith, J. N., Trigg, L. E., & Embling, C. B. (2019). The Effects of Ship Noise on Marine Mammals—A Review. *Frontiers in Marine Science*, *6*, 606. https://doi.org/10.3389/fmars.2019.00606

Fragasso, J., Moro, L., Mendoza Vassallo, P. N., Biot, M., & Badino, A. (2017). Experimental characterization of viscoelastic materials for marine applications. *Progress in the Analysis and Design of Marine Structures - Proceedings of the 6th International Conference on Marine Structures, MARSTRUCT 2017*, 87–96. https://doi.org/10.1201/9781315157368-12

International Organization for Standardization (ISO). (2000). *ISO 6954:2000 Mechanical Vibration and Shock – Guidelines for the Measurement, Reporting and Evaluation of Vibration with Regard to Habitability on Passenger and Merchant Ships*. ISO.

Jensen, A., & Jepsen, J. R. (2014). Vibration on board and health effects. *International Maritime Health*, *65*(2), 58–60. https://doi.org/10.5603/IMH.2014.0013

Kingma, I., Delleman, N. J., & Van Dieën, J. H. (2003). The effect of ship accelerations on three-dimensional low back loading during lifting and pulling activities. *International Journal of Industrial Ergonomics*, *32*(1), 51–63. https://doi.org/10.1016/S0169-8141(03)00029-5

Lloyd's Register. (2006). *Ship Vibration and Noise*. *July*.

Mariani, R., & Dessi, D. (2012). Analysis of the global bending modes of a floating structure using the proper orthogonal decomposition. *Journal of Fluids and Structures*, *28*, 115–134. https://doi.org/10.1016/J.JFLUIDSTRUCTS.2011.11.009

Moro, L, Brocco, E., Vassallo, P. N. M., Biot, M., Liang, P., Hong, M., Wang, Z., Iglesias, A. M., Wicks, A. L., Burdisso, R. a, Mitchell, L. D., Biot, M., Lorenzo, F., Mcgoldrick, R. T., & Trench, W. F. (2015). Student Solutions Manual for Elementary Differential Equations and

Elementary Differential Equations with Boundary Value Problems ELEMENTARY ELEMENTARY DIFFERENTIAL EQUATIONS WITH BOUNDARY VALUE. *Journal of Marine Science and Application*, *14*(3), 234–243. https://doi.org/10.1007/s11804-015-1310-1

Moro, Lorenzo, Brocco, E., Badino, A., Vassallo, P. N. M., Clericuzio, A., & Biot, M. (2016). Design procedure for the development of new floating floors to improve comfort on ships. *PRADS 2016 - Proceedings of the 13th International Symposium on PRActical Design of Ships and Other Floating Structures*.

Norwood, M. N., & Dow, R. S. (2013). Dynamic analysis of ship structures. *Ships and Offshore Structures*, *8*(3–4), 270–288. https://doi.org/10.1080/17445302.2012.755285

Ojak, W. (1988). Vibrations and Waterborne Noise on Fishery Vessels. *Journal of Ship Research*, *32*(2), 112–133.

Pais, T., Moro, L., Boote, D., & Biot, M. (2017). Vibration analysis for the comfort assessment of superyachts. *Journal of Marine Science and Application*, *16*(3), 323–333. https://doi.org/10.1007/s11804-017-1420-z

Pepper, C. B., Nascarella, M. A., & Kendall, R. J. (2003). A review of the effects of aircraft noise on wildlife and humans, current control mechanisms, and the need for further study. *Environmental Management*, *32*(4), 418–432. https://doi.org/10.1007/s00267-003-3024-4

Rao, S. S. (2007). Vibration of Continuous Systems. In *Vibration of Continuous Systems*. https://doi.org/10.1002/9780470117866

Ship Structure Committee. (1990). *Practical Guide for Shipboard Vibration Control and Attenuation*.

Smolko, A. (2009). *Structural response of the ship hull elements subject to excitation generated* *by the main engine*. *February 2013*.

Steen, S. (2015). *Experimental methods in marine hydrodynamics: statistical analysis*. *August*. http://astorplast.no/wp-content/uploads/AppendixStatisticalAnalysis.pdf

Subashi, G. H. M. J., Matsumoto, Y., & Griffin, M. J. (2008). Modelling resonances of the standing body exposed to vertical whole-body vibration: Effects of posture. *Journal of Sound and Vibration*, *317*(1–2), 400–418. https://doi.org/10.1016/j.jsv.2008.03.019

The International Towing Tank Conference (ITTC). (1966). *Proceedings of the 11th ITTC Conference*.

The International Towing Tank Conference (ITTC). (2011a). ITTC - Recommended Procedures and Guidelines - Resistance Test (7.5-02-02-01). *International Towing Tank Conference*, 13. ittc.info/media/1217/75-02-02-01.pdf

The International Towing Tank Conference (ITTC). (2011b). ITTC – Recommended Procedures and Guidelines Scale, Model Test, Cavitation Fluctua-, Cavitation Induced Pressure. *ITTC – Recommended Procedures and Guidelines, 7.5 – 02-03-03.3*, 16.

The International Towing Tank Conference (ITTC). (2014). *ITTC – Recommended Procedures and Guidelines ITTC – Recommended Procedures and Guidelines Definition of Variables*. 1–10.

The International Towing Tank Conference (ITTC). (2017). Propulsion/Bollard Pull Test - 7.5-02-03-01.1. *28th International Towing Tank Conference, Wuxi, China, September 17-22*, 1–17.

United Nations Conference on Trade and Development (UNCTAD). (2019). *UNCTAD Handbook of Statistics 2019*. United Nations. https://www.un-ilibrary.org/content/books/9789210039673

Vergassola, G., Boote, D., & Tonelli, A. (2018). On the damping loss factor of viscoelastic materials for naval applications. *Ships and Offshore Structures*, *13*(5), 466–475. https://doi.org/10.1080/17445302.2018.1425338

Wijngaarden, E. Van. (2005). *Recent Developments in Predicting Propeller-Induced Hull Pressure Pulses*. 1–8.

Wijngaarden, E. Van. (2011). *Prediction of Propeller-Induced Hull-Pressure Fluctuations Proefschrift* (Issue November). Technische Universiteit Delft.

Wijngaarden, E. Van, Brouwer, J., & Zijlstra, M. (2006). A spatial extrapolation technique for sparse measurements of propeller-induced hull-pressures using an inverse acoustic boundary element method. *6th International Symposium on Cavitation, September*.

Zambon, A., Moro, L., & Biot, M. (2021). Vibration analysis of super-yachts: Validation of the Holden Method and estimation of the structural damping. *Marine Structures*, *75*. https://doi.org/10.1016/j.marstruc.2020.102802

Appendix A: Hammer Test

Appendix A.1. Hammer Test in Air

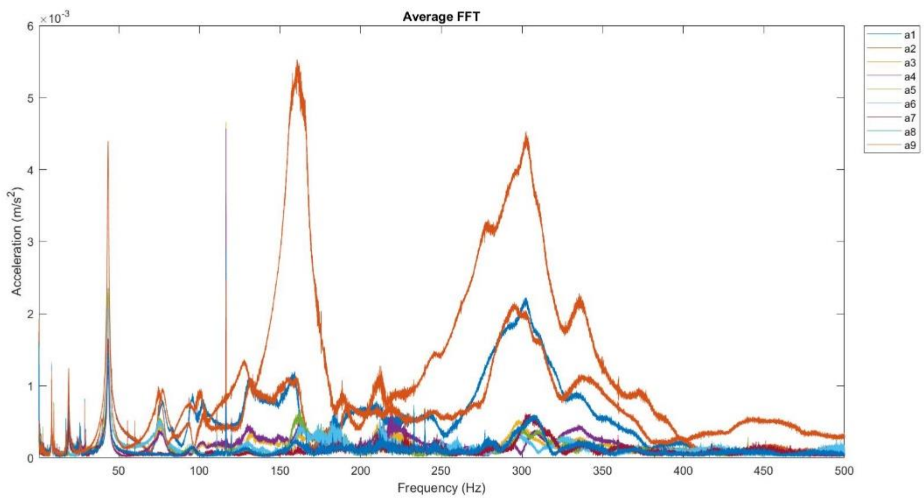

Figure 132 - Average FFT for Accelerometers' Global Arrangement in Air at Impact Point A2

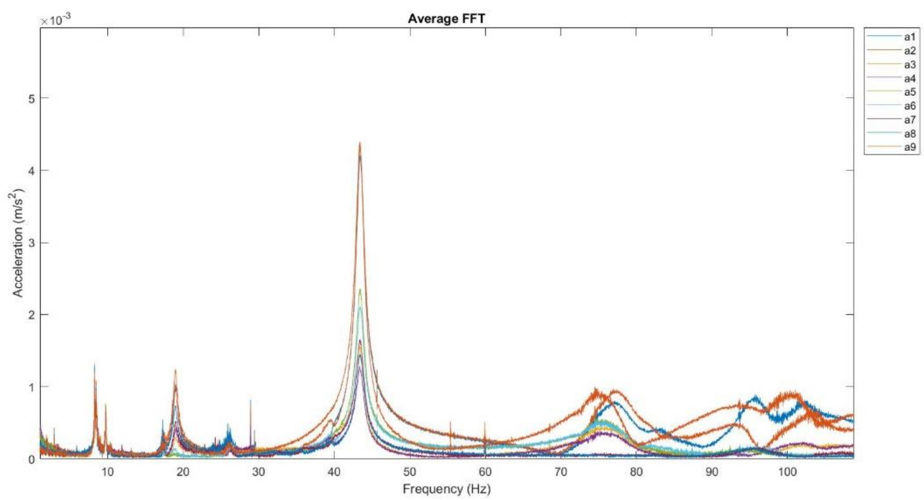

Figure 133 – Average FFT for Accelerometers' Global Arrangement in Air Up to 100 Hz at Impact Point A2

First six peaks:

Peak 1 (Hz)	8
Peak 2 (Hz)	18
Peak 3 (Hz)	43
Peak 4 (Hz)	74
Peak 5 (Hz)	161
Peak 6 (Hz)	303

Table 15 -Hammer Test in Air Peaks

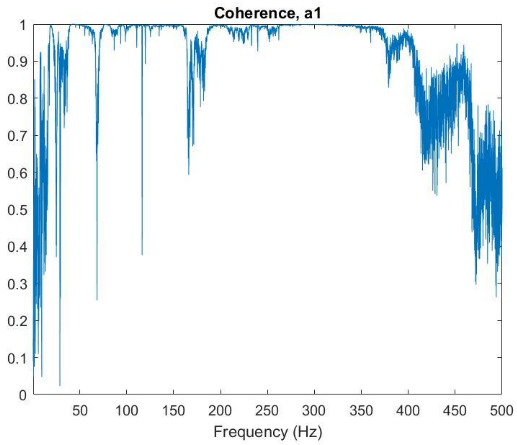

Figure 134 - Coherence Level for Accelerometer No. 1 for Global Arrangement in Air

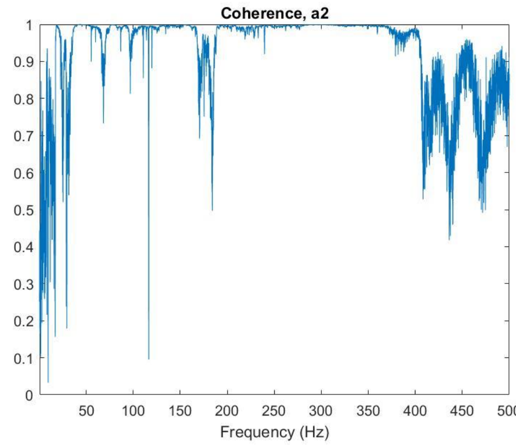

Figure 135 - Coherence Level for Accelerometer No. 2 for Global Arrangement in Air

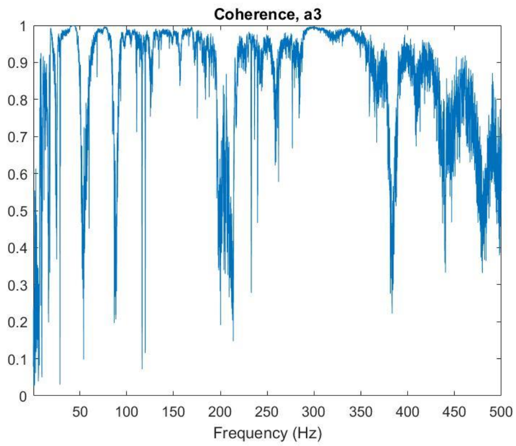

Figure 136 - Coherence Level for Accelerometer No. 3 for Global Arrangement in Air

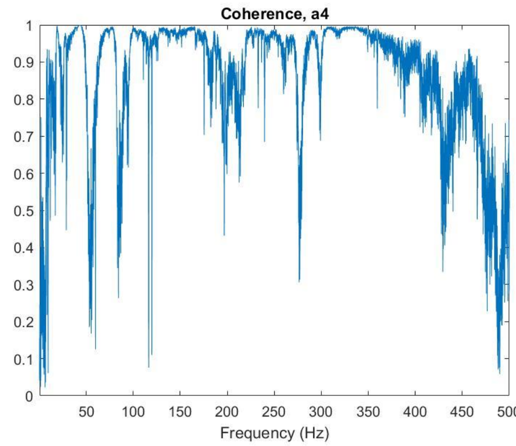

Figure 137 - Coherence Level for Accelerometer No. 4 for Global Arrangement in Air

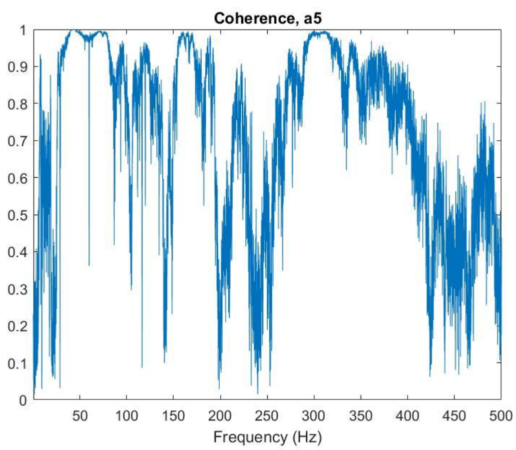

Figure 138 - Coherence Level for Accelerometer No. 5 for Global Arrangement in Air

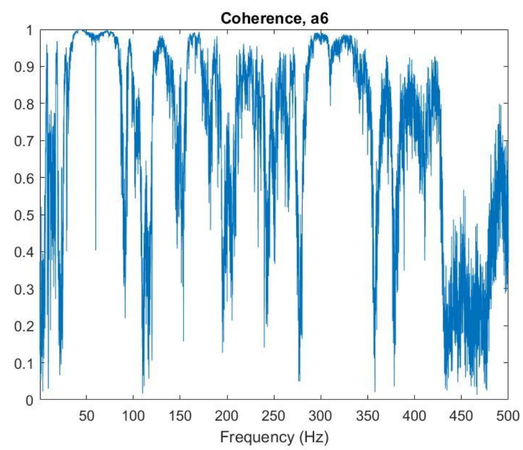

Figure 139 - Coherence Level for Accelerometer No. 6 for Global Arrangement in Air

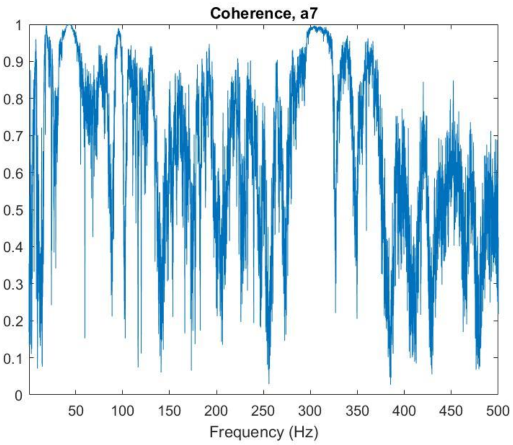

Figure 140 - Coherence Level for Accelerometer No. 7 for Global Arrangement in Air

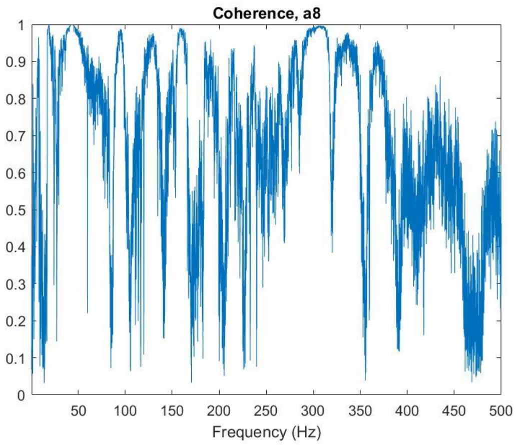

Figure 141 - Coherence Level for Accelerometer No. 8 for Global Arrangement in Air

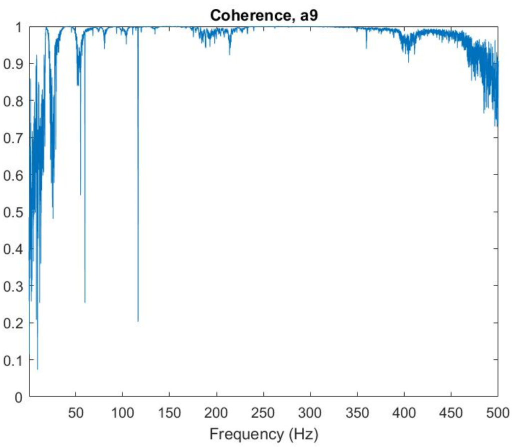

Figure 142 - Coherence Level for Accelerometer No. 9 for Global Arrangement in Air

Appendix A.2. Hammer Test in Water

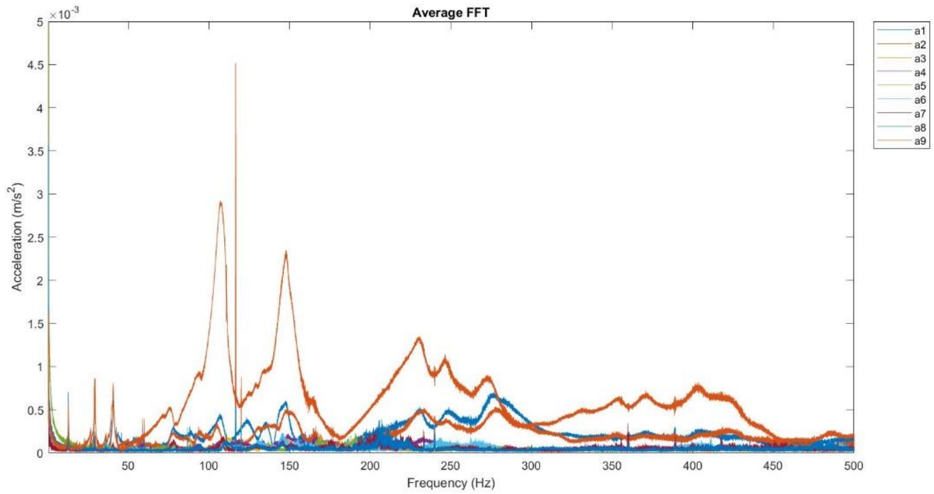

Figure 143 - Average FFT for Accelerometers' Global Arrangement in Water at Impact Point A2

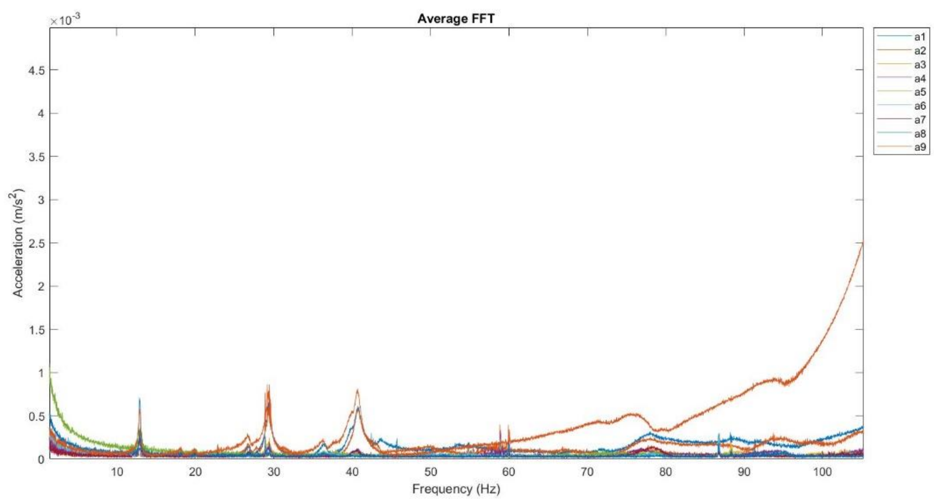

Figure 144 - Average FFT for Accelerometers' Global Arrangement in Water Up to 100 Hz at Impact Point A2

First six peaks:

Peak 1 (Hz)	12
Peak 2 (Hz)	29
Peak 3 (Hz)	40
Peak 4 (Hz)	106
Peak 5 (Hz)	147
Peak 6 (Hz)	230

Table 16 - Hammer Test in Water Peaks

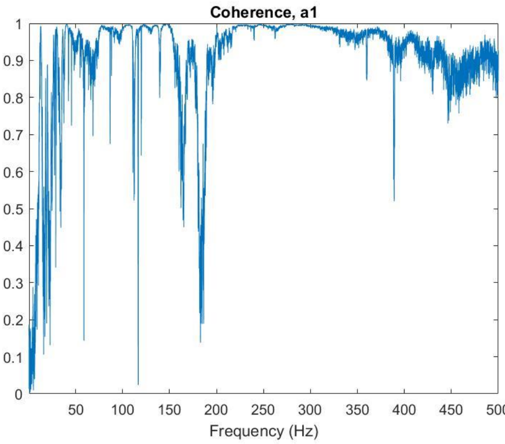

Figure 145 - Coherence Level for Accelerometer No. 1 for Global Arrangement in Water

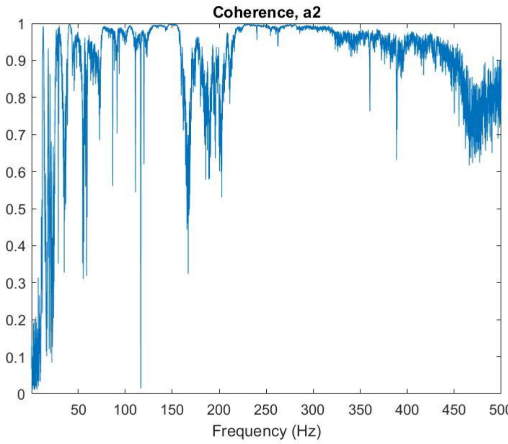

Figure 146 - Coherence Level for Accelerometer No. 2 for Global Arrangement in Water

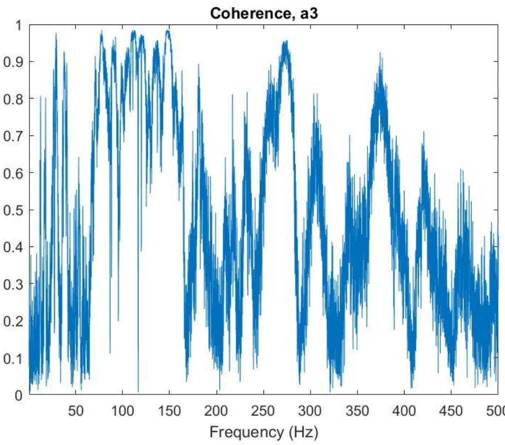

Figure 147 - Coherence Level for Accelerometer No. 3 for Global Arrangement in Water

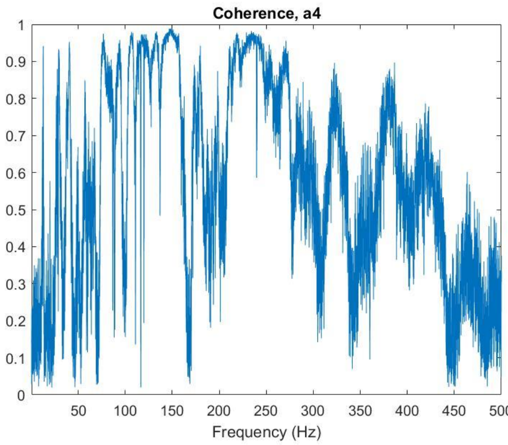

Figure 148 - Coherence Level for Accelerometer No. 4 for Global Arrangement in Water

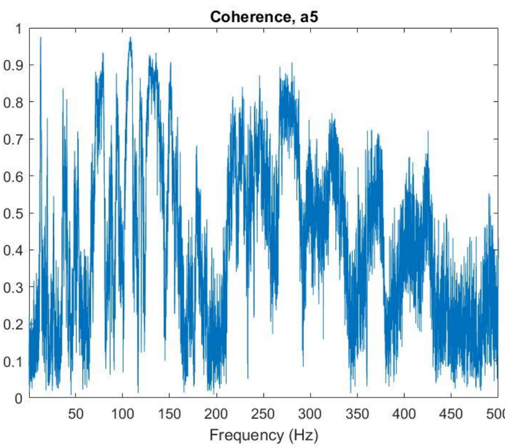

Figure 149 - Coherence Level for Accelerometer No. 5 for Global Arrangement in Water

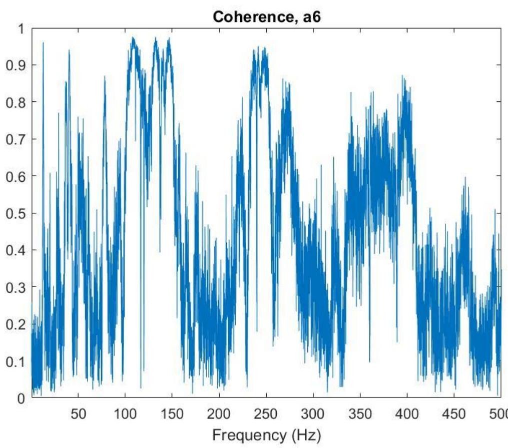

Figure 150 - Coherence Level for Accelerometer No. 6 for Global Arrangement in Water

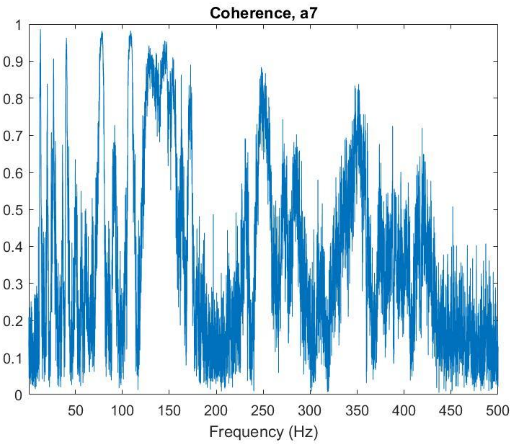

Figure 151 - Coherence Level for Accelerometer No. 7 for Global Arrangement in Water

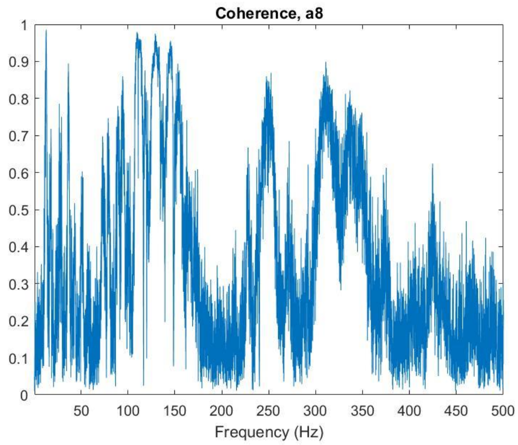

Figure 152 - Coherence Level for Accelerometer No. 8 for Global Arrangement in Water

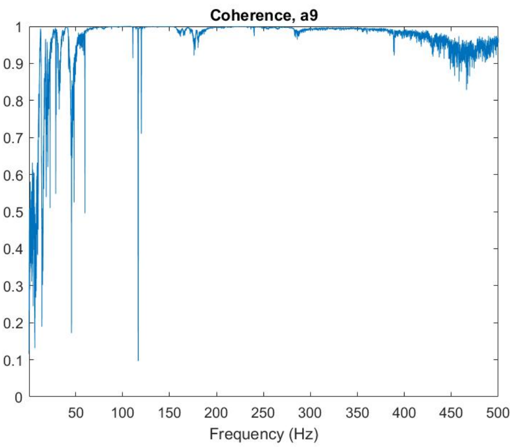

Figure 153 - Coherence Level for Accelerometer No. 9 for Global Arrangement in Water

Appendix B: Hydrodynamic Tests

Appendix B.1. ODS Measurements

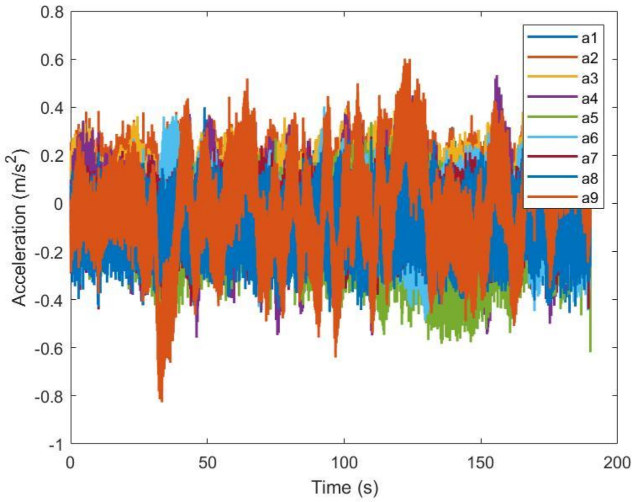

Figure 154 – Accelerometer Time Domain Signal for Local Arrangement at VM=0.917 m/s and 4.45 RPS

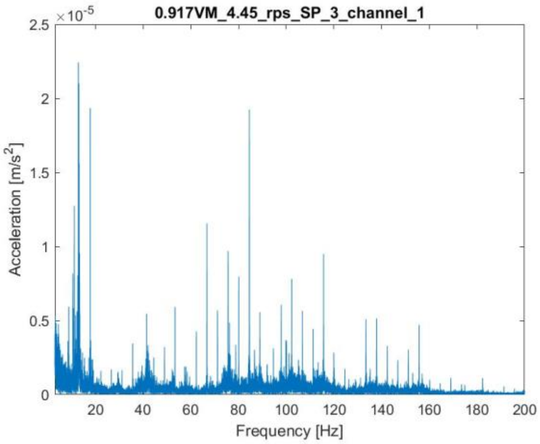

Figure 155 - FFT Signal at VM=0.917 m/s and 4.45 RPS for Accelerometer No. 1 in the Local Arrangement

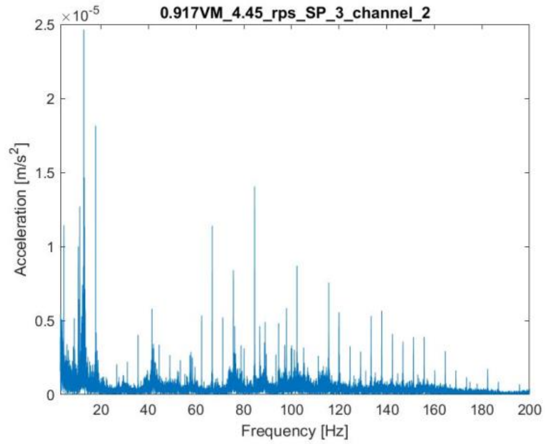

Figure 156 - FFT Signal at VM=0.917 m/s and 4.45 RPS for Accelerometer No. 2 in the Local Arrangement

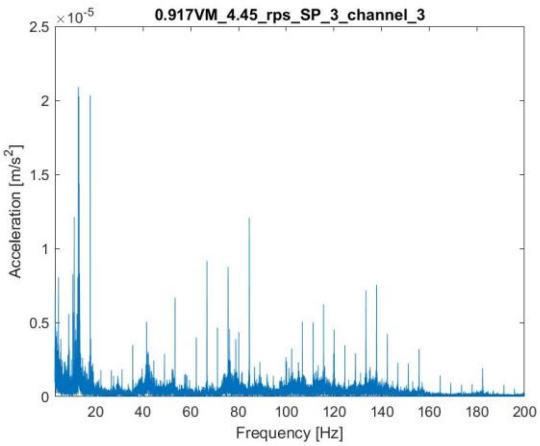

Figure 157 - FFT Signal at VM=0.917 m/s and 4.45 RPS for Accelerometer No. 3 in the Local Arrangement

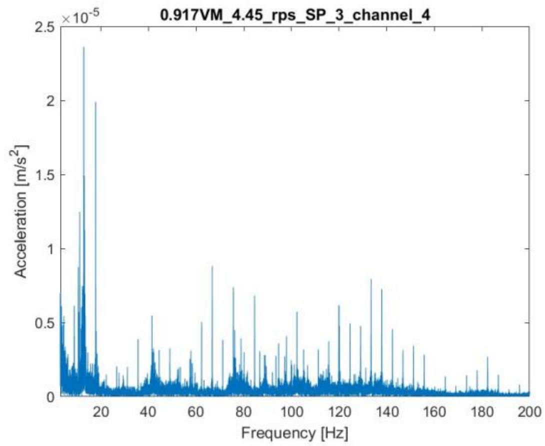

Figure 158 - FFT Signal at VM=0.917 m/s and 4.45 RPS for Accelerometer No. 4 in the Local Arrangement

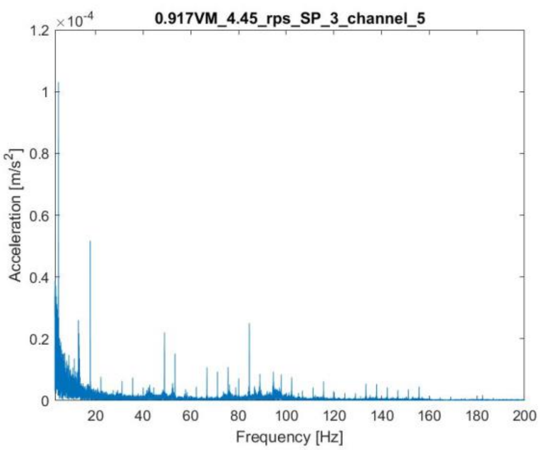

Figure 159 - FFT Signal at VM=0.917 m/s and 4.45 RPS for Accelerometer No. 5 in the Local Arrangement

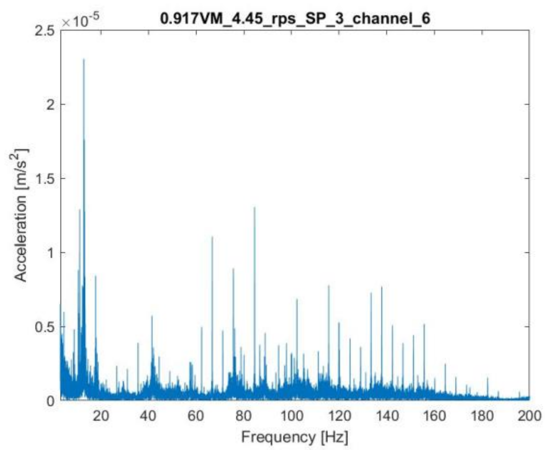

Figure 160 -FFT Signal at VM=0.917 m/s and 4.45 RPS for Accelerometer No. 6 in the Local Arrangement

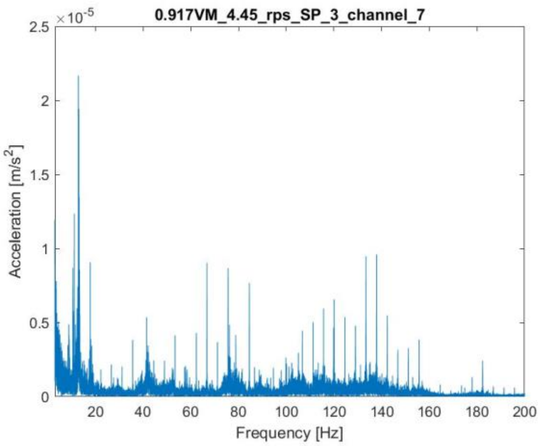

Figure 161 - FFT Signal at VM=0.917 m/s and 4.45 RPS for Accelerometer No. 7 in the Local Arrangement

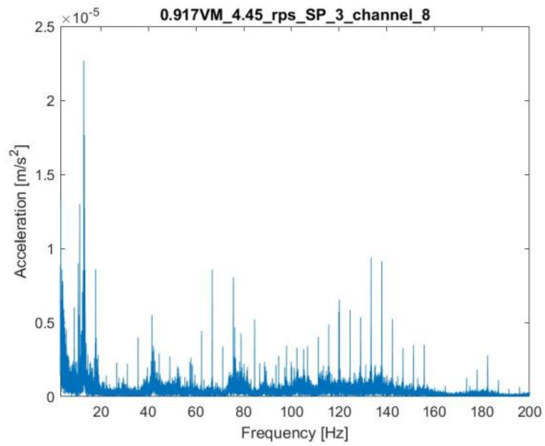

Figure 162 - FFT Signal at VM=0.917 m/s and 4.45 RPS for Accelerometer No. 8 in the Local Arrangement

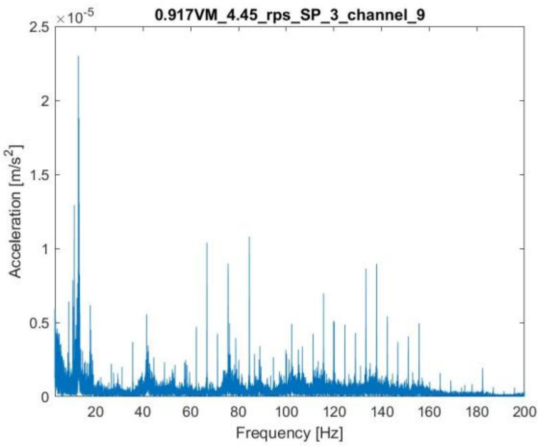

Figure 163 -FFT Signal at VM=0.917 m/s and 4.45 RPS for Accelerometer No. 9 in the Local Arrangement

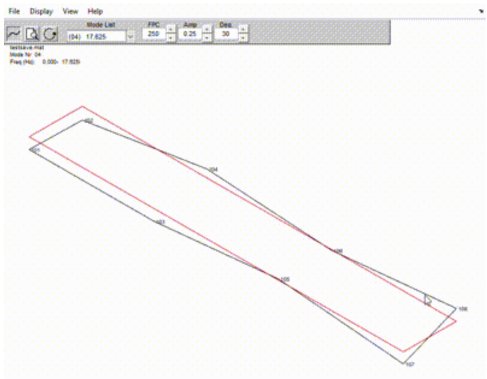

Figure 164 - ODS at Blade Passing Frequencies for a Bollard test at 4.45 RPS with frequency of 17.8 Hz

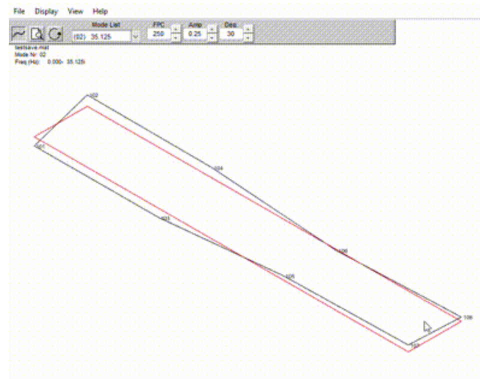

Figure 165 - ODS at Blade Passing Frequencies for a Bollard test at 4.45 RPS with frequency of 35.6 Hz

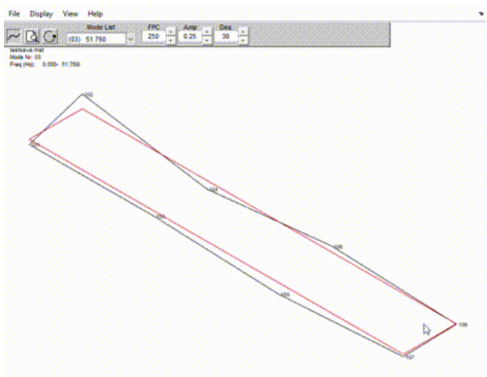

Figure 166 - ODS at Blade Passing Frequencies for a Bollard test at 4.45 RPS with frequency of 53.4 Hz

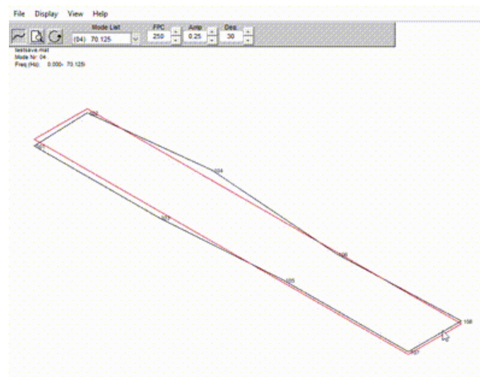

Figure 167- ODS at Blade Passing Frequencies for a Bollard test at 4.45 RPS with frequency of 71.2 Hz

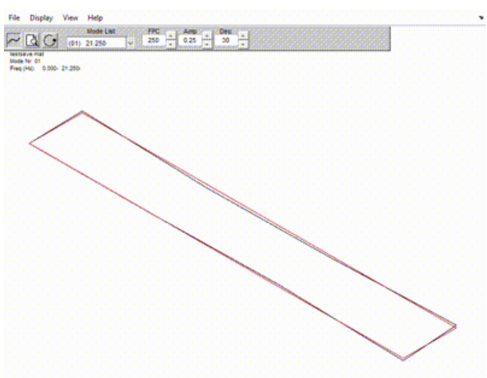

Figure 168 - ODS at Blade Passing Frequencies for a Bollard test at 5.41 RPS with frequency of 21.64 Hz

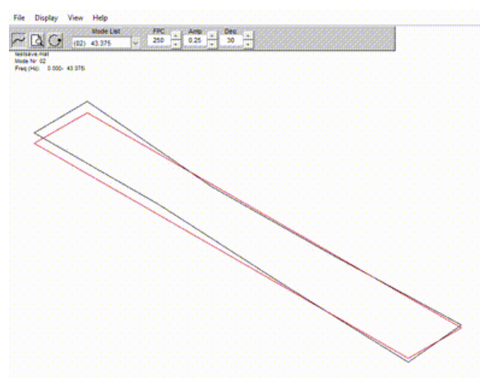

Figure 169 - ODS at Blade Passing Frequencies for Bollard tests at 5.41 RPS with frequency of 43.28 Hz

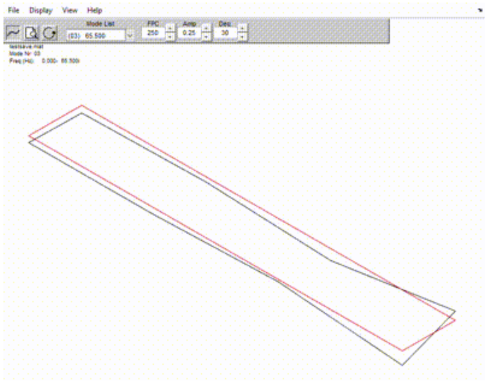

Figure 170 - ODS at Blade Passing Frequencies for Bollard tests at 5.41 RPS with frequency of 64.92 Hz

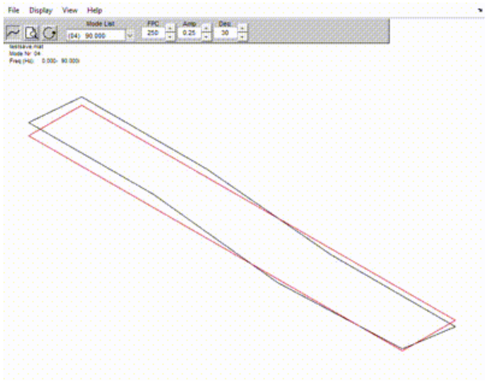

Figure 171 - ODS at Blade Passing Frequencies for Bollard tests at 5.41 RPS with frequency of 85.56 Hz

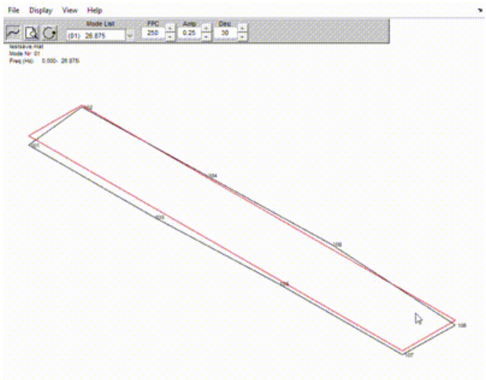

Figure 172 - ODS at Blade Passing Frequencies for Bollard tests at 6.8 RPS with frequency of 27.2 Hz

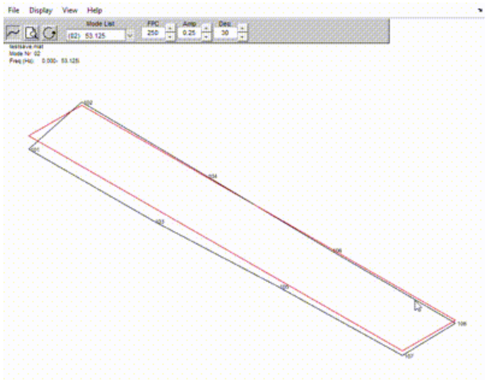

Figure 173 - ODS at Blade Passing Frequencies for Bollard tests at 6.8 RPS with frequency of 54.4 Hz

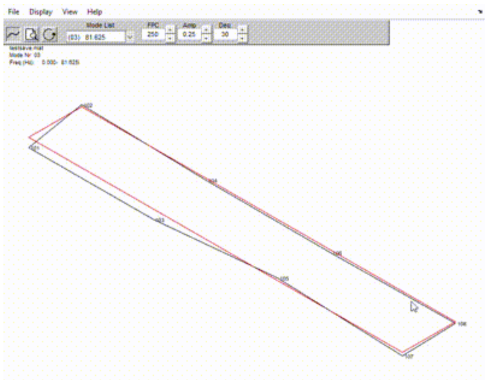

Figure 174 - ODS at Blade Passing Frequencies for Bollard tests at 6.8 RPS with frequency of 81.6 Hz

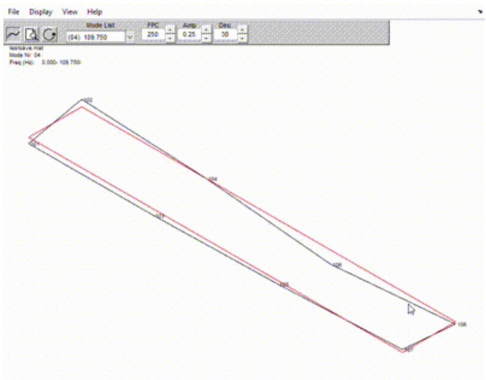

Figure 175 - ODS at Blade Passing Frequencies for Bollard tests at 6.8 RPS with frequency of 108.8 Hz

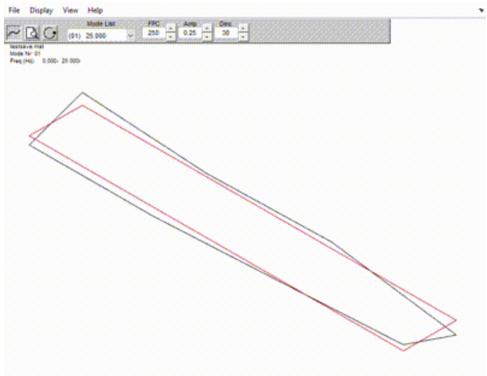

Figure 176 - ODS at Blade Passing Frequencies for Bollard tests at 6.26 RPS with frequency of 25.04 Hz

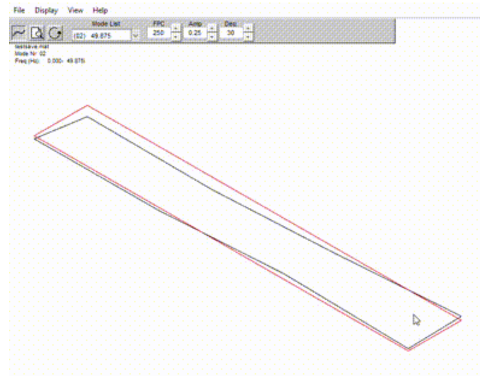

Figure 177 - ODS at Blade Passing Frequencies for Bollard tests at 6.26 RPS with frequency of 50.08 Hz

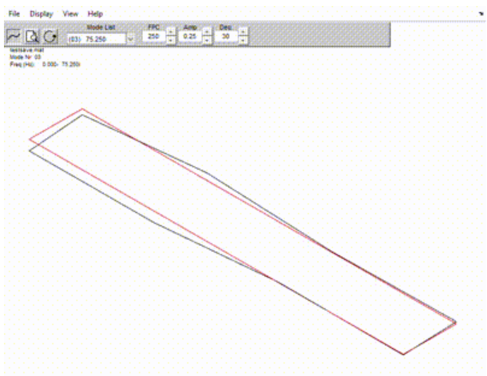

Figure 178 - ODS at Blade Passing Frequencies for Bollard tests at 6.26 RPS with frequency of 75.12 Hz

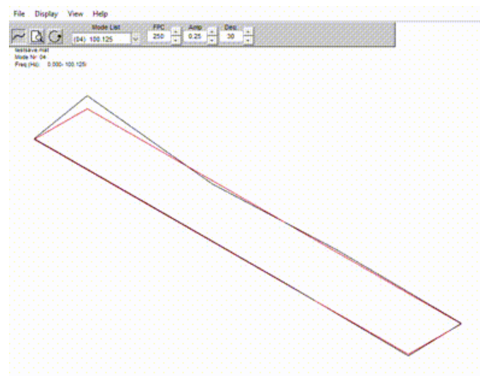

Figure 179 - ODS at Blade Passing Frequencies for Bollard tests at 6.26 RPS with frequency of 100.16 Hz

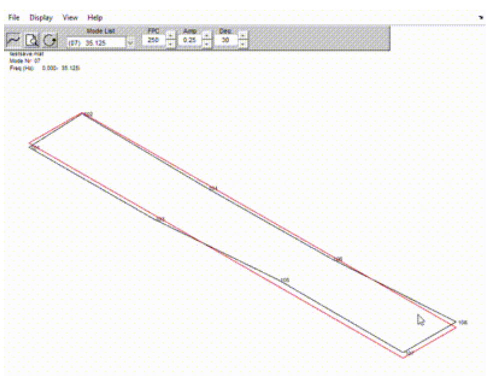

Figure 180 - ODS at Blade Passing Frequencies for Resistance tests at advanced speed of 1.159 m/s with frequency of 35 Hz

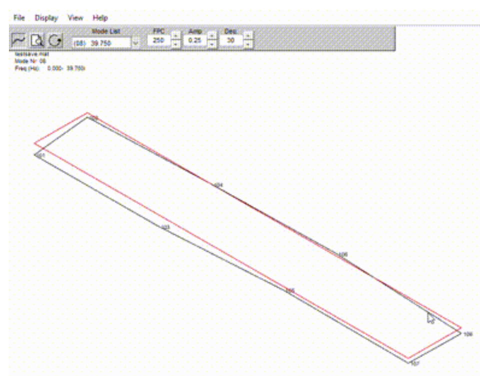

Figure 181 - ODS at Blade Passing Frequencies for Resistance tests at advanced speed of 1.159 m/s with frequency of 40 Hz

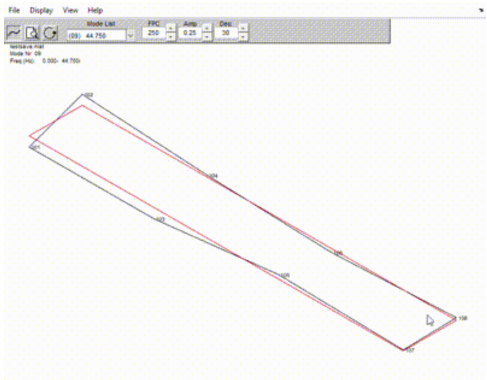

Figure 182 - ODS at Blade Passing Frequencies for Resistance tests at advanced speed of 1.159 m/s with frequency of 45 Hz

Appendix B.2. Hull Pressure Sensors' Measurements

Appendix B.2.1. Resistance Tests FFT Results

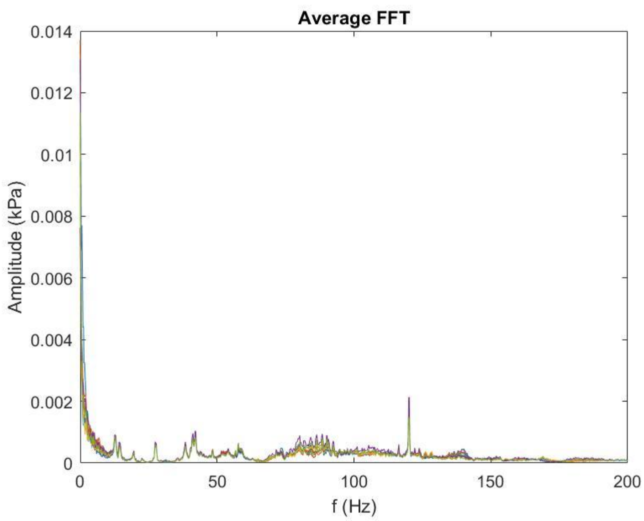

Figure 183 - Average FFT for Pressure Sensors for Resistance Test at 0.734 m/s

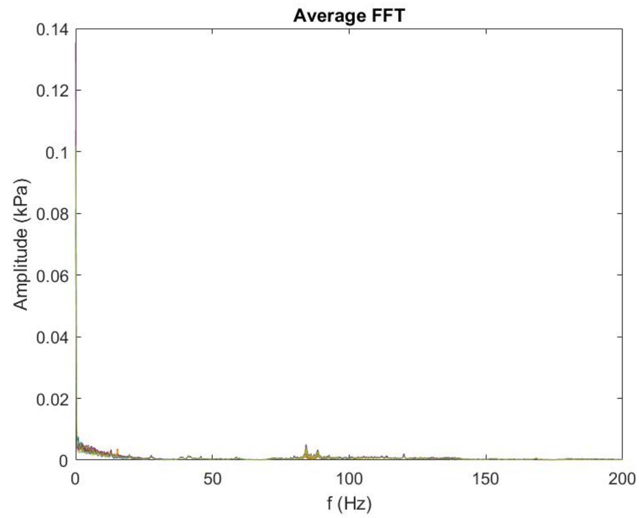

Figure 184 - Average FFT for Pressure Sensors for Resistance Test at 1.468 m/s

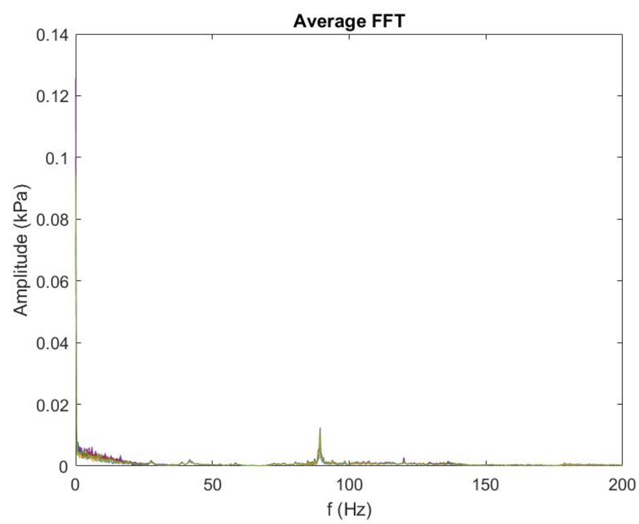

Figure 185 – Average FFT for Pressure Sensors for Resistance Test at 1.559 m/s

Appendix B.2.2 Bollard FFT Tests Results

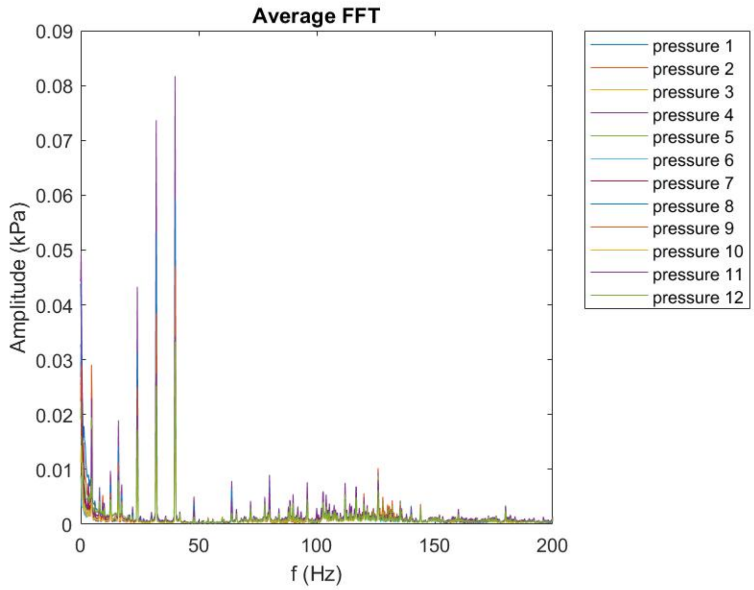

Figure 186 - Average FFT for Pressure Sensors for Bollard Test at propeller speed of 2-15 RPS

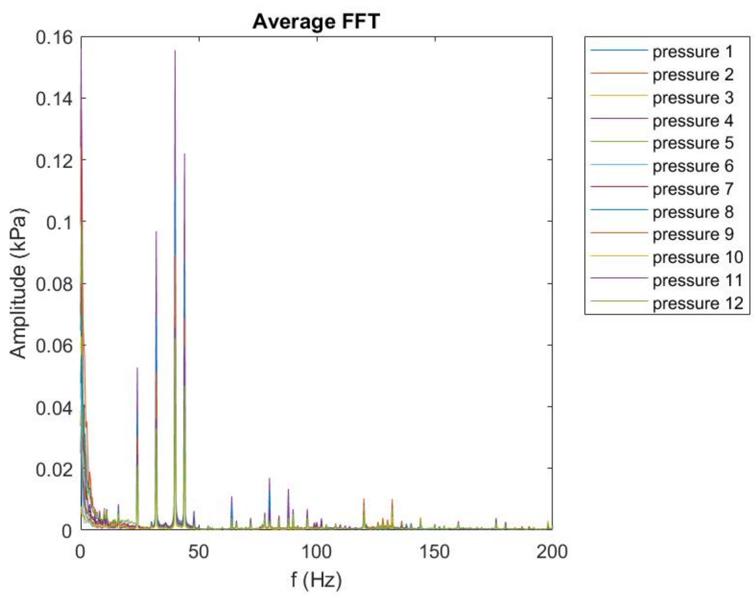

Figure 187 - Average FFT for Pressure Sensors for Bollard Test at propeller speed of 2-11 RPS

Appendix B.2.3 Self-Propulsion FFT Tests Results

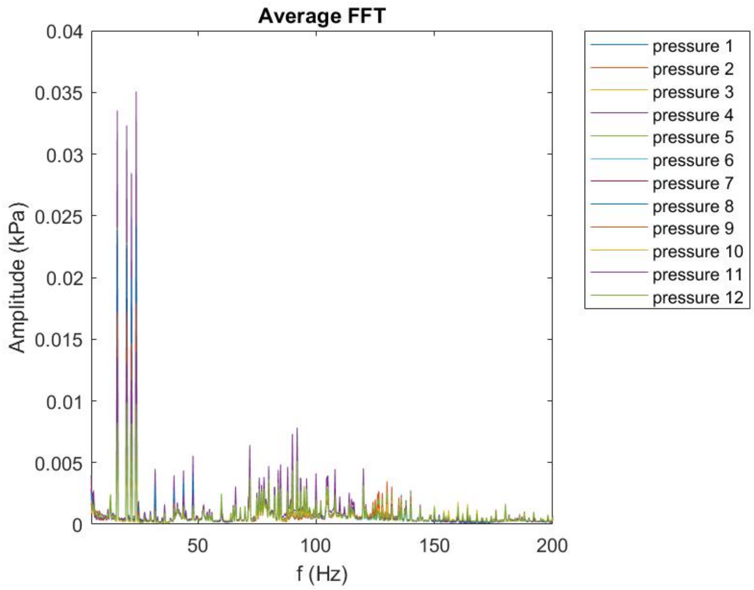

Figure 188 - Average FFT for Pressure Sensors for Self-Propulsion Test at advanced speed of 0.917 m/s and multiple RPS

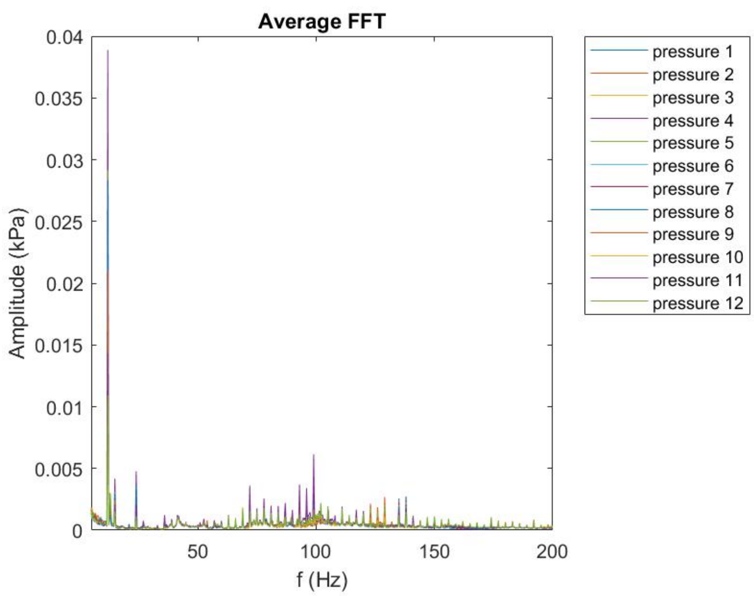

Figure 189 - Average FFT for Pressure Sensors for Self-Propulsion Test at advanced speed of 0.917 m/s and 3 RPS

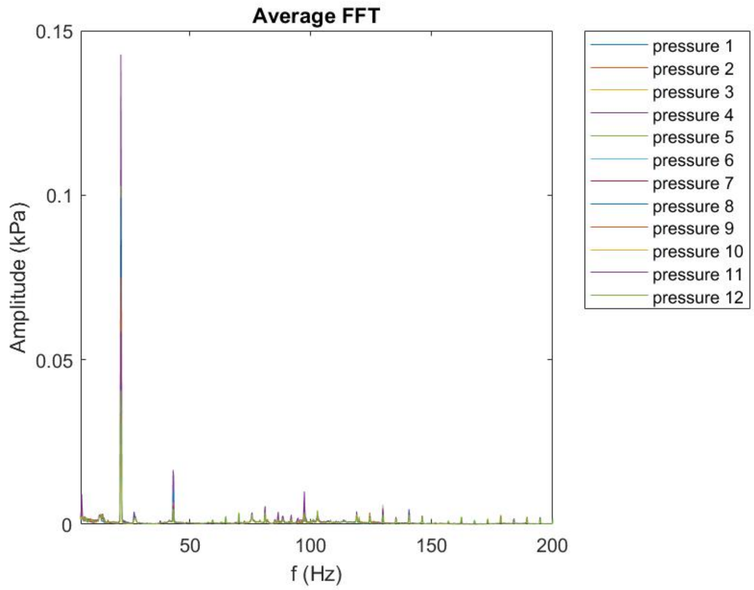

Figure 190 - Average FFT for Pressure Sensors for Self-Propulsion Test at advanced speed of 1.101 m/s and 5.41 RPS

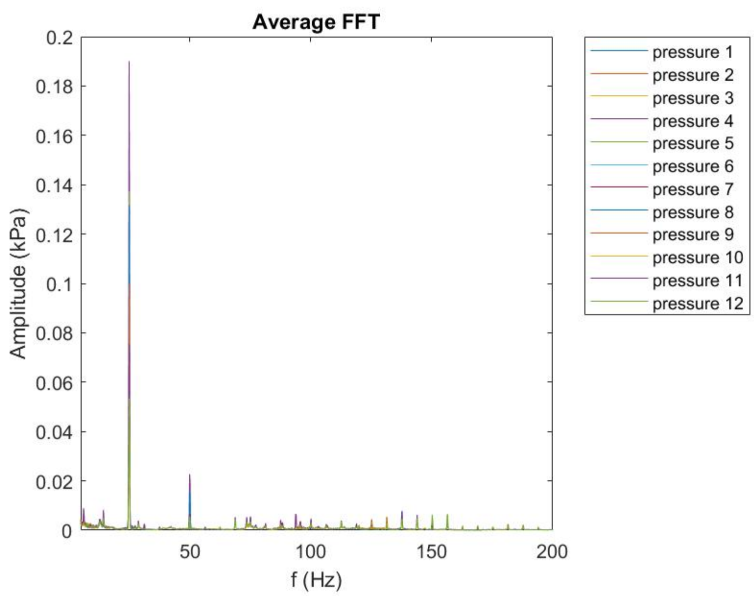

Figure 191 - Average FFT for Pressure Sensors for Self-Propulsion Test at advanced speed of 1.284 m/s and 6.26 RPS